Department of Physics and Astronomy

University of Heidelberg

Diploma thesis

in Physics

submitted by

Darvasi, Gábor

born in Budapest

2011

Optical Control of X-Ray Lasing

This diploma thesis has been carried out by Darvasi, Gábor at the
Max-Planck-Institut für Kernphysik
under the supervision of
Prof. Dr. Keitel, Christoph H.
and
Prof. Dr. Dubbers, Dirk
Physikalisches Institut Heidelberg

Optische Kontrolle der Lasertätigkeit im Röntgenbereich:
Freie-Elektronen-Laser haben das Gebiet der Röntgenphysik durch die Erzeugung von Röntgenstrahlung mit Intensitäten über 10^{18} W/cm^2 revolutioniert. Ihre Strahlung hat jedoch nur geringe Kohärenz und die zeitliche und räumliche Struktur ihrer Pulse kann nicht kontrolliert werden. Wir untersuchen die Möglichkeit Röntgen-Laserpulse mit optischem Licht zu kontrollieren und zu formen. Ein optischer Laser kontrolliert die Besetzungsinversion für den $2p \rightarrow 1s$ Übergang eines Neon-Röntgenlasers, der mit einem Freie-Elektronen-Laser gepumpt wird. Ausgehend von Bilanzgleichungen für die Photonzahl und die Besetzung der Laserniveaus untersuchen wir die Abhängigkeit der Pulse des Röntgenlasers von den Pulseigenschaften des optischen Lasers und des Freie-Elektronen-Lasers. Die Analyse der Kleinsignalverstärkung zeigt, dass eine geringe Bandbreite des Pump-Pulses und die genaue zeitliche Abstimmung des optischen Pulses und des Pumppulses miteinander Voraussetzung für wirksame optische Kontrolle sind. Unsere Rechnungen zeigen, dass die Herstellung hochintensiver sub-Femtosekunden-Laserpulse, die durch einen optischen Laser kontrolliert werden, möglich ist. Zusätzlich sind diese mit Femtosekunden-Genauigkeit an den optische Laserpuls synchronisiert. Die Ergebnisse zeigen, dass dieses Laserschema für Anrege-Abfrage-Techniken mit einem Femtosekunden-Röntgenlaserpuls und einem optischen Laserpuls verwendet werden kann.

Optical Control of X-Ray Lasing:
X-ray free-electron lasers have revolutionized x-ray science by achieving unprecedented intensities exceeding 10^{18} W/cm^2. However, they lack temporal coherence and controllability of their pulses' temporal and spatial properties, which is essential for many applications. We investigate the possibility to control and shape x-ray laser pulses with optical light. An optical laser pulse is used to control the population inversion on the $2p \rightarrow 1s$ transition in a neon x-ray laser pumped by an x-ray free-electron laser. Theoretical results are presented based on population and photon rate equations. We study the dependance of the x-ray laser's output on the pump pulse's and the optical laser pulse's properties. Small-signal gain calculations reveal that for a high degree of control narrowband pumping radiation is required and the optical laser pulse must have precise timing with respect to the pump pulse. Self-consistent gain calculations show that it will be possible to do spatial pulse shaping and to produce high-intensity, sub-femtosecond pulses that are controlled by and synchronized to the optical laser pulse with femtosecond precision. Our results indicate that the presented scheme would make it possible to establish pump-probe techniques with femtosecond x-ray and optical pulses.

Contents

List of Figures

List of Tables

1. Introduction

Laser light's coherence, extremely narrow line width, high intensity and rapid controllability [1] has had profound effects on the way research is done in the natural sciences. Some of the most notable applications exploiting these unparalleled properties include: laser spectroscopy [2], which has enabled scientists to gather structural information on atomic and molecular states with unprecedented spectral and time resolution; the cesium atomic clock [3] which serves as the basis of our time standard; and the trapping and cooling of atoms by laser light [4] in order to study fundamental questions in quantum mechanics. Motivated by the impact lasers in the microwave, infrared and optical regions have had, researchers have long endeavored to extend lasing into the x-ray region. Ultrashort, controllable x-ray laser pulses would make it possible to achieve control of atomic and molecular dynamics and to transfer laser-spectroscopy techniques [2] to the x-ray regime. In this thesis, we examine an optically controlled x-ray laser (XRL) and present results in support of the possibility to generate sub-femtosecond, intense x-ray pulses synchronized to an optical laser.

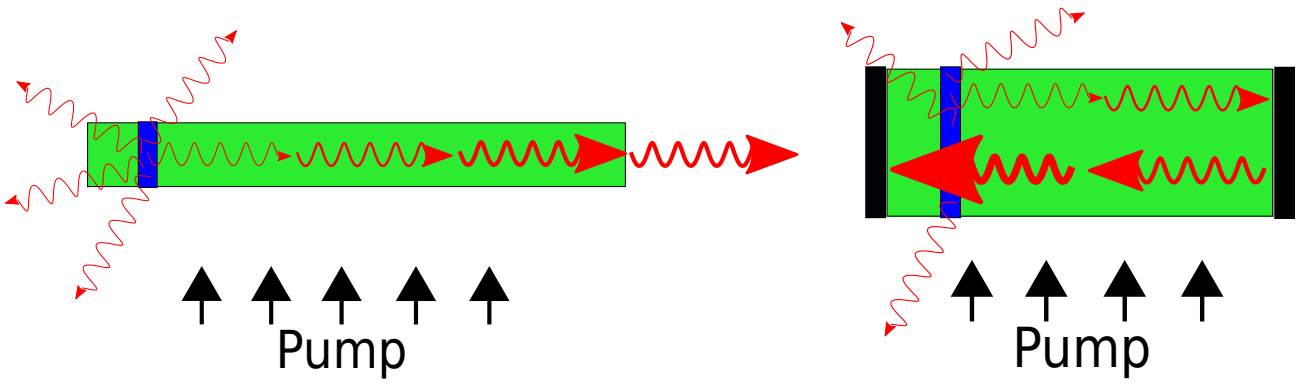

Figure 1.1.: (a) Amplified spontaneous emission. A pump excites the atoms of an active medium. The spontaneously emitted radiation from the blue area is subsequently amplified through stimulated emission. The output is highly directional as only photons propagating along the medium's longer axis are properly amplified. (b) By using a cavity the radiation can be directed back into the active medium resulting in further amplification through stimulated emission.

Lasers are based on the concept of stimulated emission introduced by Einstein in 1917 [5] to describe the emission of radiation by an excited atom (molecule) interacting with an external electromagnetic wave of the same frequency. The most basic setup for a laser consists of a active medium and an energy source [1, 6, 7], as shown in Fig. (1.1a). The energy source, also called the pump, excites the atoms in the medium, establishing a population inversion; this means that more atoms populate the upper level of a radiative transition than the the lower level. Then, spontaneously emitted photons in the decay of the excited states cause stimulated emission of identical photons from other excited atoms.

In the optical region, commonly, the active medium is placed in a cavity [1], as shown in Fig (1.1b). The photons are bounced back and forth, and the radiation is amplified every time it traverses the active medium resulting in higher intensities. Both setups produce coherent, narrowband and highly directional radiation [1]. Using optical cavities has the added benefit of restricting lasing to very few modes and that a smaller population inversion suffices to generate an output as the effective length of the amplifying medium is increased [1]. The first working laser was constructed by Maiman in 1960 from of a silver-coated ruby crystal pumped by a high-power flash lamp [6, 7]. Preceding this, several people did key theoretical work contributing to the conception of the laser. Townes was first to suggest the use of excited molecules to create a source of electromagnetic waves in the microwave region based on stimulated emission. Gordon, Zeigler and Townes went on to construct the first maser, which stands for "microwave amplification by stimulated emission of radiation", in 1954 [8, 9]. Publications on the theory of extending maser techniques to the infrared and optical region, were independently published by Schawlow and Townes [10], and Prokhorov [11] in 1958, who later each received the Nobel Prize in Physics [12–14] for their work on lasers.

Significant effort has been put into the development of short wavelength lasers in order to transfer and improve upon applications based on highly intense and coherent radiation in the optical region. Extending lasing into the x-ray region has faced great difficulties [15–18]. The lack of high reflectivity mirrors that can sustain intense x-ray radiation [16] and the short duration of population inversion caused by K-shell decay rates [19] which would necessitate the use of extremely short cavities [18], directed the development of x-ray lasers to schemes based on single pass amplification of spontaneous emission [1, 20]. Such schemes require a very large gain-length product [1, 18]. The gain [1] of an active medium is a measure for the amplification of pulse per unit length. Thus, the gain-length product is a measure for the pulse's total amplification over the entire propagation distance in the active medium. In contrast to XRLs, a laser pulse in the optical region can be bounced off the mirrors of a cavity and guided through the active medium several times increasing the total propagation distance. A gain approximately 100 times larger is required for XRL operation than for optical laser operation [15]. Due to the unfavorable scaling of the stimulated emission cross section towards smaller wavelengths [1] a very large population inversion is required in order to achieve gain that is large enough for lasing to take place within limited time and distance [15, 16, 18]. Furthermore, the power per unit volume required to sustain a population inversion is related to the spontaneous decay rate and the transition wavelength. It scales inversely with the transition wavelength to the power of five [18] meaning that a very high pumping power is necessary to obtain a given gain-length product. Laser schemes that proved successful in the optical region could not be simply transferred to XRLs [15]. It was realized that outer-shell, "optical" transition in highly charged ions could be used for lasing in the x-ray region [15, 16]. Electron-collisional excitation and electron-collisional recombination [15] have proven to be the best pump mechanisms for delivering the required, high pump power [15, 16]. Unfortunately, plasma-based collisional and recombinational schemes have a number of shortcomings: namely, wavelengths down to only approximately 10 nm in the soft x-ray region have been achieved [16], and doppler broadening due to the high temperatures as well as stark broadening due to strong electric fields in the plasma result in a large line

width [15]. Several alternative approaches to achieving lasing in the x-ray region exist. To date, x-ray free electron lasers (FEL) [21–23] offer the best approach to the generation of tunable and coherent radiation extending into the hard x-ray region with unparalleled peak intensities [16]. Presently, three x-ray FEL facilities are running, namely the Free-electron LASer at Hamburg (FLASH) [24], the Linac Coherent Light Source (LCLS) at SLAC [25, 26] in Stanford and the Spring-8 Angstrom Compact Free Electron Laser (SACLA) in Harima, Japan [27, 28]. All of these facilities are based on the principle of self-amplified spontaneous emission (SASE) [29–31] and produce x-ray FELs pulses with a chaotic temporal and spectral intensity profile; they are composed of several coherent intensity spikes of femtosecond duration that are incoherent with each other. X-ray FEL pulses lack a number of properties available to optical laser: namely, controllability of the beam properties, synchronization with respect to another laser pulse, spectral narrowness, and the ability to temporally and spatially shape the pulses.

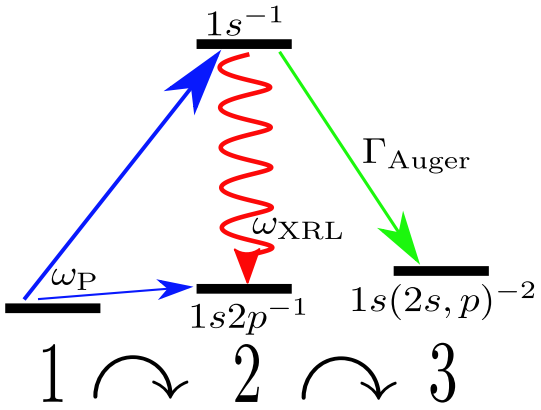

Figure 1.2.: Energy level diagram of neon laser on $K-\alpha$ transition. An x-ray pump with energy ω_{P} ionizes the $1s$ electron from a neutral atom. Lasing proceeds on the $1s^{-1} \rightarrow 1s2p^{-1}$ transition at the photon energy ω_{XRL}. The upper level is rapidly depleted through Auger decay. The figure is taken from [33].

Another alternative approach is to use inner-shell atomic transitions for x-ray lasing [15]. A photoionization-pumped inner-shell atomic XRL was first proposed by Duguay and Rentzepis in 1967 [32]. Several more theoretical studies have since been done [18, 33–40]. The scheme is based on the fact that radiation with a certain wavelength is severalfold more likely to remove tightly bound electrons than loosely bound electrons, as above threshold the photoionization cross section strongly decreases towards larger photon energies [19]. Since inner-shell electrons are preferentially ionized a population inversion is created [32]. In a subsequent spontaneous radiative decay of the core-ionized state, an outer shell electron fills the vacancy, as displayed in Fig. (1.2). The spontaneously emitted photons then induce stimulated x-ray emission from other core-ionized atoms [32]. The population inversion is self-terminating because its lifetime is limited by the decay of the upper level. The lifetime of a K-shell hole is dominated by Auger decay and is on the order of a few femtoseconds [19]. Due to the temporally short population inversion, longitudinal pumping of the XRL is necessary [32]. The pump pulse travels down the entire length of the active medium parallel to the axis of amplification, leaving a transient

population inversion in its wake. Ultra-intense pump pulses with short rise times that ionize the atoms more quickly than the inner-shell holes decay are needed to build-up a population inversion [18, 33]. Due to the lack of appropriate pumping radiation XRLs based on this scheme could not be realized for a long time [15, 16]. The idea to pump Duguay and Renzepis' atomic inner-shell XRL [32] with a x-ray FEL was first proposed by Lan *et al.* in 2004 [35]. Feasibility of the scheme was recently demonstrated for the first time [41] in a gaseous neon medium pumped by LCLS pulses [37–39].

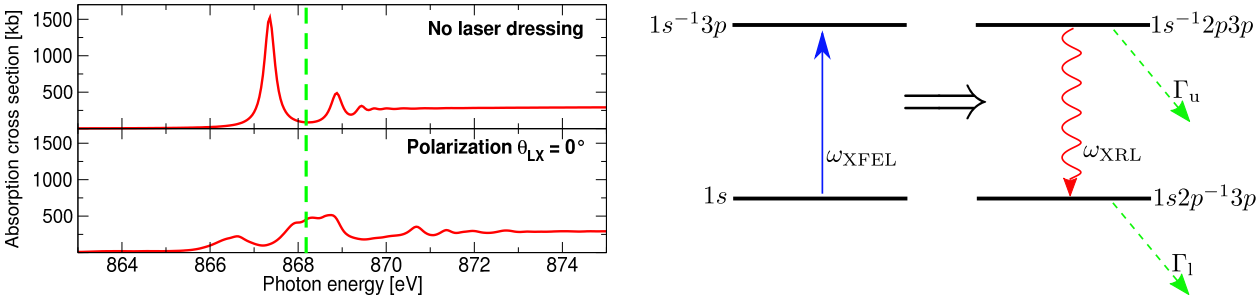

Figure 1.3.: (a) The absorption cross section is displayed in the vicinity of the K edge for the field-free case in the top panel and for laser-dressed case in the bottom panel. The dashed, green line indicates the x-ray FEL photon energy ω_{XFEL}. (b) Radiation from the x-ray FEL excites the neon atom to the $1s^{-1}3p$ Rydberg state. Subsequently an electron from the $2p$ orbital fills the $1s$ vacancy and the atom emits an x-ray photon ω_{XRL}. The decay rates of the upper and lower levels of the lasing transition are denoted by Γ_{u} and Γ_{l}, respectively.

We propose an inner-shell neon XRL pumped by an x-ray FEL. Our scheme is the same as the one described in the previous paragraph with two variations. First, we choose a x-ray FEL pump frequency ω_{XFEL} below the K edge, as indicated by the dashed, green in Fig. (1.3a). The $1s$ electron is not ionized anymore, instead it is excited to the $3p$ Rydberg orbital. Lasing proceeds on the $1s^{-1}2p3p \rightarrow 1s2p^{-1}3p$ transition. The lifetime of the upper level and the population inversion is still dominated by the Auger lifetime of the K-shell hole. A schematic of the lasing process is shown in Fig. (1.3b). The second deviation from Duguay's and Renzepis's XRL is that we add an optical laser pulse to the setup that propagates through the medium collinearly with the x-ray FEL pump pulse. The optical laser pulse dresses [42] the neon atoms and causes a modulation of the absorption cross section [43, 44], as shown in Fig. (1.3a). By tuning ω_{XFEL} to a minimum in the field-free absorption cross section, the neon atoms are efficiently excited only in the presence of the optical laser pulse. This mechanism allows us to control the build-up of population inversion, the active medium's gain and the lasing process generally. Our scheme offers rapid controllability, and the ability to temporally and spatially shape XRL pulses.

The sub-femtosecond length of the XRL pulses and their synchronization with the optical laser pulse can be exploited in time-resolved spectroscopy methods [2] in the x-ray region. For instance, using the XRL pulse as the pump in a two-color pump-probe setup, the time-dependent study of resonances in the x-ray region is possible [2, 45, 46]. Furthermore, the shortness of the XRL pulses is beneficial for coherent x-ray scattering experiments [47–50]. Radiation damage, which determines the resolution limit in the

imaging of biological samples, is reduced by using shorter x-ray pulses [50] resulting in higher quality scattering patterns.

2. X-ray physics

X-rays were discovered by Röntgen in 1895 [51] and immediately became an indispensable tool for probing the structure of matter due to their high penetration depth. The discovery of x-ray diffraction by von Laue initiated the development of scattering-based techniques for the structural analysis of atoms, molecules and solids [19]. More than a century later, x-ray diffraction is still the most commonly used technique for the structural analysis in chemistry, biology and material sciences. X-ray tubes remained the only sources of x-rays until the 1970's when it was discovered that synchrotron radiation emitted from storage rings could be exploited as a much more intense x-ray source. The construction of synchrotron facilities dedicated to the production of x-rays started a new era in x-ray science. Modern day, third generation synchrotron facilities can reach peak brilliances higher by a factor of 10^{12} than x-ray tubes and allow the experimentalist to adjust the energy, polarization and bandwidth of the radiation to his specific needs [19]. X-ray FELs [22, 23] are fourth generation synchrotrons that can reach peak brilliances still higher by about three orders of magnitude.

X-rays are electromagnetic waves with wavelengths in the range of 0.1 Å – 300 Å. Their interaction with matter can be categorized into two processes, namely scattering and absorption [19]. X-rays are scattered by electrons in the target. Mainly elastic scattering is exploited in structural analysis techniques, and a classical description of the process suffices [19]. Single-crystal x-ray diffraction is the most basic scattering method [19]; an x-ray beam is directed onto a crystal, it is scattered and then produces a diffraction pattern consisting of bright peaks coming from those scattered beams that fulfill the condition for constructive interference. The position and intensity of the spots is then measured with a detector for every orientation of the crystal. From these results the size and symmetry of the crystal's unit cell, and the atoms or molecules within it can be determined. Obtaining single crystals is often not possible and instead crystalline powders need to be used which consist of many tiny crystallites that are randomly oriented. Several powder diffraction techniques have been developed and it is possible to gain the same structural information as from single-crystal x-ray diffraction [19].

In the absorption of x-rays by matter, an x-ray photon is absorbed by a bound electron which is either excited into a higher electronic state or, if the photon energy exceeds the electron's binding energy, it is ejected from the atom [19]. The free electron's kinetic energy [52] is then given by

$$E_{\mathrm{kin}} \quad = \quad \omega_{\mathrm{X}} - E_{\mathrm{b}} \ , \tag{2.1}$$

where the ω_{X} is the energy of the x-ray photon and E_{b} is the electron's binding energy. The excitation or ionization of electrons can also happen due to the absorption of multiple photons [53]. The total energy transfer is then equal to the sum of the photons' energy. Multiphoton absorption is a higher-order, nonlinear optical process much more unlikely than single-photon absorption. Very high intensities are required for it to be observed.

When an inner-shell electron is ionized, the core vacancy is filled by an electron from an outer shell [19]. The atom, thereby emits an x-ray photon with energy corresponding to the difference in the electron's binding energy. X-ray fluorescence spectroscopy [19] is an analytical technique that measures the aforementioned x-ray photon's spectrum. Since the energy level structure of atoms is element specific, the fluorescence spectrum makes it possible to identify the components of a sample [19]. Alternatively, when an outer electron fills a core hole, a second electron can be emitted from an outer shell. This process is called Auger decay [19]. An analytical technique utilizing the Auger effect is Auger electron spectroscopy which measures the emitted electrons' energy spectrum to identify the chemical composition of a sample.

The magnitude of absorption is characterized by the x-ray absorption cross section $\sigma(\omega_{\mathrm{X}})$ [19] as a function of the x-ray photon energy ω_{X}. The absorption cross section is defined in a way that the absorption rate, describing the number of absorption events per second, is given by

$$r_{\mathrm{abs}} \;=\; \sigma(\omega_{\mathrm{X}})\frac{I_{\mathrm{X}}}{\omega_{\mathrm{X}}}\ . \tag{2.2}$$

$\sigma(\omega_{\mathrm{X}})$ is approximately proportional to $1/\omega_{\mathrm{X}}^3$ and exhibits sudden jumps typically spanning about one decade at some element specific photon energies [19]. These jumps are called absorption edges and the physical reason for their appearance is that electrons are bound to the nucleus by discrete energies. The x-ray photons can only interact act with electrons if their energy exceeds the electron's binding energy. At an absorption edge the photon energy is increased just enough for electrons from a inner shell to be energetically able to participate in the absorption of the x-rays, thereby, opening additional absorption channels. Such an absorption edge can be seen in Fig. (1.3a), where the absortption cross section increases from approximately zero to over 300 kBarn at energies above 870 eV. This is because the binding energy of a K shell electron in neon is 870.2 eV [43] and the single-photon ionization of this shell becomes possible. The resonances below the ionization threshold in Fig. (1.3a) are due to the resonant excitation of the K shell electrons to the np Rydberg states, where $n \geq 3$. The position of the absorption edges and the near-edge structure of the cross section are also element specific making it possible to identify materials based the their absorption spectrum [19]. Additionally to its strong dependance on the x-ray photon energy, $\sigma(\omega_{\mathrm{X}})$ varies with the atomic number Z of the absorber approximately as Z^4. It is this strong variation, leading to clear contrasts between materials, that makes x-rays an invaluable tool for imaging [19].

3. X-ray sources

X-ray tubes were the only method for producing radiation in the x-ray region from the time of their discovery until the 1970's when the first synchrotron facilities dedicated to x-ray science were built [19]. All x-ray tubes have the same basic setup [19] and only few technical improvements were made during this time. Free electrons are accelerated by an electric field towards a metal anode in a vacuum. The electrons' kinetic energy is subsequently transformed into x-ray radiation by one of two processes. The electrons are suddenly decelerated in collisions with the atoms and emit bremsstrahlung [54]; a continuous spectrum is produced in this process as the radiation's frequency depends on the change of an electron's momentum in a collision. Bremsstrahlung has a maximum frequency corresponding to the total kinetic energy of the electrons. Second, in a collision between a free electron and an atom, an electron can be knocked out from an inner shell. This vacancy is then filled by an electron from an outer shell. The atom, thereby emits a photon with energy equal to the difference of the binding energies of the two shells. This process is called x-ray fluorescence [19] and produces radiation at discrete energies and intensities that are orders of magnitude higher than bremsstrahlung. The fluorescence spectrum is commonly used for experiments where a monochromatic beam is required. The x-ray tube has some severe limitations, namely the frequency of the narrowband high-intensity peaks is not tunable and only a small fraction of the photons can be utilized in a spatially narrow beam [19].

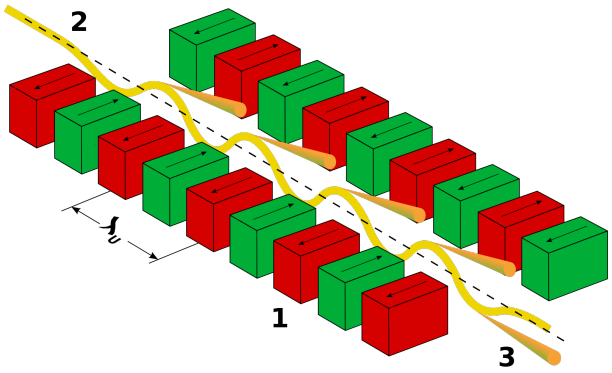

Figure 3.1.: The electrons in the beam (2) are forced to oscillate by a static magnetic field (1) of period λ_U and emit radiation (3) whilst propagation. (Figure is from http://en.wikipedia.org/wiki/undulator.)

Many new x-ray experiments were made possible by the construction of synchrotrons [19]. Modern-day, third generation synchrotrons produce tunable x-rays with intensities up to ten orders of magnitude higher than x-ray tubes [19]. A synchrotron is a circular device in which electrons are accelerated to relativistic speeds. A constant centripetal

force is applied to the electrons in order to keep them on their circular path. Accelerated charged particles emit radiation [54], such that radiation is emitted in a cone tangentially to the electrons' trajectory [19]. The emitted spectrum is very broad ranging from the infrared to the hard x-ray region. Synchrotrons can produce x-rays much more efficiently with the use of an undulator. An undulator [19] is a long periodic structure composed of an array of magnets with alternating poles. These devices are placed into a straight segment of the synchrotron. In these straight segments the magnetic field forces the electrons to carry out oscillations in a vertical plane, as shown in Fig. (3.1). The electrons emit radiation, predominantly in the forward direction due to their relativistic speeds [19, 54], during each oscillation. The radiation emitted by an electron in one oscillation is in phase with the radiation emitted by the same electron in other oscillations [19, 42], meaning that the intensities add up coherently; the amplitudes of the electric field are first added up and then the total is squared to obtain the intensity. The condition for this is that the electrons perform very small oscillations such that the radiation is strongly compressed to the forward direction [19, 54] and the radiation cones from one oscillation overlap with the radiation cones from the electrons' other oscillations [19]. The intensities add up coherently only for a certain wavelength, which implies that undulator radiation is monochromatic [19], if the less intense broad background is neglected. The wavelength for which this is the case depends on the undulator period, that is the distance between neighboring magnets and the electron's velocity. Undulator radiation has many properties that are desired in x-ray physics, namely a monochromatic, high intensity beam with small beam divergence is produced [19]. However, synchrotron radiation has limited coherence, does not reach high enough intensities to test nonlinear optical processes in the x-ray region [55] and lacks the temporal resolution for the study of atomic or molecular dynamics [23]. X-ray free electron lasers present a solution to these shortcomings.

3.1. X-ray free electron lasers

The theoretical framework for free electron lasers (FEL) was developed by Madey in 1971 [21] and the first successful demonstration of a FEL was done by Madey *et al.* in 1976 [56]. An x-ray FEL facility consists of a particle accelerator and an undulator. The electrons are accelerated to relativistic velocities and sent through the undulator where they are forced to oscillate in the same way as in synchrotrons [19]. As explained in the previous section the electromagnetic waves emitted by a single electron in an undulator are coherent with each other, but the radiation emitted by different electrons is incoherent. If the electrons in an undulator could be forced to oscillate in phase with each other much higher intensities would become accessible due to the constructive interference and the radiation generated this way would be fully coherent [19, 42]. In a x-ray FEL the parameters of a very long [57] undulator are optimized in a way that this is accomplished. Initially, when the electron bunch from the accelerator enters the undulator, the electrons have no specific spatial order and are distributed like in a gas [19]. At the beginning of the undulator the electrons start to incoherently radiate electromagnetic waves with which they in turn interact; the radiation forces the electrons into micro-bunches that are spatially confined to much less than the radiation's wavelength and separated from

each other by exactly one wavelength [19, 42]. The micro-bunches oscillate in phase with each other and emit electromagnetic waves coherently. This mechanism is called self amplification of stimulated emission (SASE). In practice, the micro-bunching process is quite messy and is strongly influenced by the accelerator's start-up noise; several sets of micro-bunches, which are not in phase with each other, are formed per shot [19]. This is the reason why x-ray FELs produce radiation with a chaotic intensity profile consisting of several temporally coherent, femtosecond intensity spikes that are incoherent with each other [29, 31]. Each intensity spike belongs to one train of micro-bunches. The wavelength of the emitted radiation is determined by the electrons' energy, making FELs widely tunable systems [42]. X-ray FELs are currently the only devices capable of producing coherent radiation in the hard x-ray region [16]. Although x-ray FELs have some very desirable properties, they also have a number of shortcomings: namely, they lack controllability of their output; their pulses vary on a shot-by-shot basis due to their chaotic nature; synchronization with respect to an optical laser pulse of femtosecond duration is difficult due to pulse jitter; and they lack spectral narrowness.

The first fully operational x-ray FEL facility was FLASH at DESY in Hamburg, Germany, which began operation in August 2005 [24, 57]. Flash operates in the soft x-ray region with wavelengths down to 4.12 nm [24]. The second running x-ray FEL facility was LCLS at SLAC [26, 57] in Stanford, which began operation in 2009. LCLS was the first facility to produce hard x-rays with wavelengths down to 0.12 nm [25]. The third running x-ray FEL facility is the Spring-8 Ångström Compact Free-Electron Laser(SACLA) [27,28] in Japan, which will be accessible to users as of March 2012. Lasing at a wavelength of 0.1 nm has already been demonstrated at SACLA with a laser power superior to LCLS [27]. Several hard x-ray FELs are currently under construction: the European XFEL [58] in Hamburg, which is expected to be running by 2015; the SwissFEL at the Paul Scherrer Institute in Switzerland [59]; and others. All these facilities are based on the SASE process. At LCLS a new beamline for a self-seeded x-ray FEL [23, 60, 61] is being built at the moment [26]. In a self-seeded FEL two consecutive undulators are used, where the output of the first undulator generated by the SASE process is subsequently sent through a monochromator and amplified through interaction with the electron beam in the second undulator [23]. A self-seeded x-ray FEL has significantly improved temporal coherence, a reduced bandwidth, a Gaussian temporal pulse shape, as well as a higher peak intensity [23]. A brief comparison of the beam properties from LCLS and FLASH is given in Tab. (3.1).

Table 3.1.: Beam characteristics at FLASH [24], the LCLS AMO and SXR beamlines [26], and the planned self-seeded LCLS-II beamline at SLAC [26].

Facility	energy range [eV]	energy resolution $\Delta E/E$	photons per shot	duration FWHM [fs]
FLASH	30-200	0.005-0.01	10^{12}	10-50
AMO	480-2000	0.005-0.01	up to 10^{13}	5-300
SXR	500-1500	0.0001-0.00025	up to 2×10^{11}	5-300
Seeded	8500-10000	0.0001-0.0004	up to 3×10^{11}	4-10

X-ray FELs are of great interest for experimentalists in several areas of research. In

atomic and molecular physics the main interest is the interaction of high intensity coherent x-ray radiation with atoms or molecules, such as nonlinear quantum optics [62–64], electronic response of matter to ultra-intense x-rays [65], double core ionization [66] and the study of hollow atoms [55]. Also, several applications have been found for x-ray FELs in structural biology, chemistry and material science because they provide both the required time and spatial resolution to image processes of the sub-nanometer world. Particular areas of current research are the imaging of macromolecules [48,67], viruses [68], cells [47] and nanostructures [69] with femtosecond coherent x-ray pulses.

3.2. Partial-coherence method

We use the partial-coherence method (PCM) [70] for generating model pulses produced by SASE FELs [29,31]. PCM is a numerical method for obtaining the temporal and spectral shape of single-shot FEL pulses. PCM is applicable to non-saturated SASE operation of FELs and reproduces the experimentally measured average spectrum $\langle S(\omega_{\mathrm{X}})\rangle$ [71] and creates single-shot pulses with statistical and coherence properties that are consistent with FEL theory [29, 31]. Also, the general structure of single-shot pulses and the results of nonlinear optics experiments using PCM pulses are in agreement with experimental measurements at x-ray FEL facilities [71], such as FLASH [24] in Hamburg. Experimentally accessible quantities, namely the average pulse spectrum $\langle S(\omega_{\mathrm{X}})\rangle$ and the average pulse duration are used as input for the calculations. The advantage of the PCM over other theoretical methods [22,30,72] for calculating the output of x-ray FELs is that the exact machine parameters of the x-ray FEL need not be known [70]. These parameters are not published along with scientific results, or lack precision due to measurement inaccuracy or technical issues such as thermal drifts [70].

At first, we introduce the formalism we use to describe PCM. Starting with the electric field $E(t)$ which needs to be real because it is a physical quantity, we define the electric field in the frequency domain [73] as

$$\widetilde{E}(\omega_{\mathrm{X}}) \;=\; \int_{-\infty}^{\infty} E(t)\mathrm{e}^{\mathrm{i}\omega_{\mathrm{X}}t}\mathrm{d}t \;. \tag{3.1}$$

Although $E(t)$ is a real function its Fourier transform $\widetilde{E}(\omega_{\mathrm{X}})$ is generally complex [73]. We denote all complex quantities with a tilde. The constraint that $E(t) = E^*(t)$ and that

$$E(t) = \frac{1}{2\pi}\int_{-\infty}^{\infty} \widetilde{E}(\omega_{\mathrm{X}})\mathrm{e}^{-\mathrm{i}\omega_{\mathrm{X}}t}\mathrm{d}\omega_{\mathrm{X}} \;, \tag{3.2}$$

is real, implies that

$$\begin{aligned} \int_{-\infty}^{\infty} \widetilde{E}(\omega_{\mathrm{X}})\mathrm{e}^{-\mathrm{i}\omega_{\mathrm{X}}t}\mathrm{d}\omega_{\mathrm{X}} \;&=\; \int_{-\infty}^{\infty} \widetilde{E}^*(\omega_{\mathrm{X}})\mathrm{e}^{\mathrm{i}\omega_{\mathrm{X}}t}\mathrm{d}\omega_{\mathrm{X}} \\ = -\int_{\infty}^{-\infty} \widetilde{E}(-\omega_{\mathrm{X}})\mathrm{e}^{-\mathrm{i}\omega_{\mathrm{X}}t}\mathrm{d}\omega_{\mathrm{X}} \;&=\; \int_{-\infty}^{\infty} \widetilde{E}^*(-\omega_{\mathrm{X}})\mathrm{e}^{-\mathrm{i}\omega_{\mathrm{X}}t}\mathrm{d}\omega_{\mathrm{X}} \;. \end{aligned} \tag{3.3}$$

The other way around, if $\widetilde{E}(\omega_{\mathrm{X}}) = \widetilde{E}^*(-\omega_{\mathrm{X}})$ holds, then $E(t)$ is real.

By specifying $\widetilde{E}(\omega_{\mathrm{X}})$ for $\omega_{\mathrm{X}} > 0$ we have complete information about $\widetilde{E}(\omega_{\mathrm{X}})$ and $E(t)$ because the negative frequency part can be obtained with $\widetilde{E}(-\omega_{\mathrm{X}}) = \widetilde{E}^{*}(\omega_{\mathrm{X}})$ for $\omega_{\mathrm{X}} > 0$. We write $\widetilde{E}(\omega_{\mathrm{X}}) = \widetilde{E}^{+}(\omega_{\mathrm{X}}) + \widetilde{E}^{-}(\omega_{\mathrm{X}})$ with $\widetilde{E}^{\pm}(\omega_{\mathrm{X}}) = \widetilde{E}(\omega_{\mathrm{X}})\Theta(\pm\omega_{\mathrm{X}})$, where $\Theta(\omega_{\mathrm{X}})$ is the Heaviside function and $\Theta(0) = 1$. For a real electric field $E(t)$ the relation $\widetilde{E}^{-}(-\omega_{\mathrm{X}}) = \widetilde{E}^{+^{*}}(\omega_{\mathrm{X}})$ holds by definition.

We define the complex electric fields $\widetilde{E}^{+}(t)$ and $\widetilde{E}^{-}(t)$ as the inverse Fourier transforms of $\widetilde{E}^{+}(\omega_{\mathrm{X}})$ and $\widetilde{E}^{-}(\omega_{\mathrm{X}})$, respectively. The physical electric field is $E(t) = \widetilde{E}^{+}(\omega_{\mathrm{X}}) + \widetilde{E}^{-}(\omega_{\mathrm{X}})$. With

$$\begin{aligned}
\widetilde{E}^{-}(t) &= \frac{1}{2\pi}\int_{-\infty}^{\infty}\widetilde{E}^{-}(\omega_{\mathrm{X}})\mathrm{e}^{-\mathrm{i}\omega_{\mathrm{X}}t}\mathrm{d}\omega_{\mathrm{X}} \\
&= -\frac{1}{2\pi}\int_{\infty}^{-\infty}\widetilde{E}^{+^{*}}(\omega_{\mathrm{X}})\mathrm{e}^{\mathrm{i}\omega_{\mathrm{X}}t}\mathrm{d}\omega_{\mathrm{X}} \\
&= \frac{1}{2\pi}\int_{-\infty}^{\infty}\widetilde{E}^{+^{*}}(\omega_{\mathrm{X}})\mathrm{e}^{\mathrm{i}\omega_{\mathrm{X}}t}\mathrm{d}\omega_{\mathrm{X}} \\
&= \frac{1}{2\pi}\Big[\int_{-\infty}^{\infty}\widetilde{E}^{+}(\omega_{\mathrm{X}})\mathrm{e}^{-\mathrm{i}\omega_{\mathrm{X}}t}\mathrm{d}\omega_{\mathrm{X}}\Big]^{*} \\
&= \widetilde{E}^{+^{*}}(t)\ ,
\end{aligned} \tag{3.4}$$

we can write $E(t) = 2 \times \Re[\widetilde{E}^{+}(t)]$.

Experimentally, it is only possible to measure the field intensities, not the electric field itself. For this reason we give expressions for the intensity and spectral intensity [73], respectively:

$$I(t) = \frac{1}{2\pi\alpha}|E(t)|^{2}\ , \tag{3.5}$$

$$S(\omega_{\mathrm{X}}) = \frac{1}{4\pi^{2}\alpha}|E(\omega_{\mathrm{X}})|^{2}\ . \tag{3.6}$$

The relationship between $I(t)$ and $S(\omega_{\mathrm{X}})$ is given by Parseval's theorem [73]:

$$\int_{-\infty}^{\infty} I(t)\mathrm{d}t = \int_{-\infty}^{\infty} S(\omega_{\mathrm{X}})\mathrm{d}\omega_{\mathrm{X}}\ .$$

Now, we proceed to describing PCM [70]. The average experimentally measured spectrum [71] is the starting point for producing pulses with PCM. We use a Gaussian function for the average spectrum

$$\langle S(\omega_{\mathrm{X}})\rangle = S_{0}\exp[-((\omega_{\mathrm{X}} - \omega_{\mathrm{S}})a)^{2}/2\Delta\omega_{\mathrm{S}}^{2}]\ , \tag{3.8}$$

where ω_{S} is the x-ray FEL central frequency, $\Delta\omega_{\mathrm{S}}$ is the FWHM of the average spectrum and $a = 2\sqrt{-2\ln(1/2)}$ is a constant.

We define the initial value for the modulus of the spectral electric field as

$$|\widetilde{E}_{\mathrm{i}}^{+}(\omega_{\mathrm{X}})| = 2\pi\sqrt{\alpha\langle S(\omega_{\mathrm{X}})\rangle}\ . \tag{3.9}$$

The phase ϕ_i of the initial electric field is undetermined and we assume it to be random, such that

$$\widetilde{E}_\mathrm{i}^{+}(\omega_\mathrm{X}) \;=\; 2\pi\sqrt{\alpha\langle S(\omega_\mathrm{X})\rangle}\mathrm{e}^{\mathrm{i}\phi_\mathrm{i}(\omega_\mathrm{X})}\;, \tag{3.10}$$

where $\phi_\mathrm{i}(\omega_\mathrm{X})$ is a random function in ω_X with values between $-\pi$ and π. The initial time-depedent electric field $\widetilde{E}_\mathrm{i}^{+}(t)$ follows from Eq. (3.2). The initial physical electric field is given by

$$E_i(t) = \widetilde{E}_\mathrm{i}^{+}(t) + \widetilde{E}_\mathrm{i}^{-}(t) = 2\Re[\widetilde{E}_\mathrm{i}^{+}(t)]\;.$$

Since the initial spectral phase is chosen to be random $\phi(\omega_\mathrm{X})$ the Fourier transform yields an infinitely long pulse for the electric field $E_i(t)$. To obtain pulses of finite duration, as is the case for SASE FEL pulses, we multiply $E_\mathrm{i}(t)$ with a temporal filtering function $F(t)$ giving us the electric field $E_\mathrm{SASE}(t) = F(t)E_\mathrm{i}(t)$ of the SASE pulse in the time domain. The temporal filtering function satisfies the condition that it only has non-zero values within an interval equal to the average pulse duration of the FEL. We choose

$$F(t) = \begin{cases} 0 & \text{if } t < 0, \\ \sin^2(\pi t/\tilde{t}_\mathrm{P}) & \text{if } 0 \le t \le \tilde{t}_\mathrm{P}, \\ 0 & \text{if } t > \tilde{t}_\mathrm{P}, \end{cases}$$

where $\tilde{t}_\mathrm{P}$ is the average duration of the pulses.

The temporal filtering has consequences on the electric field in the frequency domain, which is given by

$$\begin{aligned} \widetilde{E}_\mathrm{SASE}^{+}(\omega_\mathrm{X}) \;&=\; \int_{-\infty}^{\infty} F(t)\widetilde{E}_\mathrm{i}^{+}(t)\mathrm{e}^{\mathrm{i}\omega_\mathrm{X}t}\mathrm{d}t \\ &=\; \int_{-\infty}^{\infty}\frac{1}{2\pi}\int_{-\infty}^{\infty}\widetilde{F}(\omega_1)\mathrm{e}^{-\mathrm{i}\omega_1 t}\mathrm{d}\omega_1 \\ &\quad\times\frac{1}{2\pi}\int_{-\infty}^{\infty}\widetilde{E}_\mathrm{i}^{+}(\omega_2)\mathrm{e}^{-\mathrm{i}\omega_2 t}\mathrm{d}\omega_2\;\mathrm{e}^{\mathrm{i}\omega_\mathrm{X}t}\mathrm{d}t\;, \end{aligned} \tag{3.11}$$

where $\widetilde{F}(\omega_1)$ is the Fourier transform of $F(t)$. Integrating over t we find that

$$\int_{-\infty}^{\infty}\mathrm{e}^{-\mathrm{i}(\omega_1+\omega_2-\omega_\mathrm{X})}\mathrm{d}t = 2\pi\delta(\omega_1+\omega_2-\omega_\mathrm{X})\;,$$

hence, $\omega_2 = \omega_\mathrm{X} - \omega_1$ and

$$\widetilde{E}_\mathrm{SASE}^{+}(\omega_\mathrm{X}) \;=\; \frac{1}{2\pi}\int_{-\infty}^{\infty}F(\omega_1)E_\mathrm{i}^{+}(\omega_\mathrm{X}-\omega_1)\mathrm{d}\omega_1\;. \tag{3.12}$$

As a result of this, $\widetilde{E}_\mathrm{SASE}^{+}(\omega_\mathrm{X})$ is not equal to $\widetilde{E}_\mathrm{i}^{+}(\omega_\mathrm{X})$ and the SASE pulse's spectral phase $\phi_\mathrm{SASE}(\omega_\mathrm{X})$ is no longer completely random, leading to partial coherence of the SASE pulse [70].

The temporal profile of the intensity and the spectral intensity are shown in Fig. (3.2) for an example SASE pulse with central frequency $\omega_\mathrm{S} = 868.2$ eV, spectral FWHM $\Delta\omega_\mathrm{S} = 2.0$ eV and average pulse duration $\tilde{t}_\mathrm{P} = 100$ fs. The intensity and spectral intensity averaged over 800 shots is shown in Fig. (3.3) for the same parameters. The average intensity and average spectral intensity in Fig. (3.3) are not completely smooth due to the small sample size.

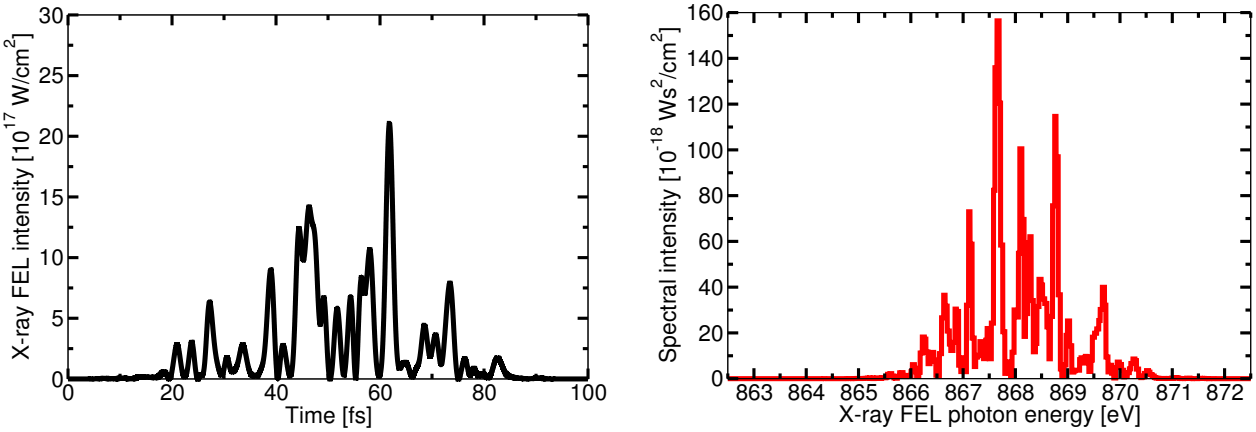

Figure 3.2.: Intensity (left) and spectral intensity (right) for a single SASE pulse with central frequency $\omega_{\mathrm{S}} = 868.2$ eV, spectral FWHM $\Delta\omega_{\mathrm{S}} = 2.0$ eV and average pulse duration $\tilde{t}_{\mathrm{P}} = 100$ fs.

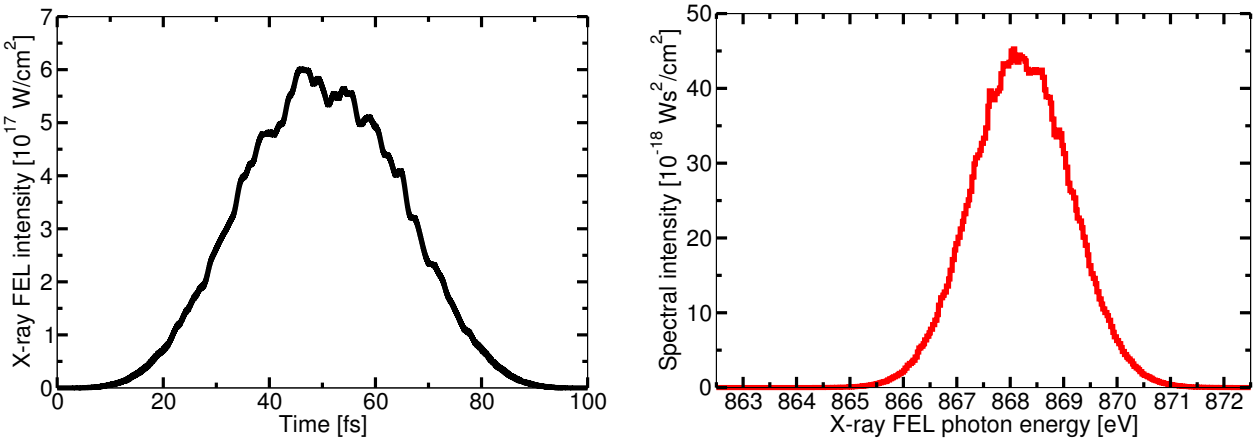

Figure 3.3.: Average intensity (left) and average spectral intensity (right) over 800 shots for SASE pulses with central frequency $\omega_{\mathrm{S}} = 868.2$ eV, spectral FWHM $\Delta\omega_{\mathrm{S}} = 2.0$ eV and average pulse duration $\tilde{t}_{\mathrm{P}} = 100$ fs.

4. Semiclassical laser theory

In this chapter we develop a semiclassical theory for treating the interaction of the radiation field with matter. Specifically, we investigate the interaction of a monochromatic, near-resonant wave traveling through an elongated medium consisting of homogeneously broadened two-level atoms, see Fig. (4.1). For our intents and purposes when we talk about a laser we refer to such a system where the two levels correspond to the upper and lower lasing states. We treat the radiation field classically with Maxwell's equations [54] and the atomic medium quantum mechanically with the von Neumann equation [74]. We wish to derive a set of equations that enables us to calculate the populations of the two levels. The radiation field interacts with the atoms inducing a polarization that in turn acts as source term for the field in the Maxwell's equations. We approximate the Maxwell-Schrödinger equations, which are a self-consistent set of equations describing the field and the matter [75], to acquire a set of coupled rate equations describing the time evolution of the populations and of the field intensity.

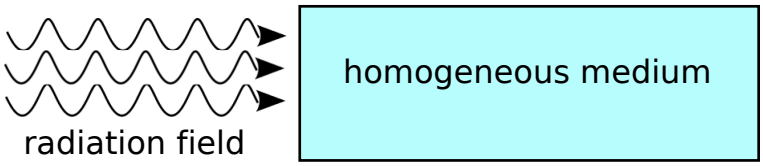

Figure 4.1.: We investigate a system composed of narrowband electromagnetic radiation resonantly propagating through a gas of homogeneously broadened atoms.

4.1. Atom-field interactions

In this section we investigate the interaction of an atom with the electromagnetic field. The atom is treated as a fully quantum mechanical two-level system and the radiation field is treated classically as a single mode field.

4.1.1. Atom-field interaction Hamiltonian

The time evolution of a quantum mechanical system is governed by the Schrödinger equation [74]

$$\mathrm{i}\frac{\partial\psi(\boldsymbol{r},t)}{\partial t} = \widehat{\mathscr{H}}\psi(\boldsymbol{r},t)\ , \tag{4.1}$$

where $\psi(\boldsymbol{r},t)$ is the wavefunction describing the quantum mechanical state of the system and $\widehat{\mathscr{H}}$ is the Hamiltonian.

An electron bound by the atomic binding potential $V(\boldsymbol{r})$ interacting with an external electric field $\boldsymbol{E}(\boldsymbol{r},t)$ can be described by the minimal-coupling Hamiltonian [75]

$$\widehat{\mathscr{H}} = \frac{1}{2}[\boldsymbol{p} + \boldsymbol{A}(\boldsymbol{r},t)]^2 - U(\boldsymbol{r},t) + V(\boldsymbol{r}) \ , \tag{4.2}$$

where $\boldsymbol{p} = -\mathrm{i}\boldsymbol{\nabla}$ is the canonical momentum operator and $\boldsymbol{A}(\boldsymbol{r},t)$ and $U(\boldsymbol{r},t)$ are the vector and scalar potential [54] of the electric field $\boldsymbol{E}(\boldsymbol{r},t)$, respectively. The electric field can be expressed through these potentials as

$$\boldsymbol{E}(\boldsymbol{r},\mathrm{t}) \ = \ -\boldsymbol{\nabla}U(\boldsymbol{r},t) - \frac{\partial \boldsymbol{A}}{\partial t} \ . \tag{4.3}$$

We choose the radiation gauge [54] for the external field, in which $U(\boldsymbol{r},t) = 0$, and $\boldsymbol{\nabla}\cdot\boldsymbol{A}(\boldsymbol{r},t) = 0$, such that we have $\boldsymbol{E}(\boldsymbol{r},t) = -\dot{\boldsymbol{A}}(\boldsymbol{r},\boldsymbol{t})$. Eq. (4.2) represents a very general Hamiltonian, which we would like to simplify to facilitate an easier mathematical treatment. We look for a physically motivated approximation. Atomic radii are typically on the order of a few Angstrom [52]. Assuming that the incident radiation is in the soft x-ray region, its wavelength is on the order of nanometers [52] and $\boldsymbol{k}\cdot\boldsymbol{r} \ll 1$, where $\boldsymbol{k}$ is the wave vector. This means that the electric field strength is approximately the same at all points of the atoms and the spacial variation of the electric field over the atom can be neglected in the first order. The Hamiltonian Eq. (4.2) can be reduced to a form suited for a simpler treatment of a two-level atom interacting with a radiation field by using the *dipole approximation* [75]. We assume the electron is bound by a potential $V(\boldsymbol{r})$ with a force center at $\boldsymbol{r}_0$, the position of the nucleus. If the condition $\boldsymbol{k}\cdot\boldsymbol{r} \ll 1$ is satisfied, the expression for the vector potential of the electromagnetic field can be simplified [54] by writing it as a Taylor series of the complex argument $\mathrm{i}\boldsymbol{k}\cdot\boldsymbol{r}$,

$$\begin{aligned} \boldsymbol{A}(\boldsymbol{r}_0+\boldsymbol{r},t) &= \boldsymbol{A}(t)\cdot \mathrm{e}^{\mathrm{i}\boldsymbol{k}\cdot(\boldsymbol{r}_0+\boldsymbol{r})} \\ &= \boldsymbol{A}(t)\cdot \mathrm{e}^{\mathrm{i}\boldsymbol{k}\cdot\boldsymbol{r}_0}\cdot(1+\mathrm{i}\boldsymbol{k}\cdot\boldsymbol{r}+\ldots) \\ &\approx \boldsymbol{A}(t)\cdot \mathrm{e}^{\mathrm{i}\boldsymbol{k}\cdot\boldsymbol{r}_0} = \boldsymbol{A}(\boldsymbol{r}_0,t) \ . \end{aligned} \tag{4.4}$$

Inserting Eq. (4.4) into the Hamiltonian Eq. (4.2), the time-dependent *Schrödinger equation* Eq. (4.1) becomes

$$\Big[-\frac{1}{2}(\boldsymbol{\nabla} - \mathrm{i}\boldsymbol{A}(\boldsymbol{r}_0,t))^2 + V(\boldsymbol{r})\Big]\psi(\boldsymbol{r},t) = \mathrm{i}\frac{\partial\psi(\boldsymbol{r},t)}{\partial t} \ . \tag{4.5}$$

Eq. (4.5) can be further simplified [74, 75] by defining a new wave function $\phi(\boldsymbol{r},t)$ as

$$\psi(\boldsymbol{r},t) = \mathrm{e}^{\mathrm{i}\chi(\boldsymbol{r},t)}\phi(\boldsymbol{r},t) \ , \tag{4.6}$$

with the phase $\chi(\boldsymbol{r},t) = \boldsymbol{A}(\boldsymbol{r}_0,t)\cdot\boldsymbol{r}$. If $\phi(\boldsymbol{r},t)$ is a solution of the time-dependent Schrödinger equation Eq. (4.1) then so is $\mathrm{e}^{\mathrm{i}\chi(\boldsymbol{r},t)}\phi(\boldsymbol{r},t)$, since the choice of the phase $\chi(\boldsymbol{r},t)$ leaves the probability density $P(\boldsymbol{r},t) = |\psi(\boldsymbol{r},t)|^2$ unaffected. $\psi(\boldsymbol{r},t)$ and $\phi(\boldsymbol{r},t)$ represent the same physical state [74]. Inserting Eq. (4.6) into Eq. (4.5) we find

$$\mathrm{i}\frac{\partial\phi(\boldsymbol{r},t)}{\partial t} = \underbrace{[\widehat{\mathscr{H}_0} - \boldsymbol{r}\cdot\boldsymbol{E}(\boldsymbol{r}_0,t)]}_{\widehat{\mathscr{H}}}\phi(\boldsymbol{r},t) \ , \tag{4.7}$$

where we have used $\boldsymbol{E}(\boldsymbol{r},t) = -\dot{\boldsymbol{A}}(\boldsymbol{r},t)$.

In the *dipole approximation* the Hamiltonian from Eq. (4.2) takes the form

$\widehat{\mathscr{H}} = \widehat{\mathscr{H}_0} + \widehat{\mathscr{H}_{\text{int}}}$, with the unperturbed Hamiltonian $\widehat{\mathscr{H}_0} = \frac{1}{2}\boldsymbol{p}^2 + V(\boldsymbol{r})$ of the free electron and the perturbation $\widehat{\mathscr{H}_{\text{int}}} = -\boldsymbol{r}\cdot\boldsymbol{E}(\boldsymbol{r}_0,t)$, caused by the external electric field. $\widehat{\mathscr{H}_{\text{int}}}$ is the interaction energy of a particle with a dipole moment given by the dipole operator $\boldsymbol{r}$ in an external electric field $\boldsymbol{E}(\boldsymbol{r},t)$.

4.1.2. Density matrix formalism for a two-level atom

The density operator $\hat{\rho}(t)$ [74] is defined as

$$\hat{\rho}(t) = \sum_{\psi} P_{\psi}(t)|\psi\rangle\langle\psi| \ , \tag{4.8}$$

where the Ψ are othogonal states and $P_{\psi}(t)$ is the probability that the system can be found in the state $|\psi\rangle$.

The equation of motion for the density operator, also known as the *von Neumann equation*, can be derived [74] by taking the time derivative of Eq. (4.8) and using the *time-dependent Schrödinger equation*, Eq. (4.1), to obtain

$$\dot{\hat{\rho}}(t) = -\mathrm{i}[\widehat{\mathscr{H}},\hat{\rho}] \ , \tag{4.9}$$

where $\widehat{\mathscr{H}}$ is the Hamiltonian of the system and $[\cdot\ ,\ \cdot]$ denotes a commutator [74]. Since the *von Neumann equation* relies on the density operator $\hat{\rho}$ instead of the state vector $|\psi\rangle$, it allows us to describe mixed states that are statistical mixtures of multiple quantum states, each represented by a different state vector $|\psi_\alpha\rangle$. This is not possible with the *Schrödinger equation* as a state vector $|\psi_\alpha\rangle$ can only represent a pure state which is a coherent superposition of quantum states with each state being weighted by its *probability amplitude* and not the actual *probability* of being observed in a measurement. The *von Neumann equation* is more general [74] than the *Schrödinger equation*. Furthermore, the density matrix allows the description of a system of which we do not have the maximum knowledge allowed by quantum mechanics. This means that the state vector of the system is not known and we only know the probabilities for being in certain states [42]. The density matrix also allows us to consider only a part of a total system by performing a partial trace over the unobserved degrees of freedom. We will use the density matrix to incorporate upper to lower level decays, which cannot be done with state vectors, because the level populations are directly influenced [42].

We incorporate decay rates representing incoherent processes that decrease the occupancy of the levels as illustrated in Fig. (4.2) by adding a relaxation matrix Γ to our Hamiltonian $\widehat{\mathscr{H}}$which is defined as

$$\langle n|\Gamma|m\rangle = \gamma_n\delta_{nm} \ , \tag{4.10}$$

where δ_{nm} is the Kronecker delta symbol. The equation of motion then becomes

$$\dot{\hat{\rho}} = -\mathrm{i}[\mathscr{H},\hat{\rho}] - \frac{1}{2}\{\Gamma,\hat{\rho}\} \ , \tag{4.11}$$

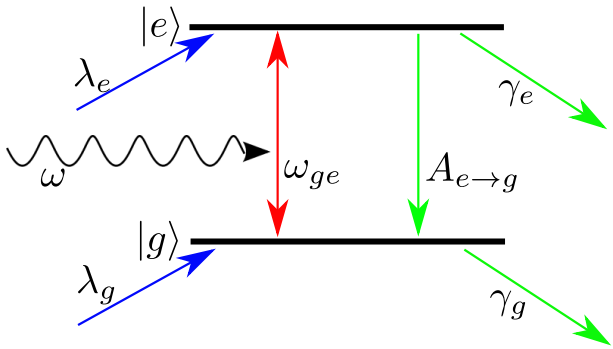

Figure 4.2.: Two-level atom with upper-level pumping and decay rates λ_e and γ_e, respectively, and lower-level pumping and decay rates λ_g and γ_g, respectively. $A_{\mathrm{e}\to\mathrm{g}}$ is the spontaneous emission rate from the upper to the lower level. The transition energy is ω_ge. The atom is interacting with a single-mode electric field of frequency ω.

with the anti-commutator $\{\Gamma,\hat{\rho}\} = \Gamma\hat{\rho} + \hat{\rho}\Gamma$.

We can now derive the equations of motion for the matrix elements of the density operator describing a two-level atom interacting with a single mode field, as shown in Fig. (4.2). In order to do this we would like to find a simpler expression for the Hamiltonian than in Eq. (4.7). We write the electric field of frequency ω as

$$\boldsymbol{E}(\boldsymbol{r}_0,t) = \boldsymbol{E}(t) = \boldsymbol{\epsilon}\cdot E(t)\ , \tag{4.12}$$

where $\boldsymbol{\epsilon}$ defines the polarization of the field. We choose $\boldsymbol{r}_0 = 0$ and for $\boldsymbol{E}(\boldsymbol{r}_0,t)$ to be linearly polarized, so that $\boldsymbol{\epsilon}$ is real. The upper and lower states of the atom are given by $|\mathrm{e}\rangle$ and $|\mathrm{g}\rangle$, respectively. The transition energy is ω_ge. We place the energy zero in the middle between the energy levels and assume that $|\mathrm{e}\rangle$ and $|\mathrm{g}\rangle$ are eigenstates of the unperturbed Hamiltonian $\widehat{\mathscr{H}_0}$ with eigenvalues $\frac{1}{2}\omega_\mathrm{ge}$ and $-\frac{1}{2}\omega_\mathrm{ge}$,

$$\widehat{\mathscr{H}_0}|\mathrm{e}\rangle = \frac{1}{2}\omega_\mathrm{ge}|\mathrm{e}\rangle \tag{4.13}$$

$$\widehat{\mathscr{H}_0}|\mathrm{g}\rangle = -\frac{1}{2}\omega_\mathrm{ge}|\mathrm{g}\rangle\ . \tag{4.14}$$

The wave function of the two-level atom can be written as a linear combination of these states as

$$|\psi(t)\rangle = C_\mathrm{e}(t)|\mathrm{e}\rangle + C_\mathrm{g}|\mathrm{g}\rangle\ , \tag{4.15}$$

with the probability amplitudes $C_\mathrm{e}(t)$ and $C_\mathrm{g}(t)$ for the electron being in the states $|\mathrm{e}\rangle$ or $|\mathrm{g}\rangle$, respectively.

Using the completeness relation $|\mathrm{e}\rangle\langle\mathrm{e}| + |\mathrm{g}\rangle\langle\mathrm{g}| = \mathbf{1}$ and Eqs. (4.13) and (4.14), we can express $\widehat{\mathscr{H}_0}$ and $\widehat{\mathscr{H}_\mathrm{int}}$ in terms of the the eigenstates and eigenvalues of the unperturbed atom as

$$\begin{aligned}\widehat{\mathscr{H}_0} &= (|\mathrm{e}\rangle\langle\mathrm{e}| + |\mathrm{g}\rangle\langle\mathrm{g}|)\widehat{\mathscr{H}_0}(|\mathrm{e}\rangle\langle\mathrm{e}| + |\mathrm{g}\rangle\langle\mathrm{g}|)\\ &= \frac{1}{2}\omega_\mathrm{ge}|\mathrm{e}\rangle\langle\mathrm{e}| - \frac{1}{2}\omega_\mathrm{ge}|\mathrm{g}\rangle\langle\mathrm{g}|\end{aligned} \tag{4.16}$$

and

$$\begin{aligned}\widehat{\mathscr{H}_{\text{int}}} &= -(|\text{e}\rangle\langle\text{e}| + |\text{g}\rangle\langle\text{g}|)r(|\text{e}\rangle\langle\text{e}| + |\text{g}\rangle\langle\text{g}|)E(t) \\ &= -(|\text{e}\rangle r_{\text{eg}}\langle\text{g}| + |\text{g}\rangle r_{\text{ge}}\langle\text{e}|)E(t) \ , \end{aligned} \tag{4.17}$$

with $r_{\text{eg}} = \langle\text{e}|\boldsymbol{r}|\text{g}\rangle \cdot \boldsymbol{\epsilon} = \boldsymbol{r}_{\text{eg}} \cdot \boldsymbol{\epsilon}$ and $r_{\text{ge}} = \langle\text{g}|\boldsymbol{r}|\text{e}\rangle \cdot \boldsymbol{\epsilon} = \boldsymbol{r}_{\text{ge}} \cdot \boldsymbol{\epsilon}$. The dipole operator has odd parity and as a consequence its diagonal elements are zero [52]. The dipole matrix elements r_{eg} and r_{ge} are generally complex and can be written as $r_{\text{eg}} = |r_{\text{eg}}|\text{e}^{\text{i}\phi}$ with phase ϕ. Since the Schrödinger equation is not affected if we multiply the wave function with a constant arbitrary phase, we are free to do the transformation $\psi(\boldsymbol{r}, t) \to \text{e}^{\text{i}\alpha}\psi(\boldsymbol{r}, t)$ [74]. By choosing the correct phase α the dipole matrix elements can be made real, such that $r_{\text{eg}} = r_{\text{ge}} = \wp$ [1]. With Eq. (4.10, 4.11, 4.16, 4.17) we can write the equations of motion for the density matrix elements as

$$\dot{\rho}_{\text{ee}} = -(\gamma_{\text{e}} + A_{\text{e}\to\text{g}})\rho_{\text{ee}} + \text{i}[\wp E(t)\rho_{\text{ge}} - \text{c.c.}] \ , \tag{4.18}$$

$$\dot{\rho}_{\text{gg}} = -(\gamma_{\text{g}} - A_{\text{e}\to\text{g}})\rho_{\text{gg}} - \text{i}[\wp E(t)\rho_{\text{ge}} - \text{c.c.}] \ , \tag{4.19}$$

$$\dot{\rho}_{\text{eg}} = -(\text{i}\omega_{\text{ge}} + \gamma_{\text{eg}})\rho_{\text{eg}} - \text{i}\wp E(t)(\rho_{\text{ee}} - \rho_{\text{gg}}) \ , \tag{4.20}$$

with $\gamma_{\text{eg}} = \frac{1}{2}(\gamma_{\text{e}} + \gamma_{\text{g}} + A_{\text{e}\to\text{g}})$.

Additionally, we have incorporated spontaneous emission [5] into these equations. Population is directly transferred from the upper level $|\text{e}\rangle$ to the lower level $|\text{g}\rangle$ via spontaneous emission which can be taken into account by subtracting $A_{\text{e}\to\text{g}}\rho_{\text{ee}}$ from Eq. (4.18) and adding it to Eq. (4.19) [75]. The spontaneous emission rate [1] is given by

$$A_{\text{e}\to\text{g}} = \frac{4|\boldsymbol{r}_{\text{eg}}|^2\omega_{\text{ge}}^3}{3c^3} \ . \tag{4.21}$$

Furthermore, we would like to incorporate a decay rate γ_{ph} into the equations of motion. Decay processes that cause decoherence, meaning that they cause the decay of non-diagonal elements in the density matrix, but leave the diagonal elements of the density matrix unchanged, are intended to be taken into account by γ_{ph} [1, 42, 75].

We replace γ_{eg} with a total relaxation rate $\gamma = \gamma_{\text{eg}} + \gamma_{\text{ph}}$ in Eq. (4.20)

$$\dot{\rho}_{\text{eg}} = -(\text{i}\omega_{\text{ge}} + \gamma)\rho_{\text{eg}} - \text{i}\wp E(t)(\rho_{\text{ee}} - \rho_{\text{gg}}) \ . \tag{4.22}$$

In the following section we would like to use the density matrix to express the polarization in Maxwell's equations. We present an expression for the atomic polarization [74, 75] in terms of the density matrix elements

$$P(t) = \langle r\rangle = \wp \cdot (\rho_{\text{eg}}(t) + \rho_{\text{ge}}(t)) \ . \tag{4.23}$$

4.2. Maxwell-Schrödinger equations

In the previous section we considered the interaction of the radiation field with a single atom. Now we will investigate the interaction of a single-mode radiation field with a large number of atoms. The most prominent such system is the single-mode laser where

atoms are pumped into an excited state $|e\rangle$ and interact with the radiation field through stimulated emission and absorption [1, 5, 8, 76, 77].

We will describe the atomic response to the incident radiation field and use the population matrix to calculate the polarization of the medium based on the dipole moments of the individual atoms. The population matrix describes the statistical mixture consisting of many identical systems, namely two-level atoms. The induced polarization appears as a source term in the Maxwell equation describing the radiation field giving us a self-consistant set of equations for the medium and the radiation field known as the Maxwell-Schrödinger equations [42, 75]. The material is presented similarly to [1, 75].

4.2.1. Polarization of a two-level medium

We derive the polarization of a one-dimensional gas of homogeneously broadened two-level atoms interacting with an electromagnetic field [75]

$$\boldsymbol{E}(\boldsymbol{r}, t) = \hat{\boldsymbol{\epsilon}} E(z, t) \ , \tag{4.24}$$

propagating along the z-axis with transverse polarization $\hat{\boldsymbol{\epsilon}}$. Each individual atom is described by the density matrix

$$\rho(z, t, t_0) = \begin{pmatrix} \rho_{\mathrm{ee}}(z, t, t_0) & \rho_{\mathrm{eg}}(z, t, t_0) \\ \rho_{\mathrm{ge}}(z, t, t_0) & \rho_{\mathrm{gg}}(z, t, t_0) \end{pmatrix} \ . \tag{4.25}$$

at time t and position z, starting its interaction with the field at time t_0 [75]. The matrix elements in Eq. (4.25) obey the equations of motion given in Eqs. (4.18), (4.19) and (4.22). When the interaction starts at time t_0, every atom is described by

$$\rho_{\alpha\beta}(z, t_0, t_0) = \rho^{(0)}_{\alpha\beta} \ ,$$

where $\rho^{(0)}_{\alpha\beta}$ are the density matrix elements for an atom at time t_0 [75].

The poplations ρ_{ee} and ρ_{gg} are pumped by exciting the atoms to these levels, as seen in Fig. (4.2). The atoms are pumped at a rate $r_\lambda(z, t_0)$ of atoms per second per unit volume. The population matrix describing the system in its entirety is obtained by summing over all initial times t_0 [75]

$$\hat{\rho}(z, t) = \int_{-\infty}^{t} \mathrm{d}t_0 r_\lambda(z, t_0) \hat{\rho}(z, t, t_0) \tag{4.26}$$

$$= \sum_{\alpha,\beta} \int_{-\infty}^{t} \mathrm{d}t_0 r_\lambda(z, t_0) \rho_{\alpha\beta}(z, t, t_0) |\alpha\rangle\langle\beta| \ . \tag{4.27}$$

We assume that the pumping rate $r_\lambda(z, t_0)$ is slowly-varying compared with the matrix elements and is taken to be constant [75]. The contributions of all atoms to the macroscopic polarization of the medium are obtained by summing over all initial times t_0. $P(z, t)$ is caused by all atoms at z at time t, regardless of their time of excitation. With Eq. (4.23)

and Eq. (4.27) we obtain [75]

$$P(z,t) = \sum_{\alpha,\beta} \int_{-\infty}^{t} \mathrm{d}t_0 r_\lambda(z,t_0)\rho_{\alpha\beta}(z,t,t_0)\wp \tag{4.28}$$

$$= \wp(\rho_{\mathrm{ge}}(z,t) + \rho_{\mathrm{eg}}(z,t)) \ . \tag{4.29}$$

The equations of motion for the elements of the population matrix are obtained through the time derivation of Eq. (4.27) and the equations of motion, Eqs. (4.18), (4.19) and (4.22), for the single atom density matrix elements which lead us to

$$\dot{\rho}_{\mathrm{ee}} = \lambda_{\mathrm{e}} - (\gamma_{\mathrm{e}} + A_{\mathrm{e}\to\mathrm{g}})\rho_{\mathrm{ee}} + \mathrm{i}[\wp E(t)\rho_{\mathrm{ge}} - \mathrm{c.c.}] \ , \tag{4.30}$$

$$\dot{\rho}_{\mathrm{gg}} = \lambda_{\mathrm{g}} - (\gamma_{\mathrm{g}} - A_{\mathrm{e}\to\mathrm{g}})\rho_{\mathrm{gg}} - \mathrm{i}[\wp E(t)\rho_{\mathrm{ge}} - \mathrm{c.c.}] \ , \tag{4.31}$$

$$\dot{\rho}_{\mathrm{eg}} = -(\mathrm{i}\omega + \gamma)\rho_{\mathrm{eg}} - \mathrm{i}\wp E(t)(\rho_{\mathrm{ee}} - \rho_{\mathrm{gg}}) \ , \tag{4.32}$$

with initial conditions $\rho_{\mathrm{eg}}^{(0)} = \rho_{\mathrm{ge}}^{(0)} = 0$ and the pumping rates $\lambda_{\mathrm{e}} = r_\lambda \rho_{\mathrm{ee}}^{(0)}$, $\lambda_{\mathrm{g}} = r_\lambda \rho_{\mathrm{gg}}^{(0)}$, as seen in Fig. (4.2)

From this point forward we consider a laser field of the form

$$E(z,t) = \frac{1}{2}\mathscr{E}(z,t)\mathrm{e}^{-\mathrm{i}(\omega t - z/c)} + \mathrm{c.c.} \ , \tag{4.33}$$

propagating in the positive z-direction with transverse polarization. $\mathscr{E}(z,t)$ is the electric field envelope. We assume that $\mathscr{E}(z,t)$ is slowly-varying in space and time compared to $\mathrm{e}^{-\mathrm{i}(\omega t - z/c)}$ which means that $\mathscr{E}(z,t)$ is nearly constant over the time period $1/\omega$ [75]. This approximation is commonly made for narrowband radiation [78], thus it is reasonable for laser light. With this ansatz for the driving electric field the linear response of the medium [1, 75] is given by

$$P(z,t) = \frac{1}{2}\mathscr{P}(z,t)\mathrm{e}^{-\mathrm{i}(\omega t - z/c)} + \mathrm{c.c.} \ , \tag{4.34}$$

where $\mathscr{P}(z,t)$ is also slowly-varying [75] and can be determined by comparison of Eq. (4.34) with Eq. (4.29) to be

$$\mathscr{P}(z,t) = 2\wp\rho_{\mathrm{eg}}\mathrm{e}^{\mathrm{i}\omega(t-z/c)} \ . \tag{4.35}$$

In order to determine the induced polarization we need to determine the time evolution of $\rho_{\mathrm{eg}}(z,t)$ under the influence of the electric field $E(z,t)$. For this purpose we will integrate $\dot{\rho}_{\mathrm{eg}}(z,t)$ from Eq. (4.32) using the *rate equation approximation* [75]. Formally $\dot{\rho}_{\mathrm{eg}}(z,t)$ can be integrated to give

$$\rho_{\mathrm{eg}}(z,t) = -\frac{\mathrm{i}}{2}\int_{\infty}^{t} \mathrm{d}t' \mathrm{e}^{-(\mathrm{i}\omega_{\mathrm{ge}}+\gamma)(t-t')}\wp\mathscr{E}(z,t')\mathrm{e}^{-\mathrm{i}\omega(t'-z/c)}[\rho_{\mathrm{ee}}(z,t') - \rho_{\mathrm{gg}}(z,t')] \ . \tag{4.36}$$

In the *rate equation approximation* we assume that the off-diagonal damping rate γ is so large that $\mathscr{E}(z,t')$ and $[\rho_{\mathrm{ee}}(z,t') - \rho_{\mathrm{gg}}(z,t')]$ are nearly constant over intervals $\sim 1/\gamma$ in Eq. (4.36). This assumption means that the decay rate in Eq. (4.22) and Eq. (4.32) is approximately

$$\gamma \approx \gamma_{\mathrm{ph}} \gg \gamma_{\mathrm{eg}} \ . \tag{4.37}$$

This is a reasonable assumption for the photoionization pumped XRL described on page 3 and page 37 as several processes lead to strong decoherence in the system: photoionization and Auger decay produce free electrons which we do not explicitly consider after performing a partial trace over the density matrix of the entire system, leading to loss of information; strong electromagnetic fields are present in the plasma column causing interaction of the neon gas with its surroundings; elastic collisions between atoms cause dephasing of the atomic dipole moments; the x-ray FEL pump pulse has a very short coherence time.

With Eq. (4.37) we can evaluate the field envelope and population difference at time t and calculate the integral [75]:

$$\begin{aligned}
(4.36) &= -\frac{\mathrm{i}}{2}\wp\mathscr{E}(z,t)[\rho_{\mathrm{ee}}(z,t)-\rho_{\mathrm{gg}}(z,t)]\int_{\infty}^{t}\mathrm{d}t'\mathrm{e}^{-(\mathrm{i}\omega_{\mathrm{ge}}+\gamma)(t-t')}\mathrm{e}^{-\mathrm{i}\omega(t'-z/c)} \\
&= -\frac{\mathrm{i}}{2}\wp\mathscr{E}(z,t)\mathrm{e}^{-\mathrm{i}\omega(t-z/c)}[\rho_{\mathrm{ee}}(z,t)-\rho_{\mathrm{gg}}(z,t)]\int_{\infty}^{t}\mathrm{d}t'\mathrm{e}^{-(\mathrm{i}(\omega_{\mathrm{ge}}-\omega)+\gamma)(t-t')} \\
&= -\frac{\mathrm{i}}{2}\wp\mathscr{E}(z,t)\mathrm{e}^{-\mathrm{i}\omega(t-z/c)}[\rho_{\mathrm{ee}}(z,t)-\rho_{\mathrm{gg}}(z,t)]\frac{1-\mathrm{e}^{-(\gamma+\mathrm{i}(\omega_{\mathrm{ge}}-\omega))t}}{\gamma+\mathrm{i}(\omega_{\mathrm{ge}}-\omega)}\ . \qquad (4.38)
\end{aligned}$$

Evaluating Eq. (4.38) for times $t \gg \gamma^{-1}$ we get

$$\rho_{\mathrm{eg}}(z,t) = -\frac{\mathrm{i}}{2}\wp\mathscr{E}(z,t)\mathrm{e}^{-\mathrm{i}\omega(t-z/c)}\frac{[\rho_{\mathrm{ee}}(z,t)-\rho_{\mathrm{gg}}(z,t)]}{\gamma+\mathrm{i}(\omega_{\mathrm{ge}}-\omega)}\ . \qquad (4.39)$$

For this approximation to be valid $\mathscr{E}(z,t)$ and $[\rho_{\mathrm{ee}}(z,t)-\rho_{\mathrm{gg}}(z,t)]$ must be slowly-varying in time compared to $\mathrm{e}^{-\gamma t}$. The field envelope $\mathscr{E}(z,t)$ satisfies this condition by definition and $[\rho_{\mathrm{ee}}(z,t)-\rho_{\mathrm{gg}}(z,t)]$ can be expected to be slowly varying if γ satisfies Eq. (4.37). Substituting this result for $\rho_{\mathrm{eg}}(z,t)$ into Eq. (4.30) and Eq. (4.31) we obtain rate equations for the populations of the upper and lower levels [75]

$$\begin{aligned}
\dot{\rho}_{\mathrm{ee}}(z,t) &= \lambda_{\mathrm{e}} - (\gamma_{\mathrm{e}}+A_{\mathrm{e}\to\mathrm{g}})\rho_{\mathrm{ee}}(z,t) - R[\rho_{\mathrm{ee}}(z,t)-\rho_{\mathrm{gg}}(z,t)], \qquad (4.40)\\
\dot{\rho}_{\mathrm{gg}}(z,t) &= \lambda_{\mathrm{g}} - (\gamma_{\mathrm{g}}-A_{\mathrm{e}\to\mathrm{g}})\rho_{\mathrm{gg}}(z,t) + R[\rho_{\mathrm{gg}}(z,t)-\rho_{\mathrm{gg}}(z,t)], \qquad (4.41)
\end{aligned}$$

with

$$R = \frac{1}{2}\left|\frac{\wp\mathscr{E}(z,t)}{\hbar}\right|^2\frac{\gamma}{\gamma^2+(\omega_{\mathrm{ge}}-\omega)^2}\ . \qquad (4.42)$$

The off-diagonal elements of the population matrix have been completely eliminated and the populations ρ_{ee} and ρ_{gg} are coupled to each other. Since we derived the population matrix by summing over all density matrices representing atoms that have contributions at one point in space and time, the population matrix elements ρ_{ee} and ρ_{gg} can take on values between 0 and the atom density n_{A}.

4.2.2. Propagation of the pulse

The electromagnetic field is described by Maxwell's equations [54]

$$\boldsymbol{\nabla}\cdot\boldsymbol{D} = 0, \tag{4.43}$$

$$\boldsymbol{\nabla}\times\boldsymbol{E} = -\frac{\partial\boldsymbol{B}}{\partial t}\ , \tag{4.44}$$

$$\boldsymbol{\nabla}\cdot\boldsymbol{B} = 0, \tag{4.45}$$

$$\boldsymbol{\nabla}\times\boldsymbol{H} = \frac{\partial\boldsymbol{D}}{\partial t}+\boldsymbol{J}\ , \tag{4.46}$$

where $\boldsymbol{D}=\frac{1}{4\pi}\boldsymbol{E}+\boldsymbol{P}$, $\boldsymbol{B}=\frac{4\pi}{c^2}\boldsymbol{H}$ and $\boldsymbol{J}=\sigma\boldsymbol{E}$, with the electric field $\boldsymbol{E}$, the electrical flux density $\boldsymbol{D}$, the magnetic flux density $\boldsymbol{B}$, the magnetic field $\boldsymbol{H}$, the macroscopic polarization $\boldsymbol{P}$, the current density $\boldsymbol{J}$ and the conductivity σ. We neglect the ohmic losses and assume $\sigma=0$ [75].

Since $\boldsymbol{P}$ appears in Maxwell's equations as source term, meaning that it contributes to the electric field, we derive the effect that the induced polarization has on electromagnetic waves traveling through the medium. We can derive the wave equation [54] by using the definitions of $\boldsymbol{D}$ and $\boldsymbol{H}$, taking the time derivative of Eq. (4.46), the curl of Eq. (4.44) and appropriately combining the expressions to obtain

$$\boldsymbol{\nabla}\times(\boldsymbol{\nabla}\times\boldsymbol{E})+\frac{1}{c^2}\frac{\partial^2\boldsymbol{E}}{\partial t^2}=-\frac{1}{4\pi c^2}\frac{\partial^2\boldsymbol{P}}{\partial t^2}\ . \tag{4.47}$$

Inserting Eq. (4.24) into Eq. (4.47) and using the general identity [54]

$$\boldsymbol{\nabla}\times(\boldsymbol{\nabla}\times\boldsymbol{E})=\boldsymbol{\nabla}(\boldsymbol{\nabla}\cdot\boldsymbol{E})-\boldsymbol{\nabla}^2\boldsymbol{E} \tag{4.48}$$

of vector calculus, we obtain

$$\frac{\partial^2}{\partial z^2}E(z,t)-\frac{1}{c^2}\frac{\partial^2}{\partial t^2}E(z,t)=\frac{4\pi}{c^2}\frac{\partial^2}{\partial t^2}P(z,t)\ , \tag{4.49}$$

where we have neglected the x- and y-dependence of the electric field. The effects of diffraction and atomic attenuation or amplification are very small on the transverse profile of a well-collimated laser pulse on the scale of the laser wavelength c/ω [79]. This means that the transverse derivates and especially the transverse second derivatives are so small that we can assume

$$\left|\frac{\partial^2}{\partial x^2}E(x,y,z,t)\right|=\left|\frac{\partial^2}{\partial y^2}E(x,y,z,t)\right|\approx 0\ ,$$

and, henceforth use the reduced wave equation [75] in Eq. (4.49).

We use the ansatz in Eq. (4.33) for the electric field and the ansatz in Eqs. (4.34) and (4.35) for the polarization. We have assumed that $\mathscr{E}(z,t)$ and $\mathscr{P}(z,t)$ are slowly-varying compared to $e^{-i(\omega t-z/c)}$ and make the slowly-varying envelope approximations [42]

$$\left|\frac{\partial\mathscr{E}}{\partial t}\right| \ll \left|\nu\mathscr{E}\right|\ ,\quad \left|\frac{\partial\mathscr{E}}{\partial z}\right|\ll\left|\frac{\nu}{c}\mathscr{E}\right|\ , \tag{4.50}$$

$$\left|\frac{\partial\mathscr{E}}{\partial t}\right| \ll \left|\nu\mathscr{E}\right|\ ,\quad \left|\frac{\partial\mathscr{E}}{\partial z}\right|\ll\left|\frac{\nu}{c}\mathscr{E}\right|\ , \tag{4.51}$$

and analogously the same approximations for the envelope of the polarization $\mathscr{P}(z,t)$. Eq. (4.49) can be rewritten using the identity

$$\frac{\partial^2}{\partial z^2}E(z,t) - \frac{1}{c^2}\frac{\partial^2}{\partial t^2}E(z,t) = \Big(\frac{\partial}{\partial z} + \frac{1}{c}\frac{\partial}{\partial t}\Big)\Big(-\frac{\partial}{\partial z} + \frac{1}{c}\frac{\partial}{\partial t}\Big)E(z,t)\ , \tag{4.52}$$

with the approximations in Eq. (4.50) and in Eq. (4.51) we then derive [75]

$$\Big(-\frac{\partial}{\partial z} + \frac{1}{c}\frac{\partial}{\partial t}\Big)E(z,t) \approx 2\mathrm{i}\frac{\omega}{c}E(z,t)\ . \tag{4.53}$$

By applying Eq. (4.52) and Eq. (4.53) to the left side of the one-dimensional wave equation Eq. (4.49) and the slowly-varying envelope approximations for $\mathscr{P}(z,t)$ to the right side, we can derive an approximated equation for the propagation of the electric field through the medium [75]

$$\frac{\partial}{\partial z}\mathscr{E}(z,t) + \frac{1}{c}\frac{\partial}{\partial t}\mathscr{E}(z,t) = \frac{2\pi\mathrm{i}\omega}{c}\mathscr{P}(z,t) \tag{4.54}$$

$$= \frac{4\pi\mathrm{i}\omega}{c}\wp\rho_{\mathrm{eg}}\mathrm{e}^{\mathrm{i}\omega(t-z/c)}\ . \tag{4.55}$$

By inserting Eq. (4.39) for ρ_{eg} we obtain

$$\begin{aligned}\frac{\partial}{\partial z}\mathscr{E}(z,t) + \frac{1}{c}\frac{\partial}{\partial t}\mathscr{E}(z,t) &= \frac{2\pi\omega}{c}\wp^2\mathscr{E}(z,t)\frac{[\rho_{\mathrm{ee}}(z,t)-\rho_{\mathrm{gg}}(z,t)]}{\gamma+\mathrm{i}(\omega_{\mathrm{ge}}-\omega)}\\ \Longleftrightarrow \mathscr{E}^*\frac{\partial\mathscr{E}}{\partial z} + \frac{1}{c}\mathscr{E}^*\frac{\partial\mathscr{E}}{\partial t} &= \frac{2\pi\omega}{c}\wp^2|\mathscr{E}|^2\frac{\rho_{\mathrm{ee}}-\rho_{\mathrm{gg}}}{\gamma+\mathrm{i}(\omega_{\mathrm{ge}}-\omega)}\ ,\end{aligned} \tag{4.56}$$

where we have multiplied both sides with $\mathscr{E}^*$. Now we would like to derive a rate equation for the radiation field in terms of its intensity. In order to achieve this we add Eq. (4.56) to its complex conjugate [1] and use the relations

$$\mathscr{E}^*\frac{\partial\mathscr{E}}{\partial t} + \mathscr{E}\frac{\partial\mathscr{E}^*}{\partial t} = \frac{\partial|\mathscr{E}|^2}{\partial t}\ ,$$

and

$$\mathscr{E}^*\frac{\partial\mathscr{E}}{\partial z} + \mathscr{E}\frac{\partial\mathscr{E}^*}{\partial z} = \frac{\partial|\mathscr{E}|^2}{\partial z}\ ,$$

to obtain

$$\frac{\partial}{\partial z}|\mathscr{E}(z,t)|^2 + \frac{1}{c}\frac{\partial}{\partial t}|\mathscr{E}(z,t)|^2 = \frac{4\pi\omega}{c}\wp^2|\mathscr{E}(z,t)|^2\frac{\gamma[\rho_{\mathrm{ee}}-\rho_{\mathrm{gg}}]}{\gamma^2+(\omega_{\mathrm{ge}}-\omega)^2} \tag{4.57}$$

$$\Longleftrightarrow \frac{\partial}{\partial z}I(z,t) + \frac{1}{c}\frac{\partial}{\partial t}I(z,t) = \frac{4\pi\omega}{c}\wp^2 I(z,t)\frac{\gamma[\rho_{\mathrm{ee}}-\rho_{\mathrm{gg}}]}{\gamma^2+(\omega_{\mathrm{ge}}-\omega)^2}\ . \tag{4.58}$$

This gives us a rate equation describing the propagation of the intensity of a plane wave in a medium composed of homogeneously broadened two-level atoms.

Eqs. (4.40), (4.41) and (4.58) give us a set of coupled partial differential equations describing the atom-field interactions. When the off-diagonal population matrix elements relax quickly compared to the temporal variations of the population difference $\rho_{\mathrm{ee}} - \rho_{\mathrm{gg}}$ and the electric field amplitude $\mathscr{E}(z,t)$, we can use the rate equation approximation and disregard the off-diagonal elements of the population matrix.

4.2.3. Orientational average

All three of the rate equations contain $|\wp|^2 = |\boldsymbol{r}_{\mathrm{eg}} \cdot \boldsymbol{\epsilon}\,|^2$, which is the scalar product of the transition dipole matrix element and the polarization vector. We would like to rewrite the rate equations using the stimulated emission cross section σ_{se} and the absorption cross section σ_{abs}. These are more practical, as $|\wp|^2$ depends on the relative orientation of $\boldsymbol{r}_{\mathrm{eg}}$ and $\boldsymbol{\epsilon}$, which, in the case of unknown polarization of the radiation or due to rotational and collisional disorientation, is not constant in time nor the same for all atoms in a gas [1]. For this reason the orientational average of $\boldsymbol{r}_{\mathrm{eg}}$ and $|\boldsymbol{\epsilon}|^2$ needs to be used.

To insert the orientational average into the rate equations, we must calculate the spherical average of $\wp^2 = (\boldsymbol{r}_{\mathrm{eg}} \cdot \boldsymbol{\epsilon})^2$ over all possible relative angles between $\boldsymbol{r}_{\mathrm{eg}}$ and $\boldsymbol{\epsilon}$ [1]. We write $\wp^2 = |\boldsymbol{r}_{\mathrm{eg}}|^2 \cdot |\boldsymbol{\epsilon}|^2 \cdot \cos^2\theta$ and use this expression in our calculations

$$\begin{aligned} \langle (\boldsymbol{r}_{\mathrm{eg}} \cdot \boldsymbol{\epsilon})^2 \rangle_{\mathrm{orientational}} &= \frac{1}{4\pi} \int_{\vartheta=0}^{\pi} \int_{\varphi=0}^{2\pi} |\boldsymbol{r}_{\mathrm{eg}}|^2 \cdot |\boldsymbol{\epsilon}|^2 \cdot \cos^2\vartheta \sin\vartheta \mathrm{d}\vartheta \mathrm{d}\varphi \\ &= \frac{1}{3} |\boldsymbol{r}_{\mathrm{eg}}|^2 \cdot |\boldsymbol{\epsilon}|^2 = \frac{c^3}{4\omega_{\mathrm{ge}}^3} A_{\mathrm{e}\to\mathrm{g}} \ , \end{aligned} \tag{4.59}$$

where in the last step we have used $|\boldsymbol{\epsilon}| = 1$ and Eq. (4.21) for the spontaneous emission rate [1]. With the orientational average from Eq. (4.59) we can write Eq. (4.42) as

$$\frac{1}{2} \langle \Omega_{\mathrm{R}} \rangle_{\mathrm{orietational}} \cdot \frac{\gamma}{\gamma^2 + (\omega_{\mathrm{ge}} - \omega)^2} = \underbrace{\frac{1}{\omega} \frac{\lambda^2 A_{\mathrm{e}\to\mathrm{g}}}{8\pi} \cdot L(\omega)}_{\frac{\sigma_{se}(\omega)}{\omega}} \tag{4.60}$$

where have used $\lambda = 2\pi c/\omega_{\mathrm{ge}}$ and the Lorentzian line shape function

$$L(\omega) = \frac{\Delta\omega_{\mathrm{ge}}/\pi}{\Delta\omega_{\mathrm{ge}}^2 + (\omega_{\mathrm{ge}} - \omega)^2} \ , \tag{4.61}$$

with $\Delta\omega_{\mathrm{ge}} = \gamma/2\pi$, which is the width of the laser transition. The right-hand side of Eq. (4.60) is the stimulated emission cross section $\sigma_{\mathrm{se}}(\omega)$ [1] divided by ω. For nondenerate levels the absorption cross section $\sigma_{\mathrm{abs}}(\omega)$ [1] is just equal to $\sigma_{\mathrm{se}}(\omega)$, however, for degenerate levels the relationship becomes $\sigma_{\mathrm{abs}}(\omega) = \frac{g_{\mathrm{e}}}{g_{\mathrm{g}}} \sigma_{\mathrm{se}}(\omega)$ [1], where g_{e} is the degeneracy of the upper level and g_{g} is the degeneracy of the lower level. To generalize the rate equations to a system with degenerate levels [1] we write Eqs. (4.40) (4.41) with the stimulated emission cross section and with the absorption cross section

$$\begin{aligned} \dot{\rho}_{\mathrm{ee}}(z,t) &= \lambda_{\mathrm{e}} - (\gamma_{\mathrm{e}} + A_{\mathrm{e}\to\mathrm{g}}) \rho_{\mathrm{ee}}(z,t) \\ &\quad - \frac{I(z,t)}{\omega} [\sigma_{\mathrm{se}}(\omega) \rho_{\mathrm{ee}}(z,t) - \sigma_{\mathrm{abs}}(\omega) \rho_{\mathrm{gg}}(z,t)] \ , \end{aligned} \tag{4.62}$$

$$\begin{aligned} \dot{\rho}_{\mathrm{gg}}(z,t) &= \lambda_{\mathrm{g}} - (\gamma_{\mathrm{g}} - A_{\mathrm{e}\to\mathrm{g}}) \rho_{\mathrm{gg}}(z,t) \\ &\quad + \frac{I(z,t)}{\omega} [\sigma_{\mathrm{se}}(\omega) \rho_{\mathrm{ee}}(z,t) - \sigma_{\mathrm{abs}}(\omega) \rho_{\mathrm{gg}}(z,t)] \ . \end{aligned} \tag{4.63}$$

Analogously, we can write Eq. (4.58) using the cross sections as

$$\frac{\partial}{\partial z} I(z,t) + \frac{1}{c} \frac{\partial}{\partial t} I(z,t) = \frac{I(z,t)}{\omega} [\sigma_{\mathrm{se}}(\omega) \rho_{\mathrm{ee}} - \sigma_{\mathrm{abs}}(\omega) \rho_{\mathrm{gg}}] \ . \tag{4.64}$$

4.2.4. Saturation and the gain coefficient

With the coupled rate equations in Eq. (4.62 - 4.64) we can calculate the populations $\rho_{ee}(z,t)$ and $\rho_{gg}(z,t)$ of the upper and lower levels of the two-level medium at any point in space and time, as well as the field intensity $I(z,t)$ or the photon flux $\Phi(z,t) = \frac{I(z,t)}{\omega}$. These equations enable us to calculate the output intensity of a laser, the resulting pulse shape, as well as the gain which we will discuss momentarily.

For a laser transition with degenerate levels, the gain cross section [1] is defined as

$$g(z,t) = [\sigma_{se}(\omega)\rho_{ee}(z,t) - \sigma_{abs}(\omega)\rho_{gg}(z,t)] \ . \tag{4.65}$$

Inserting the expression for the gain cross section into Eq. (4.64) gives

$$\frac{\partial}{\partial z}I(z,t) + \frac{1}{c}\frac{\partial}{\partial t}I(z,t) \ = \ \frac{I(z,t)}{\omega}g(z,t) \ . \tag{4.66}$$

The gain cross section is a measure for how strongly electromagnetic radiation with frequency ω is amplified in a medium. Amplification only takes place if there is a population inversion in the medium, otherwise the pulse is attenuated through absorption. The gain cross section is a very intuitive physical value, as when a photon interacts with an atom it can cause stimulated emission of a further photon, if the atom is excited, or it can be absorbed, if the atom is in the lower state of the resonant transition. The net effect of the medium on the incident pulse is amplifying, only if more atoms are in the excited state than in the lower state. The amplification of the pulse is exponential at low intensities [1], when the stimulated emission rate $\sigma_{se}\frac{I(z,t)}{\omega}$ and the absorption rate $\sigma_{abs}\frac{I(z,t)}{\omega}$ are so small that their effect on the populations in Eq. (4.62) and Eq. (4.63), respectively, can be neglected. The small-signal gain (SSG) cross section [1] describes the amplification of the pulse in this low-intensity regime. It is defined the same as the gain in Eq. (4.65) with the difference that stimulated emission and absorption are neglected when calculating the populations $\rho_{gg}(z,t)$ and $\rho_{ee}(z,t)$. However, as the pulse propagates through the medium its intensity increases and eventually reaches saturation, remaining constant beyond this point. Saturation sets in because the stimulated emission rate in Eq. (4.62) increases together with the field intensity $I(z,t)$, reducing the upper level population, which results in a smaller gain $g(z,t)$. The saturation intensity I_{sat} is defined as the intensity, at which the total exit rate of the upper level $\Delta\omega_e$ equals the rate of stimulated emission [37]. We use the stimulated emission cross section evaluated at the peak of the line profile

$$\sigma_{se}(\omega_{ge}) = A_{e\to g}\frac{2\pi c^2}{\omega_{ge}^2\Delta\omega_{ge}} \ , \tag{4.67}$$

for the definition of I_{sat}:

$$\sigma_{se}(\omega_{ge})\frac{I_{sat}}{\omega} \ = \ \Delta\omega_e \tag{4.68}$$

$$\Longleftrightarrow I_{sat} \ = \ \frac{\Delta\omega_e\omega_{ge}^3\Delta\omega_{ge}}{A_{e\to g}2\pi c^2} \ . \tag{4.69}$$

5. Control of x-ray absorption by an optical laser

This chapter deals with the coherent preparation of atomic states by laser radiation which has proven to be an efficient method to change the optical properties of a gaseous atomic medium [80]. In this setup a strong optical laser is used to control the absorption properties of a dilute neon gas for a weak x-ray probe. The optical properties of atoms are derived from their energy-level structure [80]. The medium's modified response to the x-ray probe is achieved through the optically induced coherence of atomic states, thereby, changing the energy-level structure of the states that define the interaction. It is possible to almost eliminate absorption at the resonance frequency of a transition through destructive interference of alternate excitation pathways [81].

The optically induced modulation of x-ray absorption by neon atoms described in this chapter is used to exert control over an XRL as explained in chapter 7.

5.1. Autler-Townes splitting and electromagnetically induced transparancy

At first, let us consider a strong coupling laser with electric field $\mathbf{E}_c$ resonantly interacting with a two-level atom, see Fig. (5.1). Since the interaction with $\mathbf{E}_c$ is strong, it cannot be treated perturbatively [42] and needs to be taken into account to all orders.

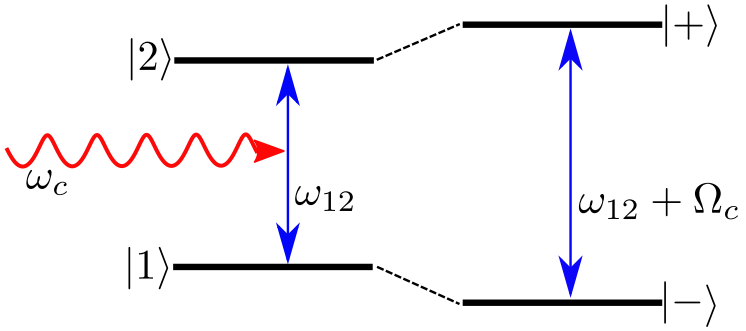

Figure 5.1.: Juxtaposition of bare states (left) and dressed states (right) picture of a two-level atom with transition frequency ω_{12} coupled to a single mode field with frequency ω_c .

This system is described by the Hamiltonian [42]

$$\widehat{\mathscr{H}} = \underbrace{\frac{1}{2}\omega_{12}\hat{\sigma}_z}_{\widehat{\mathscr{H}_0}} \underbrace{- \frac{1}{2}\Omega_c(\hat{\sigma}_- e^{i\omega_c t} + \hat{\sigma}_+ e^{-i\omega_c t})}_{\widehat{\mathscr{H}_{int}}} \tag{5.1}$$

where $\hat{\sigma}_z$, $\hat{\sigma}_-$ and $\hat{\sigma}_+$ are the Pauli spin matrices [74], ω_{12} is the transition frequency and Ω_c is the Rabi frequency [42]. The energy zero has been chosen to be in the middle between $|1\rangle$ and $|2\rangle$. The unperturbed atom is described by $\widehat{\mathscr{H}_0}$ and the interaction is described by $\widehat{\mathscr{H}_{int}}$. It is convenient to introduce a new set of states $|+\rangle$ and $|-\rangle$ that diagonalize the interaction Hamiltonian $\widehat{\mathscr{H}_{int}}$ [42]. The states $|+\rangle$ and $|-\rangle$ are eigenstates of $\widehat{\mathscr{H}_{int}}$ and are called dressed states. They can be expressed as a linear combination of the bare states $|1\rangle$ and $|2\rangle$. At resonance the dressed states are

$$|+\rangle = \frac{1}{\sqrt{2}}\{|1\rangle + |2\rangle\} , \tag{5.2}$$

$$|-\rangle = \frac{1}{\sqrt{2}}\{|1\rangle - |2\rangle\} . \tag{5.3}$$

In a rotating frame the eigenstates $|+\rangle$ and $|-\rangle$ of the interaction Hamiltonian $\widehat{\mathscr{H}_{int}}$ have the eigenvalues $\pm\frac{1}{2}\Omega_c$ [80]. It is apparent that the coupling due to the laser leads to a shift of the atom's energy levels by $\frac{1}{2}\Omega_c$. Here, $|+\rangle$ is shifted up by $\frac{1}{2}\Omega_c$ and $|-\rangle$ is shifted down by $\frac{1}{2}\Omega_c$, resulting in the energy level structure displayed on the right-hand side of Fig. (5.1). The dressed states picture was first introduced by Autler and Townes [82]. The energy shift due to the coupling is referred to as Autler-Townes splitting.

The dressed states picture can also be applied to a three-level atom interacting with a two-mode field [80], as shown in Fig. (5.2a). A strong coupling laser with electric field

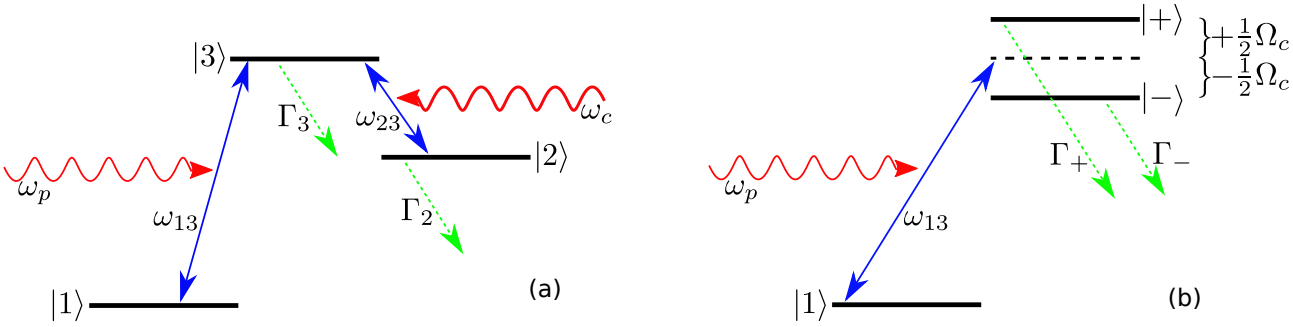

Figure 5.2.: a) Bare states picture of a 3-level atom interacting with a two-mode field. The probe with photon energy ω_p is near resonant with the transition energy ω_{13}, while the coupling field with photon energy ω_c is on resonance with the transition energy ω_{23}. b) Dressed states picture of the 3-level atom assuming $\Omega_p \ll \Omega_c$. The decay rates of the Autler-Townes doubletts $|+\rangle$ and $|-\rangle$ are denoted by Γ_+ and Γ_-, respectively.

$\mathbf{E}_c$ resonantly drives the $|2\rangle$–$|3\rangle$ transition and a probe laser with electric field $\mathbf{E}_p$ drives the $|1\rangle$–$|3\rangle$ transition near resonance with detuning $\delta = \omega_{13} - \omega_p$. For a three-level atom

three dressed states $|0\rangle$, $|-\rangle$ and $|+\rangle$ exist [80]. In general the dressed states $|\pm\rangle$ are linear combinations of all of the bare states $|1\rangle$, $|2\rangle$ and $|3\rangle$, while $|0\rangle$ has no contribution from the bare state $|3\rangle$. We assume the case of a weak probing field, such that $\Omega_\mathrm{p} \ll \Omega_\mathrm{p}$ is true for the two Rabi frequencies. Then, the ground state $|1\rangle$ of the atom is unperturbed by the weak probe and does not mix with other energy levels. The resulting situation is shown in Fig. (5.2b), where $|\pm\rangle$ do not have contributions from $|1\rangle$. The effect of Autler-Townes splitting on the optical properties of an atom can be investigated with help of the linear susceptibility $\chi^{(1)}(\omega_\mathrm{p})$ [54].

We are particularly interested in the the absorption of the probe, which is described by the imaginary part $\Im[\chi^{(1)}(\omega_\mathrm{p})]$. The absorption cross section $\sigma(\omega_\mathrm{p})$ [19] is related to the susceptibility through

$$\sigma(\omega_\mathrm{p}) = n_\mathrm{A}\Im[\chi^{(1)}(\omega_\mathrm{p})] \ , \tag{5.4}$$

where n_A is the atomic number density. If the probe is tuned to the transition frequency of the unperturbed atom, such that $\omega_\mathrm{p} = \omega_{13}$, hardly any absorption occurs as the field is in fact off resonant to the transition into the laser dressed states $|+\rangle$ and $|-\rangle$. Pronounced absorption peaks can be found for field frequencies $\omega_\mathrm{p} = \omega_{13} \pm \frac{1}{2}\Omega_\mathrm{c}$ which are due to resonant excitation into the Autler-Townes doubletts formed by $|+\rangle$ and $|-\rangle$, as shown by the blue line in Fig. (5.3).

Another effect that arises in a 3-level system driven by a two-mode field as described above that can cause a transparency window in the absorption cross section is electromagnetically induced transparency (EIT) [81, 83, 84]. EIT causes a narrow absorption minimum for a resonant ($\omega_\mathrm{p} = \omega_{13}$) probe field $\mathbf{E}_\mathrm{p}$, as shown by the red line in Fig. (5.3). The difference between Autler-Townes splitting and EIT becomes evident by comparing $\sigma(\omega_\mathrm{p})$ for both cases. EIT does not cause splitting and shifting of the resonances away from $\delta = 0$. Instead, EIT leaves the overall shape of $\sigma(\omega_\mathrm{p})$ unchanged, only causing a sudden dip at resonance, resulting in a spectrally narrow transparency window. The underlying mechanism of EIT is the laser-induced coherence of atomic states [80], which leads to destructive interference between alternate excitation pathways between atomic states.

There are two physically intuitive ways of viewing EIT [80]. In the first one [81, 85, 86] the dressed states $|\pm\rangle$ are viewed as closely spaced resonances which are assumed to decay into the same continuum via an Auger process with the decay rates Γ_+ and Γ_-. If the atom is excited by the probe laser from its groundstate $|1\rangle$, the continuum can be reached via decay from either of the excited states $|+$ or $|-\rangle$. These two alternate pathways from $|1\rangle$ to the continuum interfere with each other. If the probe laser is tuned to ω_{13}, then the atom is equally likely to be excited into either the state $|+\rangle$ or into the state $|-\rangle$. Both excitation pathways, $|1\rangle \rightarrow |+\rangle$ and $|1\rangle \rightarrow |-\rangle$, contribute equally and with opposite signs to the linear susceptibility resulting in the cancellation of the atomic response due to destructive interference [87, 88]. The distance between the resonances, which is Ω_c for a resonant coupling field $\mathbf{E}_\mathrm{c}$, must be comparable to or less than their decay widths for interference to be significant. Alternatively, in the bare states picture EIT can be understood as destructive interference of the transitions between the bare states $|1\rangle$,$|2\rangle$ and $|3\rangle$ [80]. The fields $\mathbf{E}_\mathrm{p}$ and $\mathbf{E}_\mathrm{c}$ transfer a small amplitude into state $|2\rangle$.

This means that the amplitude of state $|3\rangle$ is driven directly via the pathway $|1\rangle$–$|3\rangle$ and indirectly via the pathway $|1\rangle$–$|3\rangle$–$|2\rangle$–$|3\rangle$ or higher-order combinations. A further consequence of assuming $\Omega_p \ll \Omega_c$, is that the indirect excitation has equal magnitude to the direct excitation despite the small amplitude of state $|2\rangle$. An essential assumption that needs to be made for this scheme to work is that $|2\rangle$ is a (meta-)stable state, such that $|3\rangle$ is the only decaying state and thus the only way to absorption. This is the key difference between EIT and Autler-Townes splitting, for which this condition need not be met. Whether EIT or Autler-Townes splitting is responsible for reduced or even vanishing absorption depends on the exact combination of parameters as shall be illustrated with the absorption cross section $\sigma(\delta)$ as a function of detuning in the vicinity of the $|1\rangle$–$|3\rangle$ transition. For a system as depicted in Fig. (5.2), the following relation holds true for the absorption cross section [84]

$$\sigma(\delta) \quad = \quad \sigma_0 \frac{\delta^2\gamma_{31}^2 + \gamma_{21}\gamma_{31}(\Omega_c^2/4 + \gamma_{21}\gamma_{31})}{[\Omega_c^2/4 + \gamma_{21}\gamma_{31} - \delta^2]^2 + [\delta(\gamma_{21} + \gamma_{31})]^2} \tag{5.5}$$

where σ_0 is the peak absorption cross section in the absence of the coupling laser and $\gamma_{21} = \Gamma_2/2 + \gamma_{d,2}$ and $\gamma_{31} = \Gamma_3/2 + \gamma_{d,3}$ are decay rates for the coherences between states $|1\rangle$ and $|2\rangle$ and between states $|1\rangle$ and $|3\rangle$, respectively. The decay rates $\gamma_{d,2}$ and $\gamma_{d,3}$ take into account the loss of coherence due to elastic processes that cause the dephasing of state amplitudes. Absorption is compared for different coupling strengths Ω_c for a non-decaying state $|2\rangle$ in Fig. (5.3a). For $|\Omega_c| \ll \gamma_{31}$ a transparency window narrower than γ_{31} is seen (red line) in accord with EIT. However, for $|\Omega_c| > \gamma_{31}$ Autler-Townes splitting is observed (blue line) instead of EIT, even when $\gamma_{21} \approx 0$. This is because the resonances are shifted so far from each other that they don't overlap enough to allow significant interference of the pathways as understood in the dressed atom picture. The

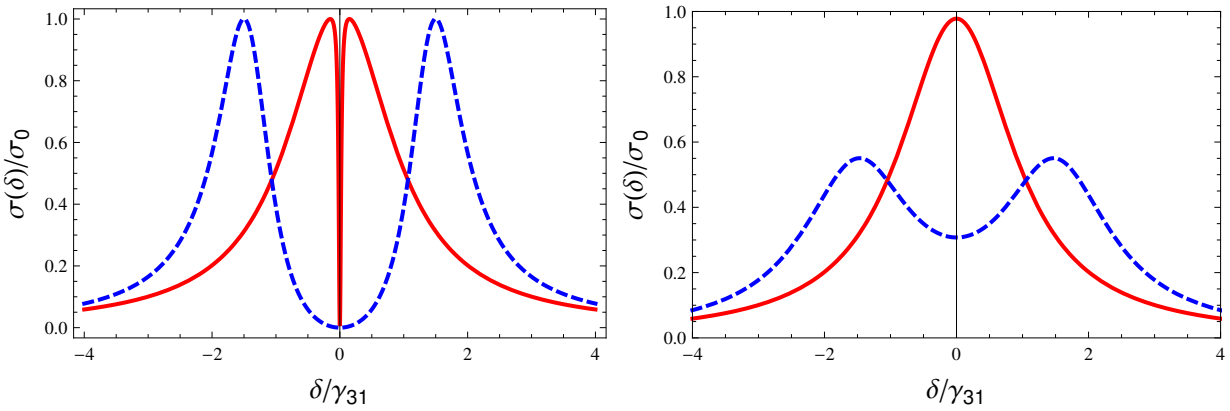

Figure 5.3.: The figures are in analogy to Fig. (7,10) in [80]. Absorption is plotted for two different coupling-laser strengths Ω_c, where in one case $\Omega_c < \gamma_{31}$ (red line) and in the other case $\Omega_c > \gamma_{31}$ (blue line) (a) In accord with the assumption that $|2\rangle$ is a metastable state, $\gamma_{21} = 10^{-4}\gamma_{31}$ and $\gamma_{31} = 1$. The coupling strengths $\Omega_c = 0.3\gamma_{31}$ (red line) and $\Omega_c = 3\gamma_{31}$ (blue line) are compared. (b) Absorption is plotted for a rapidly decaying state $|2\rangle$. We assume $\gamma_{31} = 1$ and $\gamma_{21} = \gamma_{31}$. The coupling strengths $\Omega_c = 0.3\gamma_{31}$ (red line) and $\Omega_c = 5\gamma_{31}$ (blue line) are compared.

same scenarios are compared for a state $|2\rangle$ that rapidly decays in Fig. (5.3b). As expected

EIT is not observed (red line) however Autler-Townes splitting (blue line) can still cause significant reduction of absorption if Ω_c is strong enough.

So far we have only dealt with absorption and the imaginary part of the linear susceptibility $\Im[\chi^{(1)}(\omega_p)]$, as dispersion is negligible at the atomic densities used in the model in chapter 6. However, laser dressing also influences the refractive properties of a medium [80] which are described by the real part of the linear susceptibility $\Re[\chi^{(1)}(\omega_p)]$. The refractive index for the probe field is defined as

$$n(\omega_p) = \sqrt{1 + \Re[\chi^{(1)}(\omega_p)]} \ .$$

The probe's group and phase velocity is given by

$$v_{gr} = \frac{c}{n + \omega_p(dn/d\omega_p)} \ ,$$

and

$$v_{ph} = \frac{c}{n} \ ,$$

respectively. It is characteristic of EIT that at resonance $\delta = 0$ the linear dispersion $dn/d\omega_p$ is positive leading to a reduction of the group velocity v_{gr}. Meanwhile, the index of refraction is unity for $\delta = 0$ and the phase velocity v_{ph} is equal to the speed of light c.

5.2. X-ray absorption by laser dressed neon

An *ab initio* theory for calculating the x-ray absorption cross section of optically laser-dressed atoms is presented in [44]. A single atom in the field of a moderately intense optical laser is considered. The laser intensity is assumed to be just low enough not to excite electrons in occupied orbitals in the atomic ground state. The optical laser's effect is to modify the final state into which inner-shell electrons can be excited by x-rays. The Hartree-Fock-Slater approximation is used to describe the many-electron atom. Both radiation fields are treated in terms of non-relativistic quantum-electrodynamics. This is the same as the semiclassical Floquet theory in the limit of high laser intensities. The laser with photon energy ω_L and the x-ray beam with photon energy ω_X are assumed to be monochromatic, linearly polarized and copropagating. The interaction of the atom with the optical laser is treated exactly, while the interaction of the atom with the x-ray field is described perturbatively. ω_X is assumed to be large enough to excite a K-shell electron and the x-ray intensity is assumed to be low enough to approximate its absorption as a one-photon process. However, this assumption may need to be modified for peak intensities achievable with x-ray FELs. The optical laser deforms the orbitals cylindrically along the laser's polarization axis, thereby introducing a dependance of the absorption cross section on the angle between the polarization vectors of the laser's and the x-ray's radiation field. The polarization axis of the laser and the x-ray probe are chosen to be parallel throughout this work. We will only discuss x-ray absorption for this setting.

The absorption cross section $\sigma_{1s}(\omega_X)$ of Ne near the K edge [43] is shown by the black line for no laser in Fig. (5.4a) and for a laser-dressing intensity of 10^{13} W/cm^2 in Fig. (5.4b). The calculations have been carried out in accord with the theory described

above [44] with the DREYD program from the FELLA package [89]. The laser is tuned to $\omega_L = 1.55$eV, which, within the decay width, is in resonance with the transition energy of the core-excited states $1s^{-1}3p$ and $1s^{-1}3s$. In the case of no laser-dressing the resonance

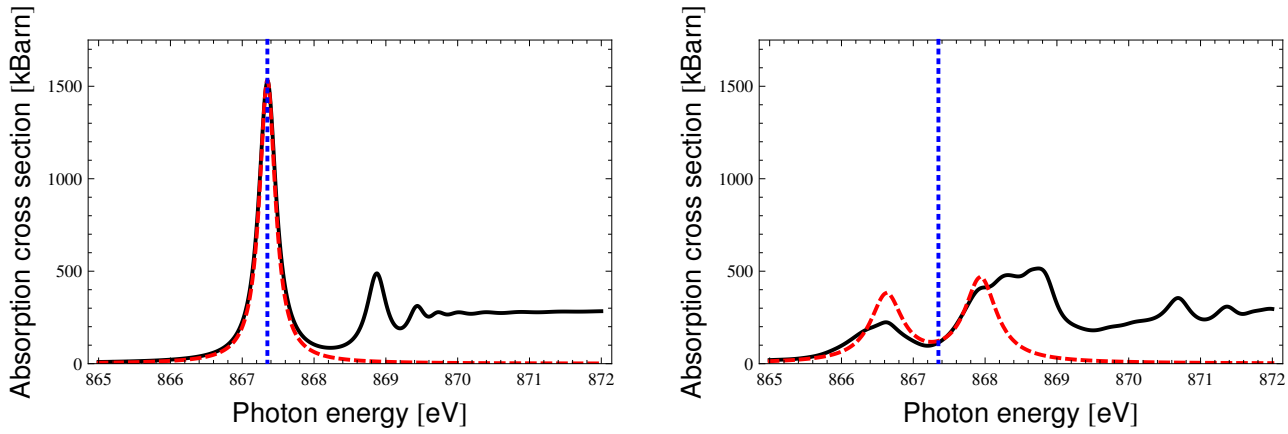

Figure 5.4.: The photoionization cross section $\sigma_{1s}(\omega_X)$ near the K edge (black line) is shown for the field free case (left) and for the case of laser dressing with an intensity of 10^{13} W/cm^2 (right). The photoionization cross sections $\sigma_{\text{model}}(\omega_X)$ calculated with a 3-level atom are displayed for both cases with the dashed red line. The blue dotted line marks the center of the $1s \rightarrow 3p$ Rydberg resonance at 867.4 eV. The figures are taken from reference [43].

at 867.4eV is caused by the $1s \rightarrow 1s^{-1}3p$ Rydberg excitation. The smaller peaks in the absorption cross section correspond to excitations $1s \rightarrow 1s^{-1}np$ into higher Rydberg states with $n \geq 4$. The optical laser causes mixing of the states and shifts the energy levels of the system [44] leading to a significant modulation of the absorption cross section $\sigma_{1s}(\omega_X)$ when the optical laser is turned on. The resonance at 867.4eV is strongly suppressed and two broader, less pronounced peaks appear at slightly higher and lower energies. The laser's effect is strongly reminiscent of Autler-Townes splitting, see Fig. (5.4b). In order to better understand the mechanism responsible for the laser-induced suppression of the $1s \rightarrow 1s^{-1}3p$ transition the Ne atom is reduced to a three-level model atom as investigated in Sec. (5.1). The states $|3\rangle$, $|2\rangle$ and $|1\rangle$, as in Fig. (5.2), are identified with the states $1s^{-1}3p$, $1s^{-1}3s$ and the Ne ground state, respectively. Now we have $\omega_c = \omega_L = 1.55$eV, $\omega_p = \omega_X$, $\omega_{23} = 1.69$eV and $\omega_{13} = 867.4$eV. The x-ray absorption cross section calculated for a model three-level atom with the *ab initio* theory introduced at the beginning of this section [43] is given by Eq. (5.5). The lifetime of the core-excited states $1s^{-1}3p$ and $1s^{-1}3s$ is dominated by the Auger lifetime [90] of a K-shell hole, which is 2.4 fs. Because the lifetimes are so short, other decoherence mechanisms such as elastic dephasing collisions are neglected [43] and we assume $\gamma_{d,2} = \gamma_{d,3} \approx 0$.

The absorption cross sections for the model three-level atom are plotted with the dashed, red lines in Fig. (5.4). For the case of laser-dressing (right) effective linewidths $\Gamma_2 = 0.54$ eV and $\Gamma_3 = 0.675$ eV are assumed [43] due to ionization induced broadening. The parameters of the model in atomic units are $\gamma_{31} = 0.012$, $\gamma_{21} = 0.01$ and $\Omega_c = \Omega_L = 0.048$, which in electron volts corresponds to a Rabi frequency of 1.3 eV. The relationship between the parameters, $\gamma_{31} \approx \gamma_{21} < \Omega_c$, used to calculate $\sigma_{1s}(\omega_X)$ and

$\sigma_{\text{model}}(\omega_X)$ corresponds to the scenario at hand in Fig. (5.3b) where Autler-Townes splitting causes a reduction in absorption and not EIT which calls for the coupling of two long-lived states to a short-lived upper state in a Λ shaped system [80]. When the laser is turned on, there are some deviations between the results of the *ab initio* theory and the model system, however, the general shape of the cross section is the same, in particular the suppression of absorption at the $1s \rightarrow 3p$ transition is reproduced. The agreement between the results in Fig. (5.4) suggests that the modulation of the cross section $\sigma_{1s}(\omega_X)$ around the transition frequency ω_{13} is related to Autler-Townes splitting, however, the situation is more complex.

The optical laser's intensity needs to be very high in order to induce transitions between the core-excited states on a timescale shorter than their Auger lifetime [43,91]. This leads to complications in comparison to the optical regime. The optical laser ionizes the coupled core-excited states in multiphoton processes [43] and leads to additional broadening of the resonances [91] in the laser-dressed absorption cross section. The core-excited states have very large linewidths caused by their rapid decay and optical-laser-induced ionization. Due to the optical laser's high intensity, the mixing of other core-excited Rydberg states $1s^{-1}nl$ outside the three-level subspace by multiphoton processes is unavoidable, even though the relative strength of mixing between states is determined by the optical laser's detuning [91]. The isolation of a three-level subspace within the Ne atom as done for Autler-Townes splitting in the optical regime is not possible [91].

Analysis of the *ab initio* results in reference [91] for the absorption cross section $\sigma_{1s}(\omega_X)$ reveals that the coupling of more than 10 spectral resonances contributes to the transparency window in Fig. (5.4b) and the coupling of over 40 spectral resonances contributes to the full spectrum of the absorption cross section $\sigma_{1s}(\omega_X)$, which explains the differences between the black and dashed, red lines in Fig. (5.4b). The effects of quantum interference on the transparency window in $\sigma_{1s}(\omega_X)$ are also calculated in [91] and found to be small. The absorption cross section $\sigma_{1s}(\omega_X)$ at the K edge is essentially the sum of non-interfering Lorentzians in support of the conclusion that the transparency is not related to EIT.

This mechanism can be used to exert control over the x-ray absorption of atoms. For a specific x-ray-probe energy ω_X the absorption cross section $\sigma_{1s}(\omega_X)$ depends on the optical laser's intensity. As described in Sec. (6.1) we use laser-dressing to control the lasing process in an XRL via modulation of the absorption cross section $\sigma_{1s}(\omega_X)$.

6. Inner-shell neon x-ray laser pumped by an x-ray FEL and controlled by optical light

The creation of population inversion in the x-ray regime by photoionization of inner-shell electrons was first theoretically investigated over four decades ago. The idea has been revisited several times since [18, 32–40]. Short rise times and high intensities for the pumping radiation are a prerequisite for the creation of significant population inversion [33, 34] as inner-shell decay processes occur on a femtosecond time scale [19]. The experimental realization of such XRLs was not possible until recently [41]. The advent of x-ray FELs, which satisfy the pumping conditions, has triggered new interest in photoionization-pumped XRLs [35–40].

I propose to extend an x-ray FEL pumped inner-shell Ne XRL scheme [37–39] by adding a copropagating optical laser to control the lasing process. The optical laser pulse dresses [42] the Ne atoms and modifies the Ne atoms' photoionization cross section [43,44] enabling the experimentalist to externally modulate the gain cross section and to imprint the optical laser pulse's properties onto the XRL.

6.1. Description of the lasing scheme

Population inversion is created in a Ne gas by longitudinal photoionization-pumping with an x-ray FEL [37–39]. Focusing the x-ray FEL onto the target creates an elongated column of core-ionized atoms by inner-shell photoionization. The core-ionized $1s^{-1}$ state of Ne^+ forms the upper level of the laser transition and the $1s2p^{-1}$ state of Ne^+ forms the lower level. The laser transition is of the form $2p \rightarrow 1s$ where an electron drops down from the $2p$-shell filling the $1s$-hole by either spontaneous or stimulated emission [52, 75]. Spontaneous emission [52, 75] is a radiative decay process in which an atom in an excited state undergoes a transition to a state with lower energy. In this process an electron drops down to fill a vacancy in an inner-shell. The atom emits a photon with energy equal to the difference of the electron's binding energy before and after the transition. Spontaneous emission is isotropic and the emitted photons have a random phase and polarization. Stimulated emission [52,75] is a process in which an excited atom interacts with an incident photon from external radiation field. The atom is "forced" to drop to a lower energy level and emits a photon in the process, which has the same energy, phase, polarization and propagates in the same direction as the incident photon. Radiative transitions of the form $2s \rightarrow 1s$ are strongly surpressed [52] and don't compete with the $2p \rightarrow 1s$ transition for gain. The XRL's output builds up from spontaneous emission meaning that the lasing medium is not used to amplify a laser resonant with the $1s - 2p$ transition. The XRL intensity is initially zero. At the beginning of the medium where the x-ray FEL pulse first creates a population inversion, radiation is only emitted through spontaneous emission.

It is this radiation that is amplified through stimulated emission in parts of the medium where population inversion exists. Spontaneous emission is isotropic, however, only the fraction of spontaneously emitted photons that are emitted in the forward direction and stay within the plasma column created by the x-ray FEL pump can be amplified, as shown in Fig. (6.1). This principal is called amplified spontaneous emission [1] and generates laser radiation the same way as conventional laser schemes save for the fact that the photons are not repeatedly bounced off mirrors in an optical resonator. The geometric acceptance angles $\Omega^{\pm}(z)$ give the fraction of spontaneously emitted photons by atoms at point P that fully traverse the remaining length of the plasma column, as seen in Fig. (6.1). Only these photons contribute to the build-up of laser radiation. $\Omega^{+}(z)$ can be calculated by finding the solid angle of a cone with apex 2Θ, which is the area of the cap on a unit sphere. In spherical coordinates this area S is given by

$$S = \int_0^{2\pi}\int_0^{\Theta} \sin\Theta' d\Theta' d\phi' \tag{6.1}$$

$$= 2\pi(1-\cos\Theta)\ . \tag{6.2}$$

One can see that $\cos\Theta = \frac{L-z}{\sqrt{r^2+(L-z)^2}}$, and we get the expression

$$\Omega^{+}(z) = 2\pi\Big(1 - \frac{L-z}{\sqrt{r^2+(L-z)^2}}\Big)\ , \tag{6.3}$$

for the geometric acceptance angles. $\Omega^{-}(z)$ can be calculated analogously and reads

$$\Omega^{-}(z) = 2\pi\Big(1 - \frac{L+z}{\sqrt{r^2+(L+z)^2}}\Big)\ . \tag{6.4}$$

The lower level of the lasing transition can be also directly populated through x-ray

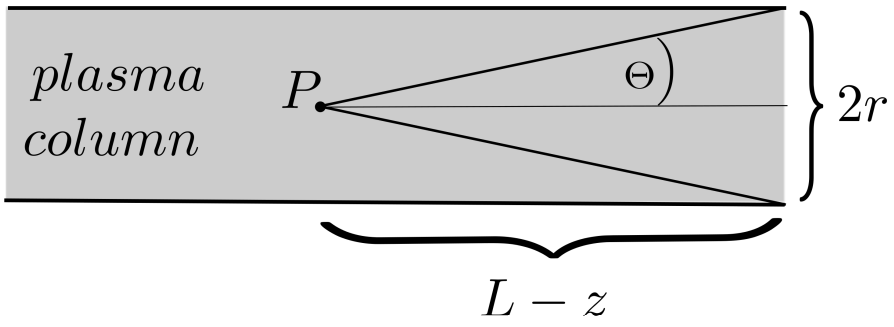

Figure 6.1.: Photons spontaneously emitted at point P in the plasma only contribute to the build-up of lasing if they stay completely within the plasma column for the remainder of their path meaning that they stay within the cone.

photoionization, if a $2p$-electron is removed from a neutral Ne atom. However, the x-ray photoionization cross section for loosely bound valence electrons is of orders of magnitude smaller than for tightly bound inner-shell electrons [19], as shown in Fig. (6.2). The rate at which the atoms are ionized is proportional to the absorption cross section [19], such

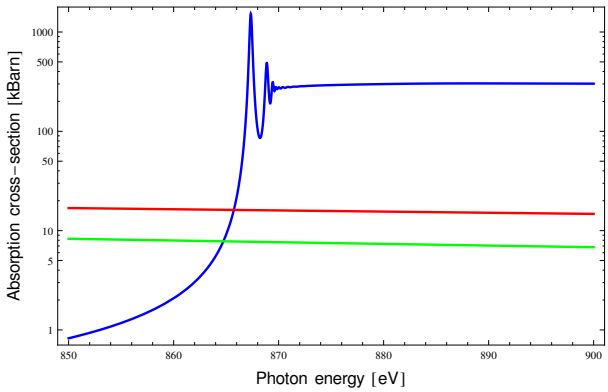

Figure 6.2.: X-ray photoionization cross sections for $1s$-,$2s$-,$2p$-electrons shown with blue,red and green, respectively. The peaks in the x-ray photoionization cross section σ_{N}^{1s} of a $1s$-electron in neutral Ne atoms are the $1s \rightarrow 3p, 4p, 5p, ...$-resonances found below the ionization threshold at 870.55 eV.

that the upper level of the laser is populated much more rapidly than the lower level by x-ray photoionization. Initially there are no ions in the gas, such that population inversion can be easily achieved in a single step process [32]. The $1s^{-1}$ state relaxes via Auger decay or radiative decay. The lifetime of the upper level is dominated by the Auger lifetime of a K-shell hole of 2.4 fs [90]. Its radiative lifetime of 116.77 fs is very long in comparison [90]. The rapid decay of the upper level permits only a transient population inversion of a few femtosecond duration. As the x-ray FEL pulse propagates through the gas it successively ionizes atoms briefly leaving the gas in a state of population inversion in its wake. Due to the ultra-fast decay of the upper lasing level, population inversion only exists in parts of the medium that the x-ray FEL pump pulse just passed. The population inversion propagates through the gas following the pump pulse; this does not involve movement of the atoms, as these are motionless on the time scale of femtoseconds. The XRL described above is investigated in references [37–39]. Fig. (6.3) shows the XRL intensity as a function of the distance propagated in the neon gas cell from reference [37] in black and the result of our reproduced calculations in red. The agreement between the curves is very good. Minor deviations result from the fact that randomly generated x-ray FEL pulses are used to pump the XRL and we do not know the exact pulse shape used for the calculations in [37].

The x-ray FEL pump pulse's central frequency ω_{XFEL} is tuned to the theoretical value of 868.2 eV below the ionization threshold of the $1s$-shell and off-resonantly to the $1s \rightarrow 3p$ Rydberg excitation, which has a transition frequency of 867.4 eV, as shown in Fig. (6.4b). This choice of pumping frequency facilitates that double core ionization which opens up other lasing channels [37] is avoided. Also, the choice of the x-ray FEL's energy makes it possible to control the lasing process with an optical laser pulse as will be explained momentarily. At this x-ray FEL photon energy, the atoms are excited to the $1s^{-1}3p$ Rydberg state of Ne, constituting the upper lasing level and the laser transition is of the form $1s^{-1}3p \rightarrow 1s2p^{-1}3p$, as shown in Fig. (1.3a). Compared to emission processes from the core-ionized $1s^{-1}$ state of Ne, the $3p$ Rydberg electron's presence shifts the XRL

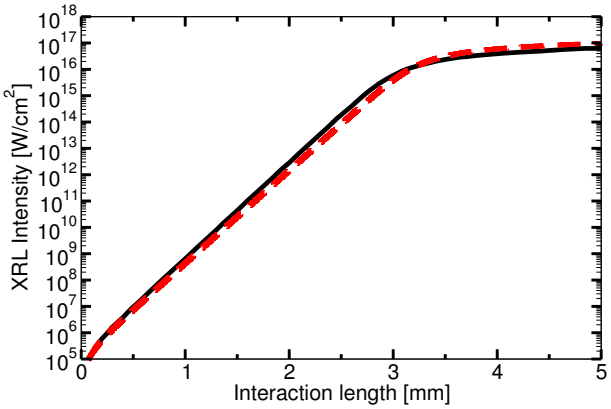

Figure 6.3.: The black line shows the XRL intensity as a function of the distance propagated in the neon gas cell from reference [37]. The dashed, red line show our reproduced result. The results minutely deviate because randomly generated x-ray FEL pulses are used to pump the XRL.

transition energy ω_{XRL} only by 0.07 eV from 849.81 eV to 849.74 eV. A difference that is small compared to the linewidth of the Rydberg excitation, so that we need not differentiate between emission processes from core-excited Ne atoms in the state $1s^{-1}3p$ and core-ionized Ne atoms with a vacancy in the $1s$-shell. Furthermore, we do not distinguish between the x-ray lasing process when the $3p$-electron is present and when it is ionized, because the Rydberg electron only minutely influences the occupied atomic orbitals and may be treated separately, as can be seen from the resonant Auger electron spectra of core-excited Ne [92, 93]. The excitation of the atoms with the x-ray FEL pulse can be treated independently from the $2p \rightarrow 1s$ lasing transition due to the strong decoherence effects discussed on page 24 in Sec. (4.2.1). The Rydberg state's lifetime is dominated by the Auger lifetime of a K-shell hole. The spontaneous emission rate from the $3p$-shell needs to be calculated in order to estimate its influence on the XRL. We obtain $A_{3p\rightarrow 1s} = \frac{4\omega_{\mathrm{ge}}^3 |\wp|^2}{3c^3} = 5.3 \times 10^{11}\ \mathrm{s}^{-1}$, with the transition energy $\omega_{\mathrm{ge}} = 867.4$ eV and the transition dipole matrix element $\wp = 0.0276$. $A_{3p\rightarrow 1s}$ is an order of magnitude smaller than the spontaneous emission rate from the $2p$-shell, $A_{2p\rightarrow 1s} = 5.9 \times 10^{12}\ \mathrm{s}^{-1}$, such that it does not interfere with the XRL transition.

By choosing an x-ray FEL central frequency ω_{XFEL} in the vicinity of the $1s \rightarrow 3p$ Rydberg excitation where $\sigma_{\mathrm{N}}^{1s}(\omega_{\mathrm{X}})$ exhibits a strong dependence on the x-ray frequency ω_{X}, we can use a copropagating optical laser pulse to control the XRL output. For instance an amplified Ti:sapphire laser system with up to 10^{13} W/cm^2 at a wavelength of 800 nm with a linear polarization parallel to the x-ray FEL's linear polarization axis. The optical laser resonantly couples the states $1s^{-1}3p$ and $1s^{-1}3s$ with each other and modulates $\sigma_{\mathrm{N}}^{1s}(\omega_{\mathrm{X}})$, the K-shell absorption cross section for the Ne ground state, depending on its intensity as described in Sec. (5.2). With a laser pulse of peak intensity 7×10^{12} W/cm^2, the absorption cross section $\sigma_{\mathrm{N}}^{1s}(\omega_{\mathrm{X}})$ can be increased more than eightfold from 86 kBarn to 720 kBarn at the frequency ω_{XFEL}, which is shown in Fig. (6.4b) by the green dotted line. The optical laser pulse cannot be chosen to be arbitrarily short. The x-ray absorption cross section for laser-dressed Ne is calculated with a Floquet theory approach [44], which assumes a continuous wave ansatz for the optical laser field. Throughout the calculations

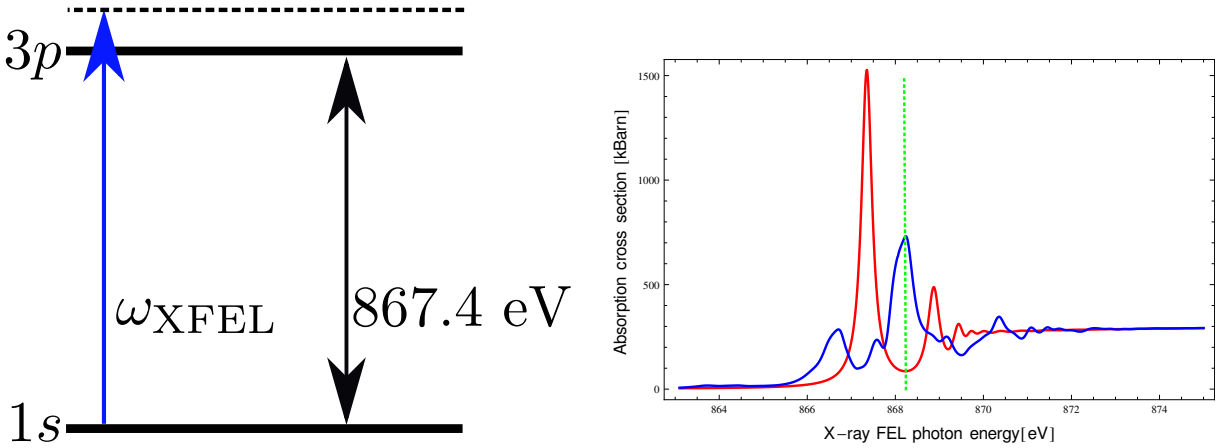

Figure 6.4.: a) Detuning of the x-ray FEL frequency $\omega_{\mathrm{XFEL}} = 868.2$ eV to the $1s \leftrightarrow 3p$ Rydberg excitation. b) Comparison of the σ_{N}^{1s} cross sections for the field-free (red) and the laser-dressed (blue) cases. The optical dressing laser has an intensity of 7×10^{12} W/cm^2.

optical laser pulses with FWHM duration of 5 cycles or 13 fs are used, which are long enough to be approximately treated as continuous waves. The x-ray FEL is tuned to $\omega_{\mathrm{XFEL}} = 868.2$ eV, because at this photon energy absorption of the x-ray FEL pulse is very small in the field-free case, as indicated by the absorption cross section at the dotted, green line in Fig. (6.4b). Since the rate at which the upper lasing level is populated is proportional to $\sigma_{\mathrm{N}}^{1s}(\omega_{\mathrm{X}})$, only a small population inversion can be created. By turning on the optical laser pulse, the rate at which the upper level is populated is significantly increased, resulting in a much bigger population inversion. It becomes possible to control the gain

$$g(z,t) = N_{\mathrm{U}}(z,t)\sigma_{\mathrm{stim}} - N_{\mathrm{L}}(z,t)\sigma_{\mathrm{abs}} \ , \tag{6.5}$$

of the lasing medium. Here $N_{\mathrm{U}}(z,t)$ and $N_{\mathrm{L}}(z,t)$, are the occupancies of the upper and lower levels, respectively. The cross sections for spontaneous emission σ_{stim} and absorption σ_{abs} are evaluated at the peak of the line, supposing a Lorentzian line shape, as given in Sec. (4.2.4). As we will extensibly discuss in Sec. (6.2.1) this mechanism increases the XRL's output intensity by several orders of magnitude and makes it possible to control the x-ray lasing process with the optical laser.

Due to the modulation of the x-ray absorption by the optical laser pulse, the absorption cross section σ_{N}^{1s} is dependent on the momentary intensity of the optical laser $I_{\mathrm{L}}(z,t)$ at any point in time and space. The x-ray absorption cross section becomes

$$\sigma_{\mathrm{N}}^{1s} = \sigma_{\mathrm{N}}^{1s}(I_{\mathrm{L}}, \omega_{\mathrm{X}}) = \sigma_{\mathrm{N}}^{1s}(z,t,\omega_{\mathrm{X}}) \ .$$

The optical laser pulse's intensity $I_{\mathrm{L}}(z,t)$ has a Gaussian temporal profile and is given by,

$$I_{\mathrm{L}}(z,t) \ = \ I_{\mathrm{L}_0} \exp[-((z-ct)a)^2/(2\tilde{t}_{\mathrm{L}}^2)] \ , \tag{6.6}$$

where I_{L_0} is the peak pulse intensity, c is the speed of light, $\tilde{t}_{\mathrm{L}}$ is the FWHM of the laser pulse and $a = 2\sqrt{-2ln(1/2)}$ is a constant. The total absorption cross section

$\sigma_{\mathrm{N}}^{\mathrm{Tot}}(I_{\mathrm{L}},\omega_{\mathrm{X}})$ is just the sum of $\sigma_{\mathrm{N}}^{1s}(I_{\mathrm{L}},\omega_{\mathrm{X}})$ and the ionization cross sections σ_{N}^{2s} and σ_{N}^{2p} for the valence electrons, which are approximately constant because ω_{XFEL} is far above threshold. The optical laser pulse does not contribute to the ionization of the $2p$ and $2s$ electrons as its photon energy is an order of magnitude smaller than the binding energies. Although the dressing laser's photon energy $\omega_{\mathrm{L}} = 1.55\mathrm{eV}$ is also smaller than the Rydberg electron's binding energy $E_{\mathrm{b}}^{3p} = 3.11\mathrm{eV}$ [94], it is strongly ionized via two-photon processes due the laser's high intensity, however as it has been explained, the 3p electron need not be considered. For this reason, spontaneous radiative transitions of the form $1s^{-1}2p^{-1}3s \rightarrow 1s^{-1}2p3s^{-1}$ need not be considered after an XRL photon has been emitted because the $1s^{-1}3p$ state is hardly populated.

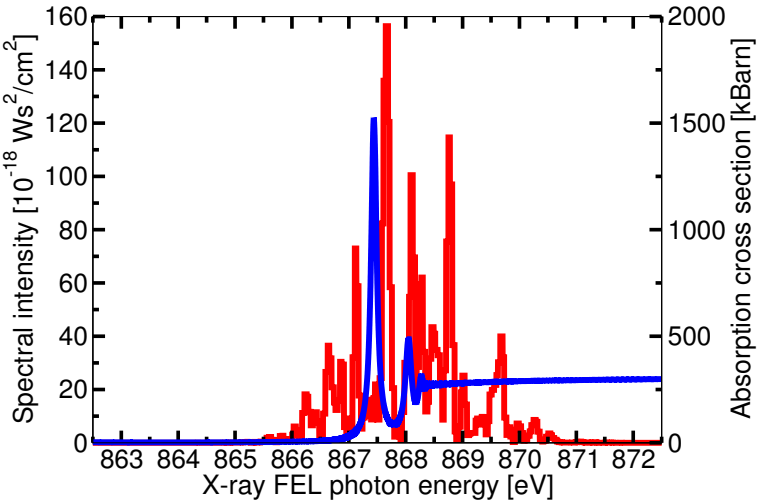

Figure 6.5.: Total photoionization cross section $\sigma_{\mathrm{N}}^{\mathrm{Tot}}(\omega_{\mathrm{XFEL}})$ for neutral Ne without laser dressing (blue) and the spectral intensity $S_{\mathrm{P}}(\omega_{\mathrm{X}})$ of a random x-ray FEL pulse (red) with $\omega_{\mathrm{XFEL}} = 868.2$ eV and $\Delta\omega_{\mathrm{XFEL}} = 2.6$ eV .

The x-ray FEL pulse is non-monochromatic with spectral FWHM $\Delta\omega_{\mathrm{XFEL}}$. It must be taken into account that each frequency component present in the pump pulse excites the Ne gas with varying strength and populates the upper level of the lasing transition at a different rate. Assuming that the spectrum is the same at every point of the pulse, we calculate the weighted average cross section to describe the excitation. The evolution of the neutral state's occupancy in the model becomes

$$\frac{dN_{\mathrm{N}}(z,t)}{dt} = \frac{I_{\mathrm{P}}(z,t)}{\omega_{\mathrm{P}}} N_{\mathrm{N}}(z,t) \frac{\int_0^\infty \sigma_{\mathrm{N}}^{\mathrm{Tot}}(I_{\mathrm{L}},\omega_{\mathrm{x}}) \frac{S_{\mathrm{P}}(z,\omega_{\mathrm{x}})}{\omega_{\mathrm{x}}} d\omega_{\mathrm{x}}}{\int_0^\infty \frac{S_{\mathrm{P}}(z,\omega_{\mathrm{x}})}{\omega_{\mathrm{x}}} d\omega_{\mathrm{x}}} . \tag{6.7}$$

The integral in the denominator can be interpreted as the weighted average absorption cross section given by the convolution of the spectral intensity $S_{\mathrm{P}}(z,\omega_{\mathrm{x}})$ and the line function $\sigma_{\mathrm{N}}^{\mathrm{Tot}}(I_{\mathrm{L}},\omega_{\mathrm{x}})$. The spectral intensity is defined as $S_{\mathrm{P}}(z,\omega_{\mathrm{x}}) = \frac{c}{4\pi^2}|E(z,\omega_{\mathrm{x}})|^2$ [73]. The overlap of these functions is shown for a randomly generated x-ray FEL pulse and $\sigma_{\mathrm{N}}^{\mathrm{Tot}}(I_{\mathrm{L}}=0,\omega_{\mathrm{x}})$ in Fig. (6.5).

The dimensions of the XRL are determined by the focus of the x-ray FEL pulse. The x-ray FEL beam can be focused to a minimal spot size with radius $r = 1\mu\mathrm{m}$ [26] at

the beam waist. Assuming a Gaussian beam profile, the focal depth, which is twice the Rayleigh range [1], is given by $L = \frac{2\pi r^2}{\lambda_{\mathrm{XFEL}}}$. The focal depth is equal to the segment of the beam around the beam waist, where the beam's radius is less than $r\sqrt{2}$. With the minimum spot radius $r = 1\mu$m and the wavelength $\lambda_{\mathrm{XFEL}} = 1.40$nm, which corresponds to a photon energy ω_{XFEL}, the focal depth equates to $L = 4.4$mm. Thus, the length of Ne gas chamber is chosen to be 4.4 mm and its center coincides with the x-ray FEL's beam waist. The transverse coherence length of the XRL is determined by its geometry [95] and can be calculated with $L_T = \frac{\lambda L}{2\pi r}$. For given parameters we find $L_T \approx 1\mu$m, meaning that the XRL has full transverse coherence.

6.1.1. X-ray laser rate equations

The rate equations describing laser scheme can be deduced from chapter 4 by properly appropriating the prevalent physical processes of the system to the quantities in (6.7)

Eqs. (4.62–4.64). This is possibe because the laser rate equation have been derived for unspecified, general pump rates and decay rates. The only constraint is that they satisfy the scheme illustrated in Fig. (4.2). The populations of the excited state ρ_{ee} and the ground state ρ_{gg} of the two-level system in Sec. (4.2) can be connected to the single-atom occupancies N_{U} and N_{L} of the upper and lower levels in a straightforward manner because the atoms are independent from each other and homogeneously distributed in the entire gas [1].

The occupancy of the upper level $N_{\mathrm{U}}(z,t)$ of the laser is connected to the population by $N_{\mathrm{U}}(z,t) = \frac{\rho_{\mathrm{ee}}(z,t)}{n_{\mathrm{A}}}$, which can be calculated with Eq. (4.62). Expressions for the upper level pumping rate λ_{e} and upper level decay rate γ_{e} need to be found. In our lasing scheme the upper level occupancy is built up via excitation of a K-shell electron in a neutral Ne atom, such that

$$\lambda_{\mathrm{e}} \;=\; \frac{I_{\mathrm{P}}(z,t)}{\omega_{\mathrm{XFEL}}} N_{\mathrm{N}}(z,t) \frac{\int_0^\infty \sigma_{\mathrm{N}}^{1s}(I_{\mathrm{L}},\omega_{\mathrm{X}}) \frac{S_{\mathrm{P}}(z,\omega_{\mathrm{X}})}{\omega_{\mathrm{X}}} d\omega_{\mathrm{X}}}{\int_0^\infty \frac{S_{\mathrm{P}}(z,\omega_{\mathrm{X}})}{\omega_{\mathrm{X}}} d\omega_{\mathrm{X}}} \,. \tag{6.9}$$

Here, we have accounted for the fact that the x-ray FEL pump pulse has a finite spectral distribution in the same way as in Eq. (6.7) by using an average absorption cross section. Besides stimulated emission, the processes that destroy the upper lasing state are Auger decay and valence ionization of the core-excited Ne atom, such that we have

$$\gamma_{\mathrm{e}} \;=\; \Gamma_{\mathrm{Tot}} + \sigma_{\mathrm{U}}^{\mathrm{Tot}} \frac{I_{\mathrm{P}}(z,t)}{\omega_{\mathrm{XFEL}}} \,, \tag{6.10}$$

where Γ_{Tot} is the total Auger decay rate and $\sigma_{\mathrm{U}}^{\mathrm{Tot}} \frac{I_{\mathrm{P}}(z,t)}{\omega_{\mathrm{XFEL}}}$ is the rate at which ionization destroys the upper level. $\sigma_{\mathrm{U}}^{\mathrm{Tot}}$ is the total photoionization cross section of a core ionized Ne ion. Since double core photoionization is not possible, only ionization of the valence electrons needs to be considered. $\sigma_{\mathrm{U}}^{\mathrm{Tot}}$ is approximately constant because ω_{XFEL} is far

above threshold. Inserting these expressions into Eq. (4.62) we obtain

$$\begin{aligned}\frac{dN_{\mathrm{U}}(z,t)}{dt} &= \frac{I_{\mathrm{P}}(z,t)}{\omega_{\mathrm{XFEL}}}N_{\mathrm{N}}(z,t)\frac{\int_0^\infty \sigma_{\mathrm{N}}^{1s}(I_{\mathrm{L}},\omega_{\mathrm{X}})\frac{S_{\mathrm{P}}(z,\omega_{\mathrm{X}})}{\omega_{\mathrm{X}}}d\omega_{\mathrm{X}}}{\int_0^\infty \frac{S_{\mathrm{P}}(z,\omega_{\mathrm{X}})}{\omega_{\mathrm{X}}}d\omega_{\mathrm{X}}} \\ &-\frac{\sigma_{\mathrm{se}}}{\omega_{\mathrm{XRL}}}\{I_{\mathrm{XRL}}^{+}(z,t)+I_{\mathrm{XRL}}^{-}(z,t)\}N_{\mathrm{U}}(z,t) \\ &+\frac{\sigma_{\mathrm{abs}}}{\omega_{\mathrm{XRL}}}\{I_{\mathrm{XRL}}^{+}(z,t)+I_{\mathrm{XRL}}^{-}(z,t)\}N_{\mathrm{L}}(z,t) \\ &-\{\Gamma_{\mathrm{Tot}}+A_{2p\to 1s}+\sigma_{\mathrm{U}}^{\mathrm{Tot}}\frac{I_{\mathrm{P}}(z,t)}{\omega_{\mathrm{XFEL}}}\}N_{\mathrm{U}}(z,t)\ .\end{aligned} \tag{6.11}$$

The first line on the right-hand side gives rate at which the upper level is populated through photoionization pumping. The second and third lines on the right-hand side model the effects of stimulated emission and absorption on the occupancy of the upper state. $I_{XRL}^{+(-)}(z,t)$ is the intensity of the XRL pulse propagating in the positive (negative) z-direction and ω_{XRL} the XRL radiation's frequency. The last line on the right-hand side contains the processes that depopulate the upper level. $A_{2p\to 1s}$ is the rate of spontaneous emission from the $2p$-shell to the $1s$-shell.

Rabi Flopping [42, 75] of the core electron between the $3p$-shell and $1s$-shell induced by the x-ray FEL pulse can effect the populations of the upper and lower state. However, the x-ray FEL induced transition from the core-excited $1s^{-1}3p$ state back to the ground state is negligible as long as the Auger decay of the core-excited state is faster than the induced stimulated emission process [63]. For Rabi oscillations to take place on the same time scale as the Auger decay a minimal x-ray FEL intensity of $I_{\mathrm{R,min}} = 1.5\times 10^{18}$ W/cm^2 is required [63]. The reason why such a high intensity is required is because the Auger decay happens ultrafast, within a few femtoseconds and becasue the transition dipole matrix elements for inner-shell transitions are quite small [63]. We keep the x-ray FEL pump intensity beneath this value for all calculations.

The differential equation for the lower level occupancy $N_{\mathrm{L}}(z,t)$ can be obtained analogously by finding expressions for the lower level pumping rate λg and lower level decay rate γ_{g} in Eq. (4.62). Beside spontaneous and stimulated emission from the upper level, the lower level is created when the x-ray FEL pump pulse ionizes a $2p$-electron from a neutral Ne atom. Thus the lower level pumping rate is

$$\lambda\mathrm{g} = \sigma_{\mathrm{N}}^{2p}\frac{I_{\mathrm{P}}(z,t)}{\omega_{\mathrm{XFEL}}}N_{\mathrm{N}}(z,t)\ , \tag{6.12}$$

where σ_{N}^{2p} is the ionization cross section of a $2p$ electron in a neutral Ne atom. The lower level is composed of Ne ions with a hole in the outer $2p$-shell, thus the only way it can be destroyed is through further ionization by the x-ray FEL pulse. It follows that the rate at which the lower level is destroyed is given by

$$\gamma_{\mathrm{g}} = \sigma_{\mathrm{L}}^{\mathrm{Tot}}\frac{I_{\mathrm{P}}(z,t)}{\omega_{\mathrm{XFEL}}}\ , \tag{6.13}$$

where $\sigma_{\mathrm{L}}^{\mathrm{Tot}}$ is the total absorption cross section of valence-ionized Ne and only takes into account the ionization of the $2s-$ and $2p$-electrons as the x-ray FEL photon energy of

ω_{XFEL} is too low to ionize a $1s$-electron, which is bound stronger than in a neutral Ne atom. Combining these expressions we obtain

$$\begin{aligned}\frac{dN_{\mathrm{L}}(z,t)}{dt} &= A_{2p\to 1s}N_{\mathrm{U}}(z,t)+\sigma_{\mathrm{N}}^{2p}\frac{I_{\mathrm{P}}(z,t)}{\omega_{\mathrm{XFEL}}}N_{\mathrm{N}}(z,t) \\ &+\frac{\sigma_{\mathrm{se}}}{\omega_{\mathrm{XRL}}}\{I_{\mathrm{XRL}}^{+}(z,t)+I_{\mathrm{XRL}}^{-}(z,t)\}N_{\mathrm{U}}(z,t) \\ &-\frac{\sigma_{\mathrm{abs}}}{\omega_{\mathrm{XRL}}}\{I_{\mathrm{XRL}}^{+}(z,t)+I_{\mathrm{XRL}}^{-}(z,t)\}N_{\mathrm{L}}(z,t) \\ &-\sigma_{\mathrm{L}}^{\mathrm{Tot}}\frac{I_{\mathrm{P}}(z,t)}{\omega_{\mathrm{XFEL}}}N_{\mathrm{L}}(z,t)\ .\end{aligned} \tag{6.14}$$

The second and third lines on the right-hand side describe the interaction of the XRL radiation with the medium and the effects of stimulated emission and absorption on the lower level occupancy. The spontaneous emission rate $A_{2p\to 1s}$ directly transfers population from the upper to the lower level.

The rate equation describing the change of intensity of the XRL pulse whilst propagation is obtained from Eq. (4.64) by replacing $\rho_{\mathrm{ee}}(z,t)$ and $\rho_{\mathrm{gg}}(z,t)$ with $N_{\mathrm{U}}(z,t)$ and $N_{\mathrm{L}}(z,t)$, respectively. Furthermore, we need to account for spontaneous emission from the upper lasing level, as it is this radiation that is amplified in the lasing medium. Thus we add the term

$$\frac{\Omega^{\pm}(\tilde{z})}{4\pi}A_{2p\to 1s}N_{\mathrm{U}}(\tilde{z},t)n_{\mathrm{A}}c\ , \tag{6.15}$$

to the right-hand side of Eq. (4.64). This expression gives the number of spontaneously emitted photons per second at a point $\tilde{z}$ that contribute to lasing in the positive z-direction for $\Omega^{+}(z)$ and in the negative z-direction for $\Omega^{-}(z)$. The rate-equation for the XRL intensity is given by

$$\begin{aligned}\frac{dI_{\mathrm{XRL}}^{\pm}(z,t)}{dt} &= I_{\mathrm{XRL}}^{\pm}(z,t)cn_{\mathrm{A}}\{\sigma_{\mathrm{se}}N_{\mathrm{U}}(z,t)-\sigma_{\mathrm{abs}}N_{\mathrm{L}}(z,t)\} \\ &+\frac{\Omega^{\pm}(z)}{4\pi}A_{2p\to 1s}N_{\mathrm{U}}(z,t)n_{\mathrm{A}}c\mp c\frac{dI_{\mathrm{XRL}}^{\pm}}{dz}\ ,\end{aligned} \tag{6.16}$$

where $I_{\mathrm{XRL}}^{+}(z,t)$ is the intensity of the pulse traveling in the positive z-direction along with the x-ray FEL pump pulse $I_{\mathrm{P}}(z,t)$ and the optical laser pulse $I_{\mathrm{L}}(z,t)$, and $I_{\mathrm{XRL}}^{-}(z,t)$ is the intensity of the XRL pulse traveling in the negative z-direction. The first line on the right-hand side of Eq. (6.16) describes the amplification of the XRL pulse due to stimulated emission and its attenuation due to absorption. We neglect $I_{\mathrm{XRL}}^{-}(z,t)$ in our calculations as it propagates in the opposite direction of the population inversion and lasing cannot occur [39].

A collection of all constants can be found in Tab. (6.1), except for $\sigma_N^{1s}(\omega_P)$, which is displayed in Fig. (6.4b).

6.1.2. XRL linewidth

The width of the lasing transition $\Delta\omega_{\mathrm{XRL}}$ is dominated by the lifetime of the upper level, which is the lifetime of the Rydberg excitation. The width of the upper state is

Table 6.1.: Parameters of the XRL

Physical quantity	SI-units	Atomic units [a.u.]
X-ray FEL central frequency ω_{P}	868.24 eV	31.91
Stimulated emission cross section σ_{se}	53.68 MBarn	1.917
Absorption cross section σ_{abs}	8.946 MBarn	0.3195
XRL frequency ω_{XRL}	850 eV	31.24
XRL linewidth $\Delta\omega_{\mathrm{XRL}}$	0.252 eV	9.261×10^{-3}
Laser frequency ω_{L}	1.55 eV	$5.696{\times}10^{-2}$
Auger decay rate upper level Γ_{Tot}	$3.77 \times 10^{14}\mathrm{s}^{-1}$	9.117×10^{-3}
Absorption cross section of core-ionized Ne $\sigma_{\mathrm{U}}^{\mathrm{Tot}}$	32.79 kBarn	1.171×10^{-3}
Spontaneous emission rate $A_{2p\to 1s}$	$5.94{\times}10^{12}$ s^{-1}	1.436×10^{-4}
σ_{N}^{2p}	7.70 kBarn	2.749×10^{-4}
Absorption cross section of valence-ionized Ne $\sigma_{\mathrm{L}}^{\mathrm{Tot}}$	24.22 kBarn	8.649×10^{-4}
Focal radius r	1 μm	18897
Atomic number density n_{A}	10^{19} cm^{-3}	1.482×10^{-6}
Interaction length L	4.4 mm	8.315×10^{7}

$\Delta\omega_{\mathrm{U}} = 0.252$eV [96]. The fine structure of the $1s \leftrightarrow 2p$ transition is smaller than the natural line width and can be neglected [33].

Line broadening due to thermal ion motion is expected to be minimal. The ion temperature in the plasma column is expected to remain cold during the time of amplification due to the femtosecond timescale on which population inversion is built up. The Doppler width can be estimated [97] with

$$\Delta\omega_{\mathrm{d}} = \frac{0.15}{\lambda}\left(\frac{T_{\mathrm{i}}}{A_{\mathrm{i}}}\right)^{1/2}\mathrm{eV}\ ,$$

where λ is the transition wavelength in angstroms, T_{i} is the ion temperature in eV, and A_{i} is the ion mass in atomic mass units. For the $2p \to 1s$-transition in Ne at a room temperature of 300K we have $\lambda = 14.3$ Å, $T_{\mathrm{i}} = 0.026$ eV and $A_{\mathrm{i}} = 20$ u, which results in $\Delta\omega_{\mathrm{d}} = 3.8 \times 10^{-4}$ eV. $\Delta\omega_{\mathrm{d}}$ is negligible compared to the natural linewidth.

In a plasma, stark broadening is caused by the electric field generated by the ions. Only quadratic stark broadening needs to be considered. The linear Stark effect does not play a role [34] because the energy difference between the $2p$- and $2s$-levels of 29.64eV is much greater than the natural linewidth, so that the levels cannot be considered degenerate. The linewidth due to Stark broadening can be estimated [97] with

$$\Delta\omega_{\mathrm{s}} = 2 \times 10^{-32}\left(\frac{n_{\mathrm{U}}^6}{S_{\mathrm{e}}^4}\right) Z_{\mathrm{i}}^2\left(1 - \frac{N_{\mathrm{e}_0}}{S_{\mathrm{e}}}\right) n_{\mathrm{i}}^{4/3}\mathrm{eV}\ ,$$

where n_{U} is the principle quantum number of the upper state of the XRL transition, S_{e} is the shielding factor, Z_{i} and N_{i} are the ion charge and density, and N_{e_0} is the number of outer shell shielding electrons. For $n_{\mathrm{U}} = 2$, $Z_{\mathrm{i}} = 2$, $S_{\mathrm{e}} = 7.48$ [52] and $n_{\mathrm{i}} = n_{\mathrm{A}} = 10^{19}$ cm^{-3}, we get $\Delta\omega_{\mathrm{s}} = 2.65 \times 10^{-8}$ eV, which is also negligible.

Electron impact broadening can be estimated with [97]

$$\Delta\omega_{\mathrm{ei}} = 1.4 \times 10^{-23} \left(\frac{n_{\mathrm{e}} n_{\mathrm{U}}^4}{T_{\mathrm{e}}^{1/2} S_{\mathrm{e}}^2} \right) \left(1 - \frac{N_{\mathrm{e0}}}{S_{\mathrm{e}}} \right)^2 \mathrm{eV} \ .$$

Taking $T_{\mathrm{e}} = 846.7$ eV, the same as for estimating τ_{coll}, we get $\Delta\omega_{\mathrm{ei}} = 10^{-6}$ eV, which can be neglected compared to the natural linewidth $\Delta\omega_{\mathrm{nat}}$.

The gain of the XRL depends on the linewidth of the lasing transition as the stimulated emission cross section given in Eq. (4.67) scales with the inverse of $\Delta\omega_{\mathrm{XRL}}$. The fact that besides lifetime broadening no effects contribute to the XRL's linewidth results in a narrow high-gain lasing transition.

6.1.3. Dispersion

As a consequence of dispersion [54] the phase and group velocities of the laser and x-ray FEL pulses in a medium differ from those in vacuum, causing deformation of the pulses and a change the relative position of the pulses to each other. Dispersion needs to be estimated in a Ne gas as well as in a plasma. The group velocity in the gas is given by

$$v_{\mathrm{g}}(\omega) = \frac{c}{1 + 2\pi n_{\mathrm{A}} \{ \alpha_{\mathrm{I}}(\omega) + \omega \times (d\alpha_{\mathrm{I}}/d\omega)(\omega) \}} \ ,$$

where α_{I} is the the dynamic polarizability of Ne and n_{i} is the ion density. The group velocity in a plasma is given by

$$v_{\mathrm{g,pl}}(\omega) = c \sqrt{1 - \frac{\omega_{\mathrm{P}}^2}{\omega^2}}$$

with the plasma frequency $\omega_{\mathrm{P}} = \sqrt{4\pi n_{\mathrm{e}}}$ and n_{e} is the electron density. The phase velocities in any medium can be all calculated with

$$v_{\mathrm{p}}(\omega) = \frac{c}{n(\omega)} \ ,$$

where $n(\omega)$ is the real part of the appropriate refractive index. We assume a worst case scenario for the estimates in which all ions are doubly charged due to multiphoton ionization and auger decay giving $n_{\mathrm{e}} = 2n_{\mathrm{A}}$. The atom density is $n_{\mathrm{A}} = 10^{19}$ cm^{-3} . For the laser pulse we find $\alpha_{\mathrm{I}}(\omega_{\mathrm{L}}) = 2.685$ a.u., $d\alpha_{\mathrm{I}}/d\omega(\omega_{\mathrm{L}}) = 0.2312$ a.u. and $n(\omega_{\mathrm{L}}) - 1 = 3 \times 10^{-5}$ through linear interpolation [98]. For the x-ray FEL pulse the dynamic polarizability of laser dressed Ne is required [99], which can be calculated with the DREYD program v1.3.0. The resulting changes in the phase and group velocities for a laser dressing intensity of 10^{13} W/cm^2 can be found in Tab. (6.2). Dispersive effects are negligible for both the x-ray FEL pulse and the optical laser pulse in the medium.

6.1.4. Collisional ionization

The free electrons created by the Auger process can have a profound impact on the populations through collisional ionisation. The most rapid collisional process is the collisional

Table 6.2.: Estimates of the changes of the phase and group velocities for the laser and x-ray FEL pulses. A laser dressing intensity of 10^{13} W/cm^2 is assumed. The group velocity v_g for the x-ray FEL pulse in the gas was calculated for a number density $n_A = 2.4 \times 10^{19}$ cm^{-3} in [43] and serves as an upper bound becasue dispersion is weaker in a gas of lower density.

ω [eV]	$v_p/c - 1$	$v_g/c - 1$	$v_{p,pl}/c - 1$	$v_{g,pl}/c - 1$
1.55	-3×10^{-5}	-2.5×10^{-5}	3.3×10^{-4}	-3.3×10^{-4}
868.24	1.8×10^{-8}	$< 3 \times 10^{-6}$	5.8×10^{-7}	-5.8×10^{-7}

ionization of outer-shell electrons [34]. The ion-electron collision time can be estimated by a geometrical collisional ionization cross section [34], which gives the following expression for the time to increase the average ionization stage by one:

$$\tau_{coll} \sim \frac{1}{n_e \pi a_0^2 (8T_e/\pi)^{\frac{1}{2}}} .$$

An Auger electron emitted from the $3p$-subshell following a $2p \rightarrow 1s$-transition has Temperature of $E_e = 846.7$ eV, which is the highest value any Auger electron can have. Supposing a gas number density $n_A = 10^{19}$ cm^{-3}, an electron density $n_e = n_A$, and that all electrons have the maximum possible Temperature T_e, the electron-ion collison time will be around $\tau_{coll} \sim 582$ fs. The build-up of the population inversion happens on the timescale of several femtoseconds [37], short compared to τ_{coll}. For this reason, collisional relaxation effects on the populations can be neglected. The collision times for the ionized $3p$ electrons need not be calculated as they are much longer than for the Auger electrons due to their smaller temperature.

6.1.5. Absorption of the x-ray FEL pulse

To describe the absorption of the x-ray FEL pump pulse we need to consider the absorption of the different frequency components of the pulse for which the strength of absorption varies as can be seen in Fig. (6.5). In general absorption of a broadband pulse can be described in the following way. The electric field in the frequency domain as a function of the propagated distance [73] is given by

$$\widetilde{E}_P(z, \omega_X) = \widetilde{E}_P(0, \omega_X) e^{i \frac{\omega_X}{c} n(\omega_X) z} , \tag{6.17}$$

where $n(\omega_X)$ is the index of refraction [73]. We will show in Sec. (6.1.3) that dispersion is negligible, such that $n(\omega_X)$ is a purely imaginary number. Its imaginary part is $\Im[n(\omega_X)] = \frac{c n_D \sigma(\omega_X)}{\omega_X}$ [99] with the atomic number density n_D and the absorption cross section $\sigma(\omega_X)$ describes the absorption of the pulse. With Eq. (3.5) we can write the pump intensity as

$$\begin{aligned} I(z,t) &= \frac{1}{2\pi\alpha} \left| \frac{1}{2\pi} \int_{-\infty}^{\infty} \widetilde{E}_P(z, \omega_X) e^{-i\omega_X t} d\omega_X \right|^2 \\ &= \frac{1}{2\pi\alpha} \left| \frac{1}{2\pi} \int_{-\infty}^{\infty} \widetilde{E}_P(0, \omega_X) e^{-n_D \sigma(\omega_X) z} e^{-i\omega_X t} d\omega_X \right|^2 \end{aligned} \tag{6.18}$$

In our calculations we used an approximated equation for calculating the x-ray FEL pump pulse's absorption in the medium. The details are explained in Sec. (6.7).

6.2. Analysis of the XRL's output

The output of the XRL strongly depends on the pump pulses. To illustrate the relationship between the intensity, spectral intensity and duration of the x-ray FEL and the gain and intensity of the XRL, we will discuss calculation done with Gaussian pump pulses. We chose not to use SASE pulses because of their chaotic nature, which makes the analysis of the dependencies more difficult. Naturally, all findings are applicable to pumping with SASE pulses, as we demonstrate in Sec. (6.3). Gaussian-shaped x-ray FEL pulses cannot yet be achieved at existing x-ray FEL facilities, however, self-seeded x-ray FELs will be able to produce such pulses in the future. For the calculations we use

$$I_{\mathrm{P}}(z,t) \;=\; I_{\mathrm{P}_0}\exp[-((z-ct)a)^2/(2\tilde{t}_{\mathrm{P}}^2)]\;, \tag{6.19}$$

for the x-ray FEL pulse intensity, where $a = 2\sqrt{-2\ln(1/2)}$ is a constant, $\tilde{t}_{\mathrm{P}}$ is the FWHM duration of the pulse and

$$I_{\mathrm{P}_0} \;=\; \frac{\Phi}{(\frac{1}{2}\tilde{t}_{\mathrm{P}}\sqrt{\pi/\ln 2})}\;, \tag{6.20}$$

is defined such that the integral $\int_0^\infty I_{\mathrm{P}}(z,t)dt = \Phi$ for any z, where Φ is the radiative fluence. The fluence Φ is the amount of energy flowing through a unit area per unit of time and can be calculated for an x-ray FEL pulse with $\Phi = \frac{N_{\mathrm{ph}}\omega_{\mathrm{XFEL}}}{\pi r^2}$. The number of photons per pulse N_{ph} and the focal radius r of the x-ray FEL are within the expected range of the parameters for the self-seeded x-ray FEL being built at the LCLS [26]. All calculations are carried out with $N_{\mathrm{ph}} = 6.4\times10^{12}$ and $\omega_{\mathrm{P}} = 868.2$ eV unless otherwise stated. At these intensities the XRL can saturate and results are acquired that facilitate a clear analysis. The intensity spectrum has a Gaussian shape centered at ω_{XFEL} with FWHM 0.2 eV. The copropagating optical laser has the FWHM duration of $\tilde{t}_{\mathrm{L}} = 13.3$ fs and peak intensity $I_{\mathrm{L}_0} = 7\times10^{12}$ W/cm^2 throughout the chapter.

6.2.1. Optical laser dressing of the XRL

In this section we discuss the optical control of the Ne XRL based on calculations with a Gaussian pump pulse $I_{\mathrm{P}}(z,t)$ with FWHM duration $\tilde{t}_{\mathrm{P}} = 25$ fs and focal radius $r = 1$ μm. Two sets of calculations with the same pump pulse are presented, one for the field-free case and one for the case with optical laser-dressing. Before delving into the analysis of the results, I would like to explain the contents of the figures.

Throughout this section, the black lines show the results of calculations done for the field-free case and the red lines show the results acquired for the case with optical laser-dressing. The temporal shape of the x-ray FEL pump pulse (black) and optical laser pulse (dashed, red) are shown in Fig. (6.6a) before entering the gas cell. Fig. (6.6b) shows the temporal profile of the gain $g(z=0,t)$ calculated at the beginning of the gas cell using the initial, unabsorbed pump pulse from Fig. (6.6a). At the the beginning of the gas cell, the gain $g(z=0,t)$ is not affected by stimulated emission and absorption of the XRL pulse. These only play a role after a certain propagation length when the XRL intensity is so big that the stimulated emission rate and the absorption rate significantly

affect the occupancies of the upper and lower lasing levels. For this reason $g(z = 0, t)$ is identical to the small-signal gain (SSG) cross section, which was defined on page 28 in Sec. (4.2.4). Fig. (6.7a) shows the occupancy of the ground state also calculated at the beginning of the interaction with the initial pump pulse. Fig. (6.7b) shows the occupancies of the upper level (solid lines) and the lower level (dashed lines), which have also been calculated with the initial pump pulse at $z = 0$. Stimulated emission and absorption has no effect on the occupancies at $z = 0$. Throughout this work $N_{\mathrm{N}}(t)$, $N_{\mathrm{U}}(t)$ and $N_{\mathrm{L}}(t)$ refer to the occupancies at $z = 0$, where the z-dependance has been dropped. These are the occupancies used to calculate the SSG. The temporal profiles of the gain $g(z, t)$ and occupancies calculated for points $z > 0$, after a certain distance that the pump pulse has propagated, are different due to the reshaping of the pump pulse by absorption and the onset of the XRL's saturation due to stimulated emission and absorption. The solid lines in Fig. (6.8a) show the peak XRL intensity as a function of the interaction length, which we define as the distance propagated in the gas cell. The dashed lines show the peak gain of the medium also as a function of the interaction length. Thus, the dashed lines show the maximum value of the gain's temporal profile $g(z = z_0, t)$ at every point z_0. For $z = 0$, that is just the peak of the lines in Fig. (6.6b). Fig. (6.8b) displays the same content as Fig. (6.8a), with the difference that stimulated emission and absorption of the XRL pulse has been neglected in all calculations, meaning that the second and third lines on the right-hand side of Eq. (6.11) and Eq. (6.14) have been omitted from the model. Without taking stimulated emission and absorption into account the XRL does not saturate and the intensity increases exponentially throughout the gas cell. The solid lines show the XRL intensity without the effects of saturation and the dashed lines display the peak SSG cross section as a function of the interaction length. Figures (6.9a) (6.9b) display the temporal profiles of XRL intensities $I_{\mathrm{XRL}}(z_0, t)$ at a point z_0 in the gas.

The absorption cross section $\sigma_{\mathrm{N}}^{1s}(I_{\mathrm{L}}, \omega_{\mathrm{XFEL}})$ at the x-ray FEL central frequency is increased through laser-dressing and it is apparent from Fig. (6.6b) that the copropagating optical laser dramatically increases the SSG of the Ne gas. In this example, the peak SSG has been increased from 0.21 Bohr^2 to 0.52 Bohr^2. The optical laser's effect can also

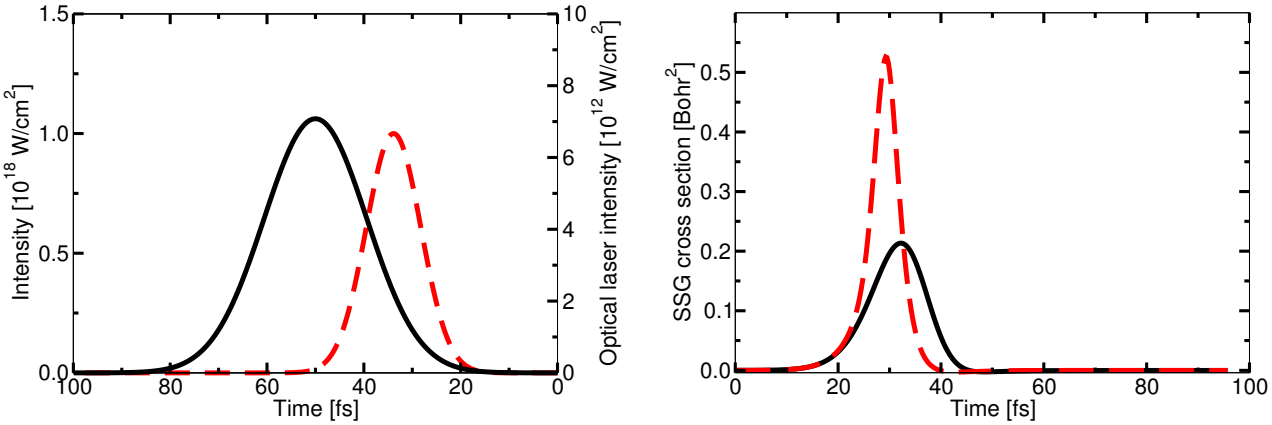

Figure 6.6.: (a) The initial x-ray FEL pump pulse (black) and the optical dressing laser pulse (dashed, red) are shown. (b) SSG without (black) and with (dashed, red) laser dressing.

be observed on the occupancy of the ground state $N_{\mathrm{N}}(t)$, the upper state $N_{\mathrm{U}}(t)$ and the lower state $N_{\mathrm{L}}(t)$ in figures (6.7a) and (6.7b). Comparison of Fig. (6.6a) and Fig. (6.7a) reveals that the gas is totally ionized within the first 40 fs without laser dressing and and within the first 30 fs with laser dressing, meaning that only the front part of the x-ray FEL pulse takes part in the $1s \rightarrow 3p$-excitation of the ground state. However, the remaining part of the pump pulse does not traverse the gas interaction free as it destroys the upper and lower levels of the XRL through ionization of valence electrons as can be seen from Eq. (6.10) and Eq. (6.13). The shape of the gain in the time domain is dominated by the temporal shape of $N_{\mathrm{U}}(t)$ as can be seen upon comparison of Fig. (6.6b) and Fig. (6.7b). There are two reasons for this. First, $\sigma_{\mathrm{abs}} = \frac{g_{\mathrm{U}}}{g_{\mathrm{L}}}\sigma_{\mathrm{se}}$, see Sec. (4.2.3), where g_{U} is the statistical weight of the upper level and g_{L} is the statistical weight of the lower level. One of the $1s$ electrons has been excited so $g_{\mathrm{U}} = 1$ and the $2p$ shell is fully occupied so $g_{\mathrm{L}} = 6$. Only one electron can take part in absorption, but six electrons can take part in a stimulated emission process. Second, the occupancy of the lower level is an order of magnitude smaller than the occupancy of the upper level, as can been observed in Fig. (6.7b).

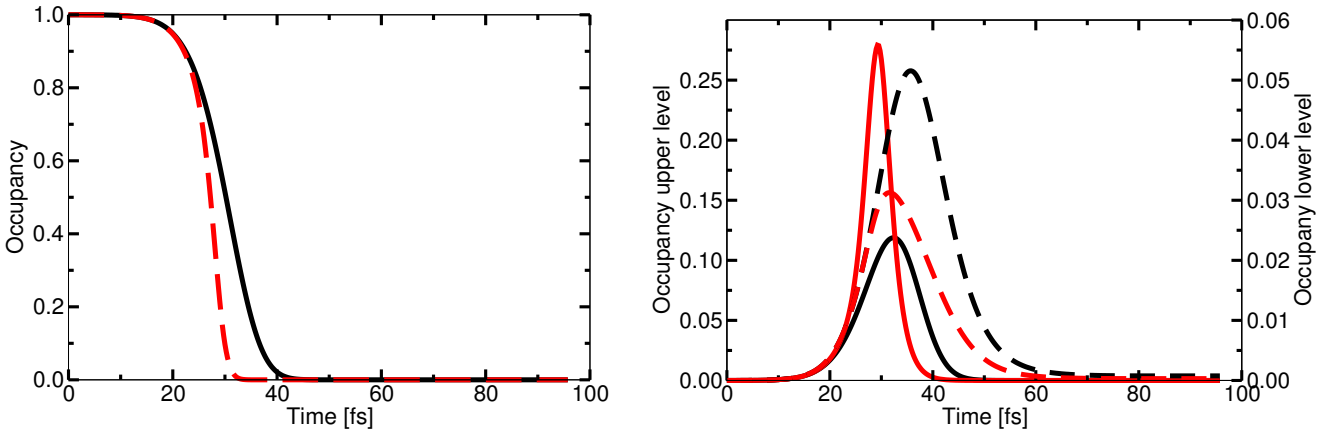

Figure 6.7.: (a) Ground state occupancy at $z = 0$ without (black) and with (dashed, red) optical laser dressing. (b) The upper state occupancy at $z = 0$ is shown with the solid lines without (black) and with (red) optical laser dressing respectively. The lower state occupancy at $z = 0$ is shown with the dashed lines without (black) and with (red) optical laser dressing respectively.

We can now understand how laser dressing effects the XRL. The increase of $N_{\mathrm{U}}(t)$ due to laser dressing is clear as the optical laser increases the absorption cross section for the pumping x-rays from $\sigma_N^{1s}(0,\ 868.2\ \mathrm{eV}) = 86$ kBarn to $\sigma_N^{1s}(7 \times 10^{12}\ \mathrm{W/cm^2},\ 868.2\ \mathrm{eV}) = 720$ kBarn and with it the rate at which the upper level is populated; see the first line on the right-hand side of Eq. (6.9). However, all other terms are not modified, in particular the rate of the upper level's destruction is unaltered as seen in Eq. (6.10). The optical laser's effect on $N_{\mathrm{U}}(t)$ also explains the increase of the gain in Fig. (6.6b).

The solid line in Fig. (6.8a) show the peak XRL intensity as a function of the interaction length. It can be seen in that the exponential build up of the XRL is much faster with laser dressing. This reflects the fact that the gain is considerably increased through laser dressing. Also, the red lines shows that the laser-dressed XRL goes into saturation after

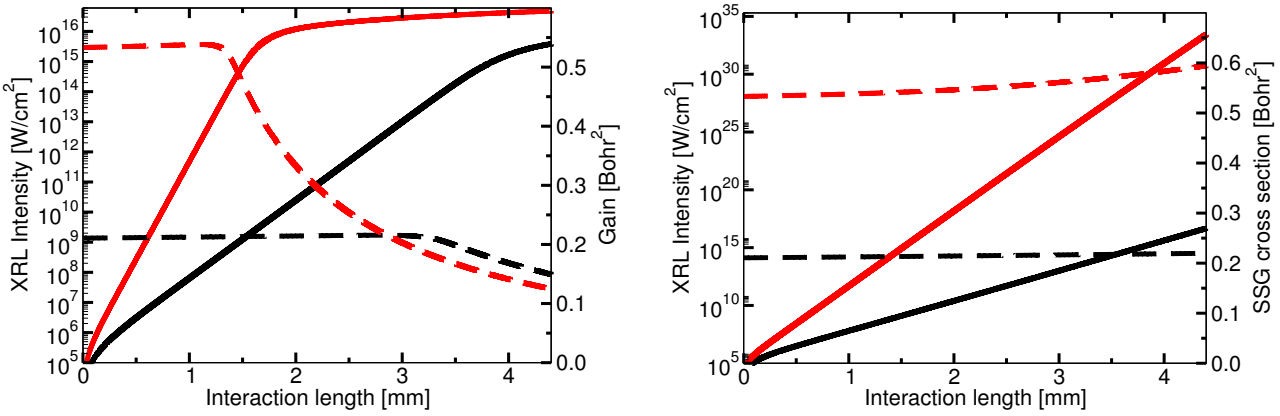

Figure 6.8.: (a) XRL peak intensity (solid lines) is shown as a function of the interaction length without (black) and with (red) laser-dressing. The peak gain (dashed lines) is shown as a function of the propagation distance in the gas without (black) and with (red) laser-dressing.

approximately 1.5 mm in the gas cell and much earlier than the field-free XRL, which starts to saturate only at the very end of the gas cell, as shown by the black line. The shape of the XRL intensity in Fig. (6.8a) is supported by the dashed lines which show the gain. The gain takes a dip when the XRL saturates. The effect of saturation on the gain is well visible at 1.5 mm for the dashed, red line and at about 4 mm for the dashed, black line. The slight increase of the gain before saturation in Fig. (6.8a) is due to absorption which will be discussed in Sec. (6.2.6).

The temporal profiles of the XRL pulses without (black) and with (dashed, red) laser dressing are displayed in Fig. (6.9a) after an interaction length of 1.6 mm just before the laser-dressed XRL saturates. The difference between the peak pulses intensities is the biggest at this point. The intensity of the XRL is increased six orders of magnitude from 1.8×10^9 W/cm^2 to 1.4×10^{15} W/cm^2 by laser-dressing and the XRL pulse duration is compressed from 4.0 fs to 1.1 fs at FWHM. The FWHM duration of the XRL pulse also decreases due to propagation as can be seen upon comparison of Fig. (6.9a) with Fig. (6.9b), which shows the temporal profile of the XRL pulses after an interaction length of 0.5 mm. At this point the XRL has FWHM 7.3 fs without laser dressing (black) and FWHM 2.0 fs with laser dressing (dashed, red). The dashed, blue line in figures (6.9a) and (6.9b) shows the temporal profile of the optical laser pulse. As dispersion is negligible in the Ne gas, the optical laser pulse stays synchronized with the XRL pulse in the entire gas cell.

6.2.2. Dependence on the overlap between x-ray pump pulse and optical laser pulse

The effect of laser-dressing on the XRL strongly depends on the optical laser's relative temporal position to the pump pulse. The two copropagating pulses need to coincide in a specific way in order to achieve good control over the XRL. The calculations in this section have been done with Gaussian x-ray pump pulses, see Eq. (6.19) with FWHM duration of $\tilde{t}_p = 50$ fs and focal radius $r = 1\mu$m. In this section, black lines show the

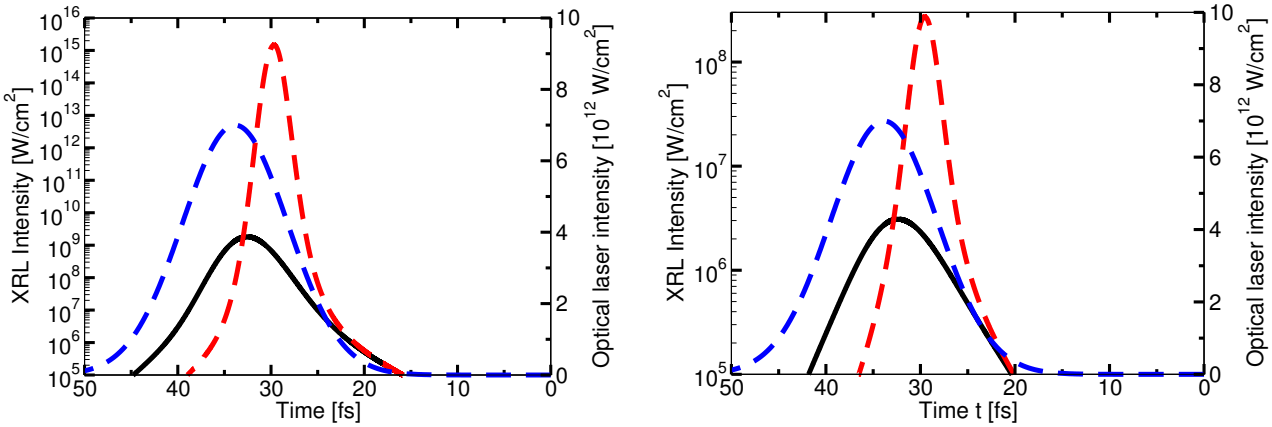

Figure 6.9.: (a) Temporal profile of the XRL pulses after an interaction length of 1.6 mm just before saturation is shown without (black) and with (red) laser dressing. (b) Temporal profile of the XRL pulses after an interaction distance of 0.5 mm is displayed without (black) and with (red) laser dressing.

pump pulse in Fig. (6.10a) and the results of the field-free calculations in all other figures. The dashed, colored lines show the optical laser pulses in Fig. (6.10a) and the results of laser-dressed calculations with the optical laser pulse of the same color in all other figures.

The red lines always show the best-case scenario. For this ideal overlap between the copropagating optical laser and x-ray FEL pulse shown in Fig. (6.10a), the peak SSG is increased more than threefold from 0.11 Bohr^2 to 0.38 Bohr^2, see Fig. (6.10b). If the optical laser arrives just 20 fs earlier relative to the pump pulse as shown by the blue, dashed line in Fig. (6.10a), the peak SSG is increased less than twofold to 0.19 Bohr^2, see Fig. (6.10b). The difference is even bigger if the optical laser pulse is placed 20 fs behind the dashed, red line, as shown by the dashed, green line in Fig. (6.10a). In this case the majority of the ionizing part of the pump pulse passes the atoms before the absorption cross section $\sigma_N^{1s}(I_L, \omega_{\mathrm{XFEL}})$ is increased through laser-dressing and only a small change of the SSG can be observed in comparison to the black line in Fig. (6.10b). For optical laser pulses that arrive even later relative to the x-ray pump pulse no effect on the XRL's gain can be observed, because the ground state has been completely ionized by the time they dress the atoms.

By looking at the occupancy $N_{\mathrm{N}}(t)$ of the ground state in Fig. (6.11a), one can deduce that the optical laser pulse must overlap with the rising flank on the pump pulse in a way that facilitates the ionization of atoms in the shortest possible time. The biggest population inversion is achieved this way, because the upper level is populated so fast that only little decay of the upper level can happen within that time. If ionization is less rapid upper-level decay removes population while the upper level is still being populated. It can be seen in Fig. (6.10a) that in the ideal case the red, dashed lines and the black lines do not coincide for approximately the first 18 fs. This is because the intensity at the front of the x-ray FEL pulse is so small that it hardly contributes to the ionization of the ground state. The occupancy $N_{\mathrm{G}}(t)$ of the ground state drops merely to 0.92 in the first 18 fs of the interaction for the solid, black line and the dashed, red line in Fig. (6.11a).

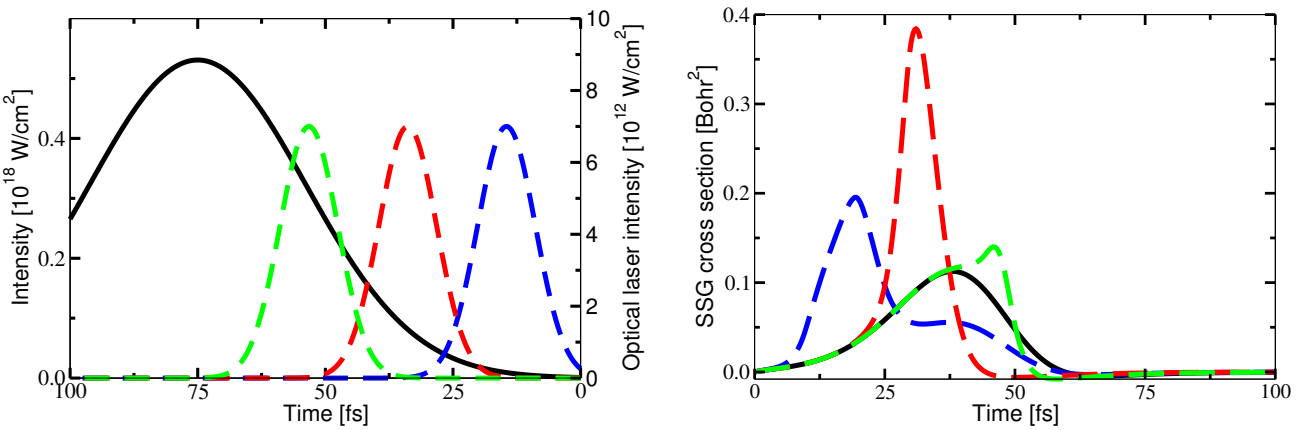

Figure 6.10.: Dependence of gain modulation on the optical laser's position. Red lines illustrate the ideal case. (a) X-ray FEL pump pulse (black line) and optical laser pulses (colored dashed lines) at different positions. (b) XRL's SSG for the field-free case (black line) and for the case with laser-dressing (colored dashed lines) for different positions of the optical laser pulse relative to the x-ray FEL pulse.

Thus, it is not beneficial to dress the atoms for this duration. For the best result the laser must increase the absorption cross section $\sigma_N^{1s}(I_L, \omega_{\mathrm{XFEL}})$ during the time interval when the atoms are interacting with the part of the x-ray FEL pulse that is mainly responsible for the excitation.

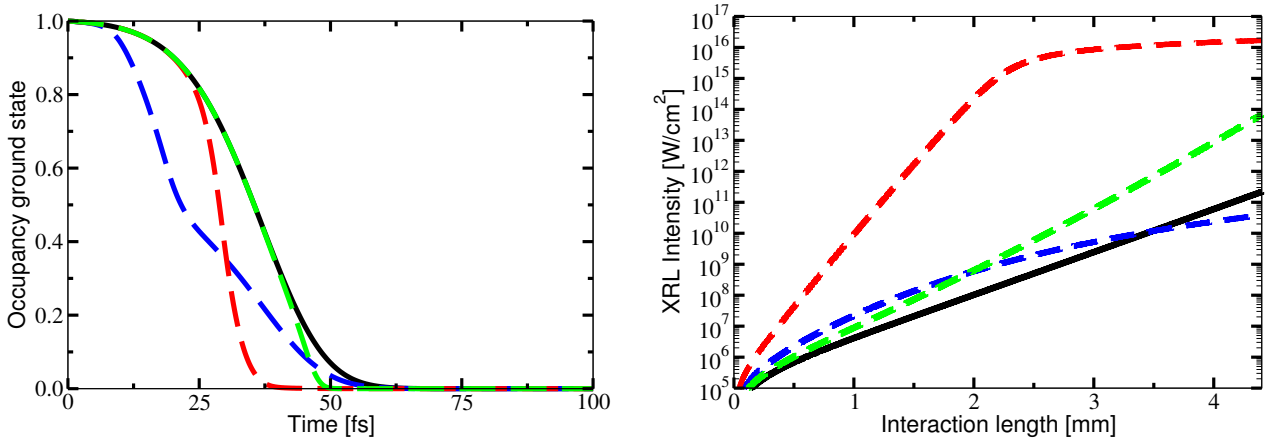

Figure 6.11.: (a) Occupancy $N_{\mathrm{N}}(t)$ of the groundstate and (b) XRL intensity. In both graphs the solid, black line shows the field-free case and the dashed lines show cases with laser-dressing for the optical pulses of the color in Fig. (6.10b).

The peak XRL intensity as a function of the interaction length for the field-free case and the three laser-dressed cases is shown in Fig. (6.11b). Only the red, dashed line reaches saturation. The XRL does not saturate for the field-free case and for laser-dressing with the dashed, blue and green optical laser pulses in Fig. (6.10a). The blue dashed line's slope decreases over the interaction distance due to absorption effects that will be elaborated on in Sec. (6.2.6).

6.2.3. Dependence on the optical laser's intensity

As explained in Sec. (5.2) the magnitude of the absorption cross section's modulation through laser-dressing depends on the the optical laser pulse's intensity. Fig. (6.12a) displays the the absorption cross section for the field-free case (black) and the peak, optical laser-dressing intensities of 10^{12} W/cm^2 (green), $3{\times}10^{12}$ W/cm^2 (blue) and $7{\times}10^{12}$ W/cm^2 (red). The value of the absorption cross section at the x-ray FEL central frequency, which is denoted with the vertical orange line, increases with growing peak, optical laser intensities.

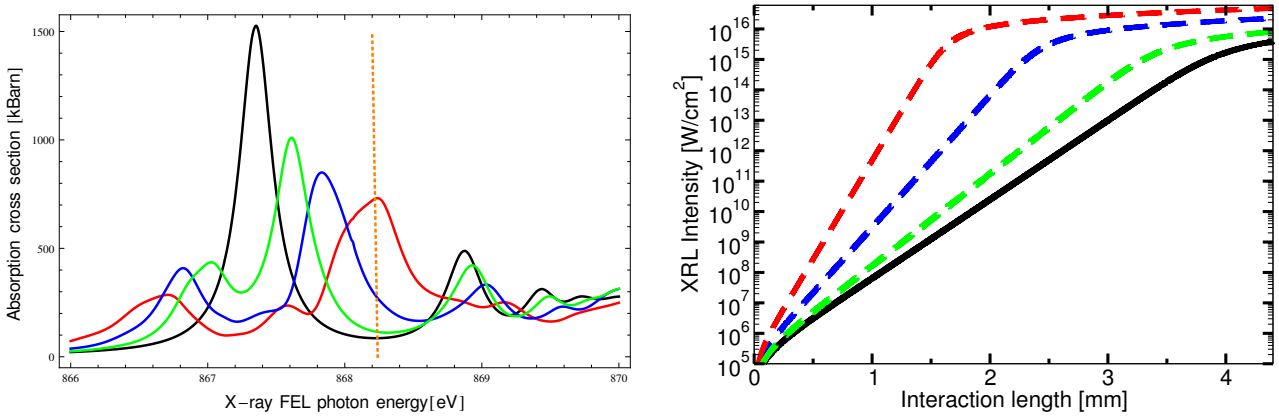

Figure 6.12.: (a) The absorption cross section is shown for the field-free case in black and for laser-dressing with an optical laser intensity of 10^{12} W/cm^2 in green, 3×10^{12} W/cm^2 in blue and 7×10^{12} W/cm^2 in red. The dotted, orange line denotes the x-ray FEL central frequency ω_{XFEL}. (b) The XRL's intensity is shown as a function of the interaction length for the scenarios of the same color in (a).

We choose an x-ray pump pulse with the FWHM duration of $\tilde{t}_P = 10$ fs, the focal radius $r = 1$ μm and the number of photons per shot $N_{\mathrm{ph}} = 2.5 \times 10^{12}$. This results in a peak intensity of 10^{18} W/cm^2. Fig. (6.12b) shows the peak XRL intensity as a function of the interaction length in matching colors for the field-free case and the three different laser-dressing intensities from Fig. (6.12a). The XRL's output intensity can be controlled via the optical laser's intensity. With this mechanism it is possible to imprint the transverse intensity profile of an optical laser pulse onto the XRL pulse as there are no correlations in the transverse direction.

6.2.4. Dependence on the x-ray FEL's intensity

In order to show how the XRL's gain and peak intensity change with varying pump intensity we compare calculations where all parameters are kept the same except for the focal radius r. The x-ray pump pulse has FWHM duration of $\tilde{t}_P = 10$ fs and the number of photons per shot is $N_{\mathrm{ph}} = 2.5 \times 10^{12}$. The relative position of the optical laser pulse to the XFEL pulse has been set to cause maximum modulation of the XRL's gain $g(z,t)$. In figures (6.13a), (6.13b) and (6.14), which are discussed in this subsubsection, the blue lines show results for the case when the pumping x-ray FEL pulse is focused to $r_1 = 7.5\mu$m

and the red lines show results for the case when $r_2 = 1\mu$m. Also, the solid lines always correspond to the field-free case and the dashed lines always correspond to the case when the copropagating optical laser is turned on. The peak intensity of the x-ray FEL pulse drops from 10^{18} W/cm^2 to 1.8×10^{16}W/cm^2 when the radius is increased from 1μm to 7.5μm, which is a reduction by a factor of approximately 56 ($\approx 7.5^2$).

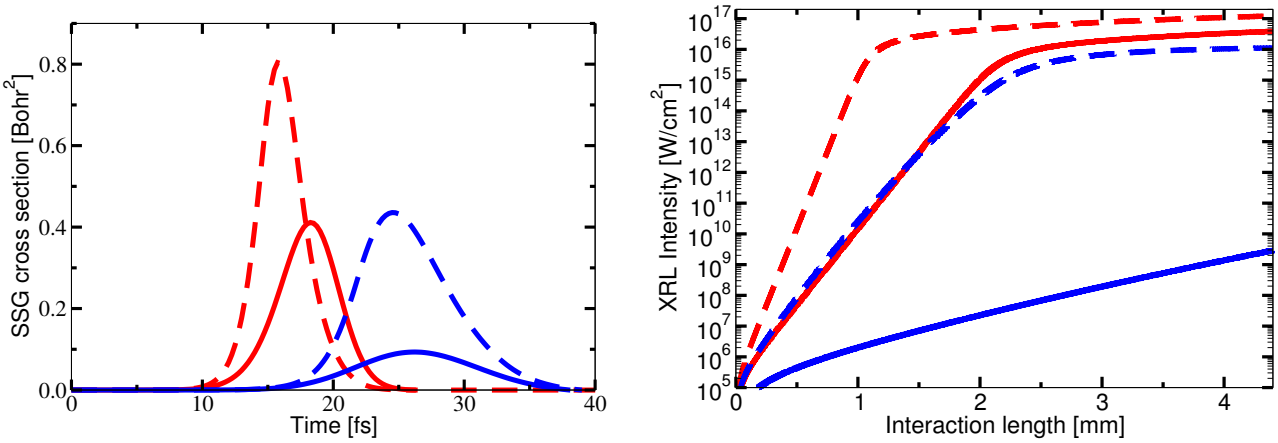

Figure 6.13.: (a) The blue lines show the SSG for a focal radius $r_1 = 7.5\mu$m and the red lines show the SSG for a focal radius $r_2 = 1\mu$m. In both cases, the solid lines belong to the field-free case and the dashed lines show the case with a copropagating optical laser pulse. (b) The peak XRL intensities are plotted as a function of the propagation distance for an x-ray FEL pump pulse with peak intensity of 10^{18}W/cm^2 (red) and 1.8×10^{16}W/cm^2 (blue), and for the cases with (dashed) and without (solid) laser dressing.

The plot in Fig. (6.13a) shows the SSG for the four cases introduced above. The lower pumping intensity leads to a temporally longer SSG with generally smaller values which becomes evident by comparing the red and blue lines in Fig. (6.13a). As discussed in Sec. (6.2.1) the shape of the SSG is dominated by the upper level occupancy $N_{\mathrm{U}}(t)$. In order to understand the mechanism leading to the differences between the results shown by the blue and the red lines, let us discuss Eq. (6.11).

We simplify Eq. (6.9) by substituting $I_{\mathrm{P}}(z,t)$ with the peak x-ray FEL intensity I_{P_0} to estimate the changes in the population and depletion rate of the upper level. In this approximation, the rate at which the upper level is populated decreases by a factor of 56.25 when the focal radius is increased from $r_1 = 1$ μm to $r_1 = 7.5$ μm and I_{P_0} decreases from 10^{18} W/cm^2 to 1.8×10^{16} W/cm^2. If the depletion rate is given Eq. (6.10) was smaller by the same factor of 56.25, then pumping with the less intense x-ray FEL pulse would result in the same temporal profile of the occupancies and the SSG as shown by the red lines in Fig. (6.13a), just over a longer time interval. However, this is not the case due to the appearance of the Auger decay rate Γ_{Tot} in Eq. (6.10). Calculating $\Gamma_{\mathrm{Tot}} + \sigma_{\mathrm{U}}^{\mathrm{Tot}} \frac{I_{\mathrm{P}_0}}{\omega_{\mathrm{XFEL}}}$ with the values from Tab. (6.1) reveals that the rate of depopulation is merely reduced by a factor of 2.58 when lowering the peak x-ray FEL intensity from 10^{18} W/cm^2 to 1.8×10^{16} W/cm^2. This leads to the smaller values of the SSG. This small change of the depopulation rate explains why the SSG and with it the population inversion is longer in time, as the upper laser level is destroyed less rapidly.

A further effect of lowering the pump intensity is that the modulation of the SSG caused by laser dressing is much bigger, as seen by comparing the blue and red lines in Fig. (6.13a). For $r_2 = 1\mu$m the peak value of the SSG increases approximately twofold from 0.41 Bohr^2 to 0.80 Bohr^2, while for $r_1 = 7.5\mu$m the peak value increases over fourfold from 0.09 Bohr^2 to 0.43 Bohr^2! The peak XRL intensities are displayed in Fig. (6.13b) for the four cases. By comparing the XRL intensities with and without laser-dressing for both pump pulses respectively, one reaches the same conclusion as based on the SSG. Just before saturation of the red, dashed line after 1 mm propagation, the value of the red, dashed line is five orders of magnitude bigger than the value of the solid red line, meaning that at the higher pump intensity laser-dressing increases the XRL's peak intensity by five orders of magnitude. This difference for the blue lines before saturation of the dashed blue line at 2 mm is more than seven orders of magnitude, meaning that at the lower pump intensity laser-dressing increases the XRL's intensity by seven orders of magnitude. This observation can once again be explained with Eq. (6.11). Laser dressing changes the photoionization cross section from $\sigma_{\mathrm{N}}^{1s}(0, \omega_{\mathrm{XFEL}})$ to $\sigma_{\mathrm{N}}^{1s}(I_{\mathrm{L}}, \omega_{\mathrm{XFEL}})$, meaning that only the pumping rate shown in Eq. (6.9) is affected. Since $\sigma_{\mathrm{N}}^{1s}(I_{\mathrm{L}}, \omega_{\mathrm{XFEL}})$ is independent of the x-ray FEL's intensity, it changes in the same way for both pumping scenarios. However, the occupancy of the groundstate $N_{\mathrm{N}}(z,t)$, which also appears in the first line on the right-hand side of Eq. (6.9), changes significantly due to laser-dressing for $r_1 = 7.5\mu$m (blue lines), as seen in Fig. (6.14), while for $r_2 = 1\mu$m (red lines) the effect of laser-dressing is more subtle. The reason is that the pumping intensity for focal radius $r_2 = 1\mu$m is already so high that the ground state is rapidly ionized and completely depopulated even without laser-dressing, as seen in Fig. (6.14). The acceleration of the excitation process has a smaller magnitude.

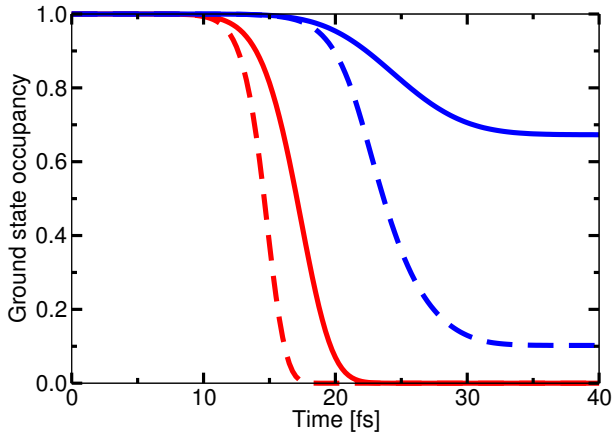

Figure 6.14.: The red lines show the occupancy of the ground state $N_{\mathrm{N}}(t)$ when pumped with an x-ray FEL pulse with peak intensity 10^{18} W/cm^2 and the blue lines show the occupancy when pumping with a peak intensity of 1.8×10^{16} W/cm^2. The solid lines show the field-free case and the dashed lines show the lase-dressed case.

6.2.5. Dependence on the x-ray FEL pulse duration

In this section, we illustrate how the length of the pump pulse effects the XRL. The calculations have been done for the focal radius $r = 1\mu$m and the overlap of the optical laser pulse and the pump pulse are chosen to result in the greatest modulation of the gain. Three x-ray FEL pulse lengths are compared with FWHM duration 10 fs (red), 25 fs (blue) and 100 fs (green). The pulses are shown in Fig. (6.15a) and the SSG for each pump pulse is shown with the same color in Fig. (6.15b). The solid lines show the results of the field-free calculations and the dashed lines show the results with laser-dressing. An increase in the pulse duration leads to a decrease in the pulse intensity which can be seen in Eq. (6.20) because the number of photons $N_{\mathrm{ph}} = 2.5 \times 10^{12}$ per pulse and the focal radius $r = 1\mu$m are held constant. This results in a smaller and longer SSG analogously to Sec. (6.2.4).

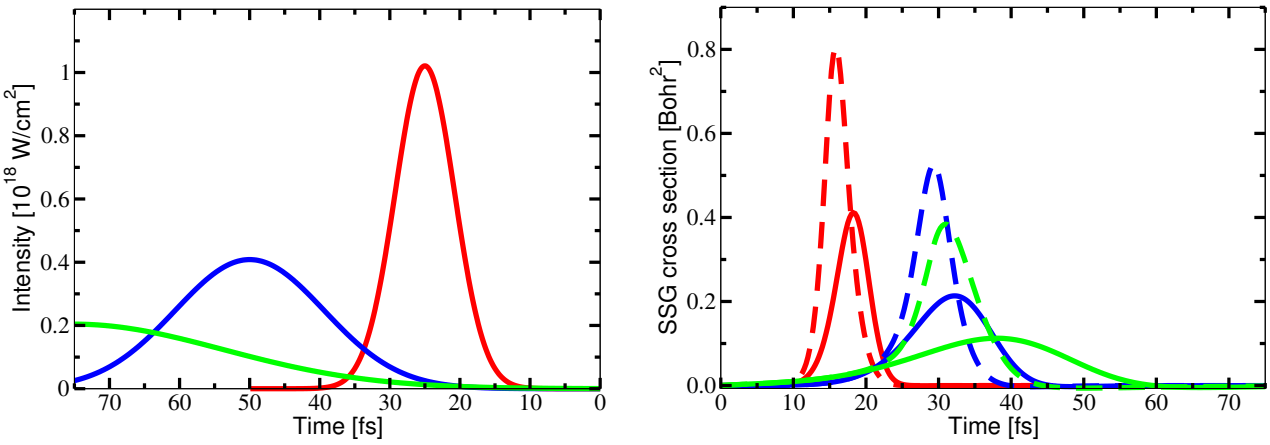

Figure 6.15.: (a) XFEL pulses with FWHM 10 fs (red), 25 fs (blue) and 50 fs (green). Since the number of photons per pulse $N_{\mathrm{ph}} = 2.5 \times 10^{12}$ and the focal radius $r = 1$ μm are the same, the intensity decreases with increasing duration of the pulses. (b) Corresponding SSGs for the field-free case (continuous lines) and the case with laser-dressing (dashed lines).

To investigate the effect of the pump pulse's rise time on the SSG, we have done calculation with varying pulse durations while keeping the peak intensity the same for all pulses. This can be achieved by either increasing the number of photons N_{ph} per pulse or decreasing the focal radius r while increasing the pulse duration. X-ray FEL pulses with FWHM 10 fs (red), 25 fs (blue) and 50 fs (green) are shown in Fig. (6.16a) for the constant peak intensity of 10^{18} W/cm^2. Longer rise times lead to smaller and longer SSGs, as the very flat low intensity front of the pump pulse does the ionization at a low rate [33] as can be observed in Fig. (6.16b). Generally lower x-ray FEL intensities can be advantageous as optical control over the XRL is better. Regardless of this, short rise times are important to build up a population inversion, such that it is better to keep the pulse FWHM short.

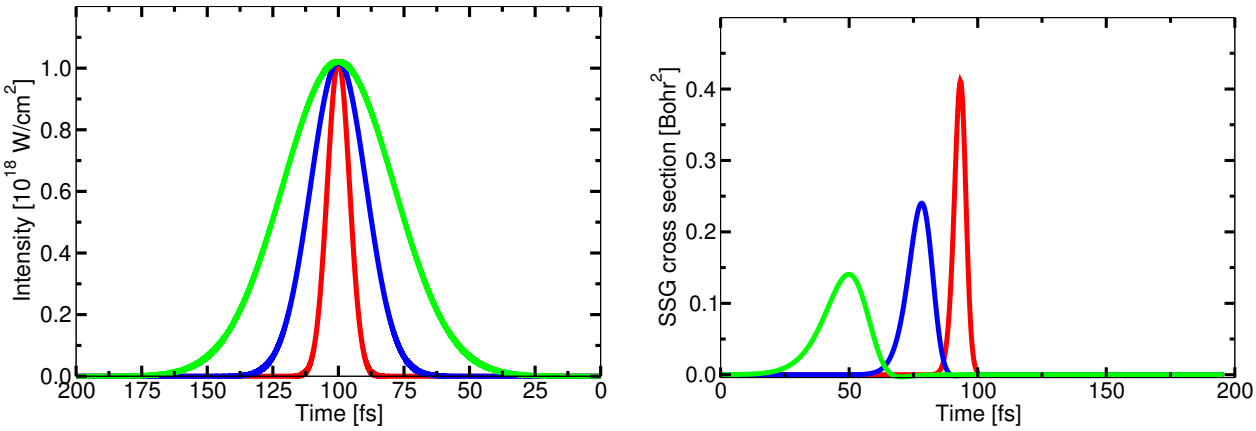

Figure 6.16.: (a) X-ray FEL pulses with FWHM 10 fs (red), 25 fs (blue) and 50 fs (green). In order to keep the peak intensity of the blue and green pulses at 10^{18}W/cm^2, the number of photons per pulse N_{ph} has been increased by a factor 2.5 and 5 for the 25 fs and 50 fs pump pulses, respectively. (b) SSG achieved by the pump pulses shown in (a) with the same colors.

6.2.6. Influence of the x-ray FEL pulse's absorption

We discuss different calculations using an x-ray FEL pump pulse with FWHM duration $\tilde{t}_P = 10$ fs. All calculations have been done for photons $N_{\mathrm{ph}} = 2.5 \times 10^{12}$ per pulse, and a focal radius $r_1 = 7.5$ μm and $r_2 = 1$ μm to illustrate that absorption affects the XRL in different ways for a low pumping intensity than it does for a high pumping intensity. This section only deals with the case when the optical laser is turned on.

First, we discuss the XRL with focal radius $r_1 = 7.5$ μm. The initial x-ray FEL pump pulse before entering the gas cell has the peak intensity of $1.8{\times}10^{16}$ W/cm^2 and is shown in Fig. (6.17a) together with the optical laser pulse. The relative position of the copropagating pulses has been chosen to achieve maximum modulation of the gain. We compare the results of three separate calculations that are shown in Fig. (6.17b): namely, the peak SSG cross section as a function of the interaction length when neglecting absorption of the x-ray FEL pulse (solid, black); the peak SSG cross section as function of the interaction length when absorption of the x-ray FEL pulse is taken into account (solid, blue); and the peak gain cross section as a function of the interaction length taking absorption of the x-ray FEL pulse into account (dashed, red). Absorption of the x-ray FEL pulse profoundly affects the SSG cross section as can be seen by comparison of the solid, black and blue lines. The explanation is that whilst propagating through the gas the x-ray FEL pump pulse is absorbed, meaning that the pumping intensity decreases with the propagation distance as can be seen in Fig. (6.18a), where the x-ray FEL pulse and the optical laser pulse are shown after traversing the entire 4.4 mm of the gas. The x-ray FEL pulse has been totally reshaped by absorption and its peak intensity has dropped to $5.5{\times}10^{15}$ W/cm^2 which is close to an order of magnitude smaller than initially. Due to the smaller pump intensity, a smaller population inversion is built up. The gain (dashed, red) and SSG (solid, blue) follow the same trend until an interaction length of approximately 1.8 mm where saturation of the XRL sets in. The XRL intensity is displayed in Fig. (6.18b). The black line shows the exponential growth of the intensity

when stimulated emission and absorption of the XRL pulse as well as the absorption of the x-ray FEL pump pulse are neglected. The blue line also shows the SSG, but absorption of the x-ray FEL pulse is now taken into account. Even though saturation effects do not occur, the intensity shown by the blue line does not increase exponentially due to the absorption of the x-ray FEL pulse and the decreasing pump intensity. The dashed, red line shows the results for the complete model. Saturation is clearly visible at an interaction length of approximately 2.2 mm.

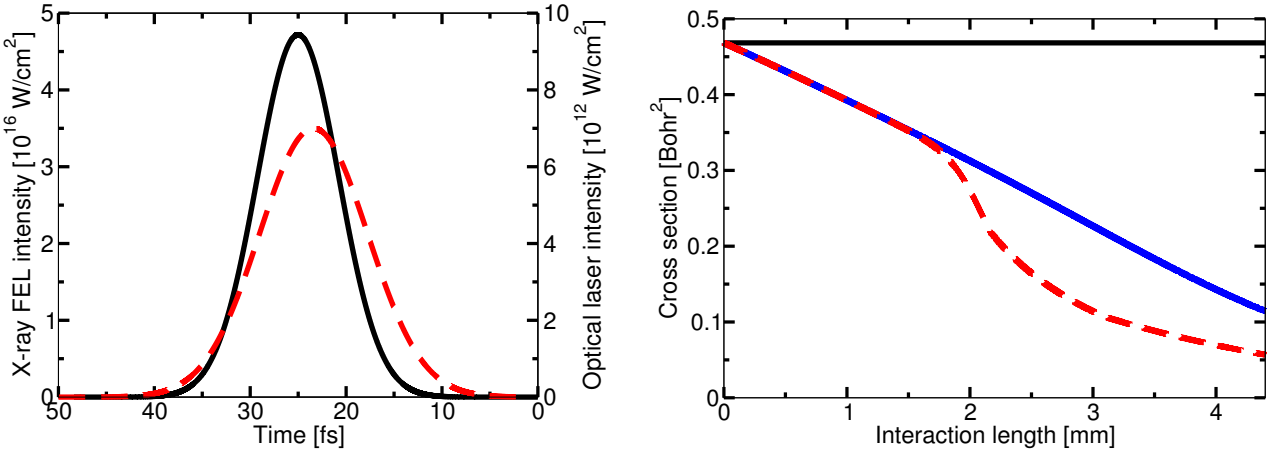

Figure 6.17.: (a) The initial x-ray FEL pump pulse (black) and the optical laser pulse (dashed, red) is shown. (b) The black line shows the peak SSG as a function of the interaction length while neglecting absorption of the x-ray FEL pulse. The blue line shows the peak SSG when absorption of the x-ray FEL pulse is considered. The dashed red line shows the gain cross section for the complete model from Sec. (6.1).

We discuss the effects of absorption for the focal radius $r_2 = 1$ μm and the peak x-ray FEL intensity of 10^{18} W/cm^2. The initial x-ray FEL pump pulse and the optical laser pulse are shown in Fig. (6.19a). The position of the optical laser has been chosen to achieve the maximum modulation of the gain. The three lines in Fig. (6.19b) display: the peak SSG cross section as a function of the interaction length when neglecting absorption of the x-ray FEL pulse (solid,black); the peak SSG cross section as function of the interaction length when absorption of the x-ray FEL pulse is taken into account (solid, blue); and the peak gain cross section as a function of the interaction length taking absorption of the x-ray FEL pulse into account (dashed, red). Absorption of the x-ray FEL has a profoundly different effect for the more intense x-ray FEL pump pulse that we now consider. The black and blue lines in Fig. (6.17b) show the SSG, but absorption leads to an increase of the blue line's value as a function of the propagation distance. This can be understood by looking at the final x-ray FEL pulse that exits the gas cell in Fig. (6.20a). Because of the x-ray FEL pulse's far higher intensity than for the focal radius $r_1 = 7.5$ μm the alteration of the pulse's shape due to absorption is much smaller. Comparison with the dashed green line which depicts the initial pulse shape shows that only the low intensity front part of the x-ray FEL pulse is absorbed. After propagation the x-ray FEL pulse has a steeper flank and shorter rise time which results in the increasing SSG displayed by the blue line in Fig. (6.19b). The gain displayed by the dashed red line in Fig. (6.19b) follows

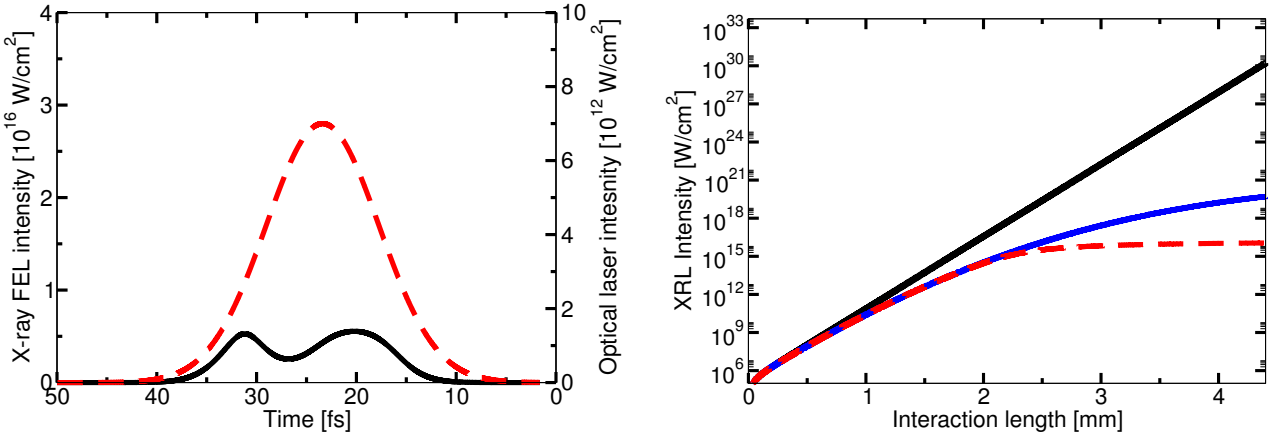

Figure 6.18.: (a) The final x-ray FEL pulse (black) and the optical laser pulse are displayed after propagation through the gas. Since dispersion is negligible the pulses still overlap, however significant reshaping of the x-ray FEL pulse has taken place due to absorption. (b) The black line shows the XRL intensity calculated when neglecting stimulated emission and absorption of the XRL pulse, as well as neglecting the absorption of the x-ray FEL pulse. The blue line is the same as the black line except the absorption of the x-ray FEL pulse is taken into account. The dashed red line is the XRL intensity calculated by taking stimulated emission and absorption of the XRL pulse and absorption of the x-ray FEL pulse into account.

the SSG until saturation sets in just as expected. The XRL output is displayed for the three different calculations in Fig. (6.20b).

6.3. Pumping with SASE pulses

In this section, we discuss some results obtained by using model LCLS pulses for pumping the XRL. The SASE pulses are produced with the Partial Coherence Method (PCM) [70].

First, I present results for pumping with SASE pulses produced at the Atomic, Molecular and Optical Science facility at LCLS [26] with 5×10^{12} photons per pulse, a pulse duration of 100 fs, a focal diameter of 1μm and a spectral FWHM of 4.3 eV. Due to the chaotic nature of x-ray FEL radiation, we present averaged results over many shots to eliminate the statistical variations observed on a shot-by-shot basis.

The averaged pulse intensity (black) of 300 shots is displayed together with the optical laser pulse (dashed red) in Fig. (6.21a). The temporal profile of the averaged x-ray FEL pulse is still chaotic due to the small sample size. A Gaussian profile would be obtained for an averaged over more shots. The averaged SSG over 300 calculations is presented in Fig. (6.22a) with black for the field-free case and with red for the case with laser-dressing. Due to the broad spectral width of the radiation, hardly any modulation of the SSG is observed. This result can be understood by looking at the spectral intensity which is plotted with red in Fig. (6.21b) together with the absorption cross section $\sigma_N^{1s}(I_P, \omega_X)$ for the field-free case in blue and for the case with laser-dressing in green. The average absorption cross section calculated with the convolution of the spectrum and the absorption

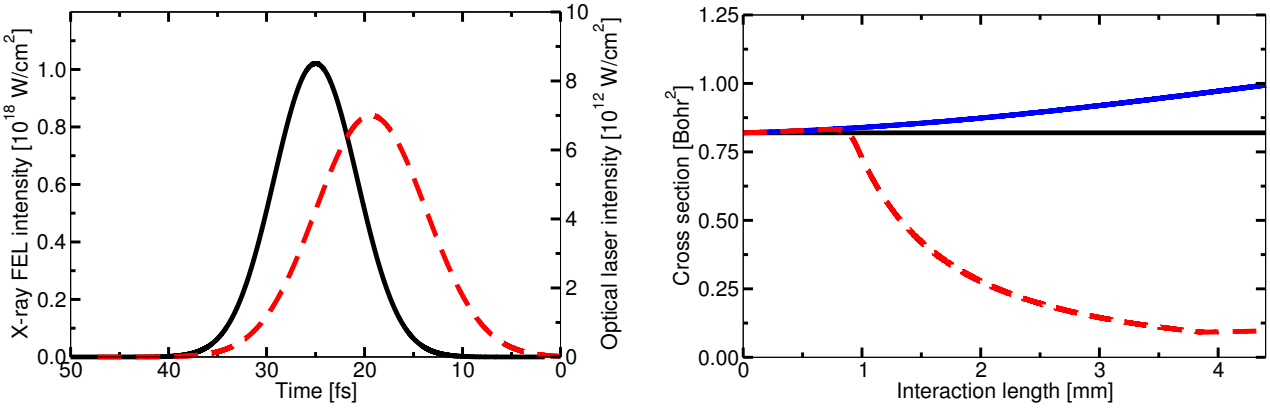

Figure 6.19.: (a) The initial x-ray FEL pump pulse (black) and the optical laser pulse (dashed red) is shown. (b) The black line shows the peak SSG as a function of the interaction length while neglecting absorption of the x-ray FEL pulse. The blue line shows the peak SSG when absorption of the x-ray FEL pulse is considered. The dashed red line shows the gain cross section for the complete model from Sec. (6.1).

cross section

$$\langle \sigma_N^{1s}(I_L) \rangle_{\omega_P} = \frac{\int_0^\infty \sigma_N^{1s}(I_L, \omega_P) \frac{S_P(z,\omega_P)}{\hbar\omega_P} d\omega_P}{\int_0^\infty \frac{S_P(z,\omega_P)}{\hbar\omega_P} d\omega_P} \tag{6.21}$$

appears in the first line on the right-hand side of Eq. (6.11). It is nearly identical for the cases with and without laser-dressing. The average absorption cross section for the field-free case is $\langle \sigma_N^{1s}(I_L = 0) \rangle_{\omega_P} = 225$ kBarn and for the case with laser-dressing it is $\langle \sigma_N^{1s}(I_L = 7 \times 10^{12} \mathrm{W/cm^2}) \rangle_{\omega_P} = 223$ kBarn. It is necessary to limit the bandwidth of the pump pulse so that the average absorption cross section increases when the copropagating optical laser is turned on. We illustrated this relationship in Fig. (6.23). The spectral intensity and the absorption cross sections are shown on the left and the SSG on the right for the field-free case and the laser-dressed cases, respectively. The x-ray FEL's bandwidth is restricted to 1.5 eV in the top panel and to 0.4 eV in the bottom panel. Some modulation of the SSG is visible at an x-ray FEL bandwidth of 1.5 eV, however, the effect only becomes significant at a bandwidth of approximately 0.4 eV, when the spectral intensity's FWHM becomes comparable with the width of the resonance in the laser-dressed absorption cross section at 868.2 eV.

For the remainder of the section model SASE x-ray FEL pulses with a bandwidth of 0.4 eV are used to pump the XRL. The other parameters are as defined at the beginning of the section. Currently, pulses with this combination of properties cannot be produced at any x-ray FEL facility. The Soft X-ray Material Science facility at LCLS [26] is capable of creating pulses with a bandwidth of 0.4 eV, however, only at significantly lower intensities. Single-shot calculation of the SSG are presented in Fig. (6.24a), Fig. (6.25a) and Fig. (6.26a) with black for the field-free case and with red for the laser-dressed case. The calculations are carried out with pump pulses of 100 fs duration that are displayed in Fig. (6.24b), Fig. (6.24b) and Fig. (6.26b), respectively, with black together with the optical laser pulse in red. The position of the optical laser is the same in all three calcu-

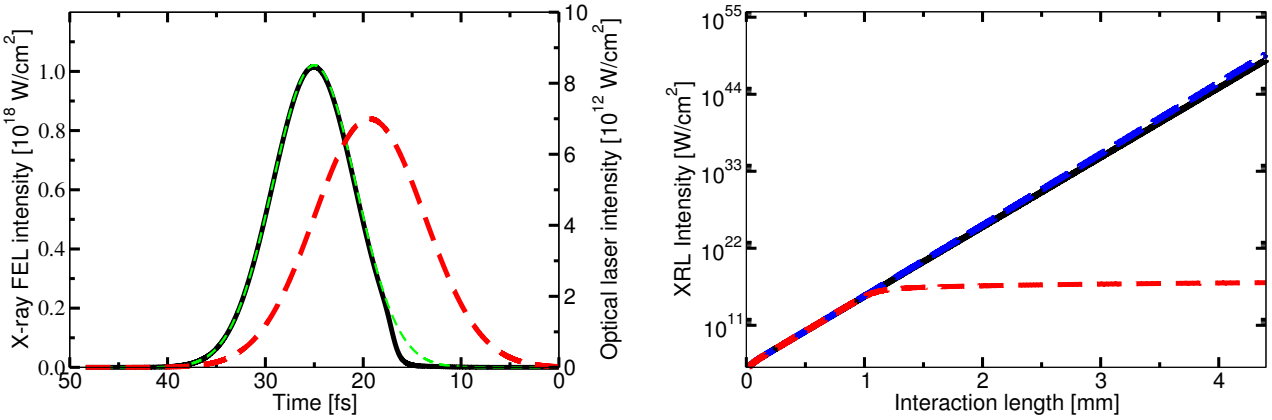

Figure 6.20.: (a) The final x-ray FEL pulse (black) and the optical laser pulse are displayed after propagation through the gas. Since dispersion is negligible the pulses still overlap, however significant reshaping of the x-ray FEL pulse has taken place due to absorption. (b) The black line shows the XRL intensity calculated when neglecting stimulated emission and absorption of the XRL pulse, as well as neglecting the absorption of the x-ray FEL pulse. The blue line is the same as the black line except the absorption of the x-ray FEL pulse is taken into account. The dashed red line is the XRL intensity calculated by taking stimulated emission and absorption of the XRL pulse and absorption of the x-ray FEL pulse into account.

lations. The XRL intensity and the gain is shown as a function of the interaction length for the pump pulse from Fig. (6.24b) in Fig. (6.27a), for the pump pulse from Fig. (6.25b) in Fig. (6.27b) and for the pump pulse from Fig. (6.26b) in Fig. (6.28) . The results for the SSG are very distinct due to the different shape of the pump pulses which vary on a shot-by-shot basis. The importance of the optical laser pulse's timing with respect to the SASE pulse is exhibited. Even though laser-dressing leads to a strong modulation of the SSG in Fig. (6.24a), the XRL's output is not increased, it is in fact decreased as shown in Fig. (6.27a). The reason is that the peak SSG is actually reduced through laser-dressing due to the unfavorable overlap between the optical laser pulse and the SASE pulse. The absorption cross section is increased at a point in time when the Ne atoms interact with a relatively low intensity part of the SASE pulse, which hardly ionizes the atoms in the field-free case. The other two scenarios display cases when the XRL's output is significantly increased through laser-dressing and show that pump pulses with a chaotic temporal and spectral profile can also be used to effectively pump the XRL.

6.4. Attosecond XRL pulse generation

As discussed in Sec. (6.2.5) x-ray pump pulses with short rise times and high intensities are necessary in order to produce short population inversions. Here we use a x-ray pump pulse with photons per shot $N_{\mathrm{ph}} = 2.5 \times 10^{12}$, FWHM duration of 10 fs, spectral FWHM of 0.2 eV and a peak intensity of 10^{18} W/cm^2 to pump the XRL, as shown in Fig. (6.29a) with the black line along with the optical laser pulse which is shown in red. This results in the gain and output intensity shown in Fig. (6.29b), where the solid line display the

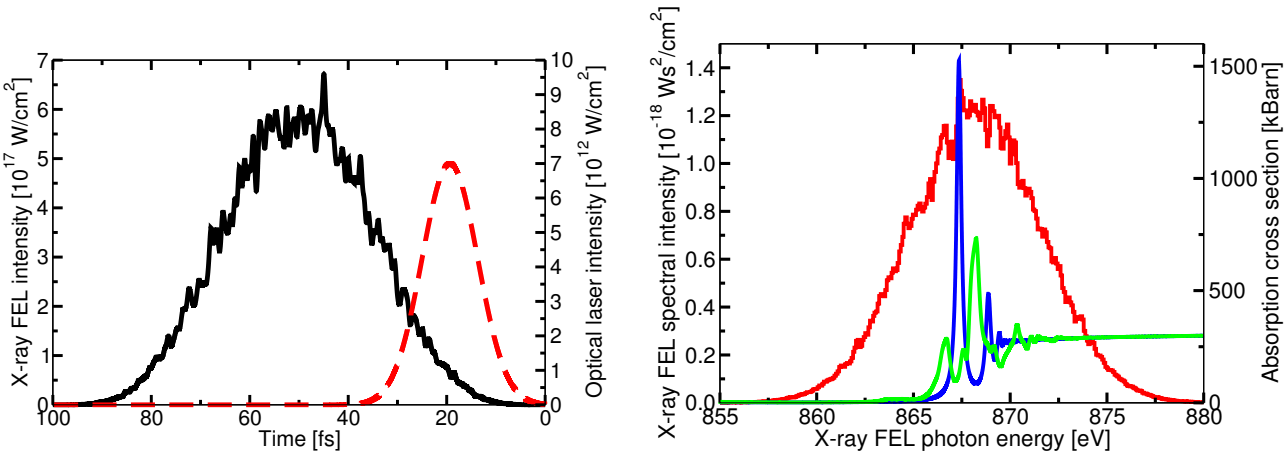

Figure 6.21.: (a) X-ray FEL pump pulse intensity averaged over 300 shots (black) and optical laser pulse, which has the same relative temporal position to each single-shot x-ray FEL pulse (red). (b) Averaged x-ray FEL intensity spectrum (red), absorption cross section for the field-free case (blue) and the absorption cross section for a laser-dressing intensity of 7×10^{12} W/cm^2 (green).

XRL intensity and the dashed lines show the gain as a function of the interaction length in black for the field-free case and in red for the laser-dressed case. At saturation of the laser-dressed XRL, after 1 mm propagation, the XRL pulses have the temporal profile shown in Fig. (6.30), where the black line corresponds to the field-free case and the red line to the laser-dressed case. The FWHM duration of the laser-dressed XRL pulse is 0.7 fs.

We try to further compress the XRL pulse by pumping with the x-ray FEL pulse shown by the black line in Fig. (6.31a). The position of the optical laser is displayed by the red line. This x-ray pump pulse has been acquired by propagating the x-ray FEL pulse through a 25 mm long neon gas cell, where it has been reshaped by absorption. It can be seen that only the front part of the x-ray pump pulse has been absorbed resulting in a reduced rise-time. The gain and intensity in dependence of the interaction length is displayed in Fig. (6.31b),where again the solid lines display the XRL intensity and the dashed lines show the gain as a function of the interaction length in black for the field-free case and in red for the laser-dressed case. Clearly, the shorter rise-times lead to faster saturation of the XRL as well as bigger gains. Before saturation of the laser-dressed XRL at an interaction length of 0.7 mm, the XRL pulse has the temporal profile shown in Fig. (6.32) with black for the field-free case and with red for the laser-dressed case. The FWHM duration of the laser-dressed XRL pulse is 0.2 fs.

6.5. Temporal structuring of x-ray laser pulses

We use an optical laser pulse with two temporally adjacent peaks as shown by the red line in Fig. (6.33a) to imprint a twin-peak structure onto the XRL pulse. We use the x-ray pump pulse shown by the black line in Fig. (6.33a) with the peak intensity of 3.5×10^{17}W/cm^2, the FWHM duration of 75 fs and the spectral FWHM of 0.2 eV.

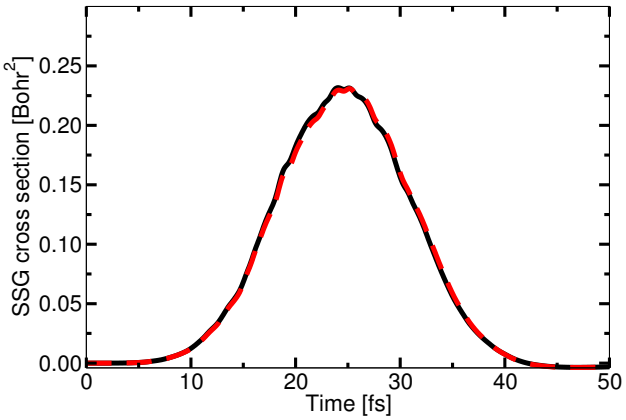

Figure 6.22.: SSG averaged over 300 shots for x-ray FEL pump pulses with a spectral width of 4.3 eV, as shown in Fig. (6.21a), displayed in black for the field-free case and in red for the case with laser-dressing.

Fig. (6.33b) shows the laser-dressed XRL pulse after a propagation distance of 3 mm in the neon gas. It is clear that the twin-peak structure of the optical laser has not been passed on to the XRL pulse.

The black line in Fig. (6.34a) shows the x-ray pump pulse after 3 mm alongside the the optical laser pulse in red. It is apparent from the fact that only the front of the x-ray pump pulse has been changed by absorption that the pumping intensity is so high that the gas is completely excited by the part of the x-ray pump pulse that overlaps only with the first of the two optical laser peaks. This is supported by the temporal profile of the neutral state occupancy of the laser-dressed XRL after 3mm have been propagated in the gas, as is shown in Fig. (6.34b). All atoms are already excited by the time the second optical peak reaches this point.

We lower the x-ray pump pulse's intensity to extend the time interval in which ionization takes place while leaving all other parameters the same. We use the pump pulse and optical pulse displayed in Fig. (6.35). The x-ray pump pulse has a peak intensity of merely 5.6×10^{16} W/cm^2. The XRL pulses acquired this way are shown in Fig. (6.35b) in black after 0.5 mm propagation and in red after 4.4 mm propagation. Initially the XRL pulse (black line) has two clearly distinguishable peaks, however while the second peak is amplified over five order of magnitude, the first peak's intensity hardly increases until the end of the amplifying medium, as can be seen from the red line. The reason for this is the reshaping of the x-ray pump pulse due to absorption. Due to the x-ray pulse's low intensity its front part, which overlaps with the first optical laser peak, is completely absorbed in the medium. Once the overlap is lost the first XRL peak cannot be further amplified. The x-ray pump pulse and the optical laser pulse are shown in Fig. (6.36) after a propagation distance of 2.5 mm. It does not seem possible to produce twin-peak XRL pulses with this scheme.

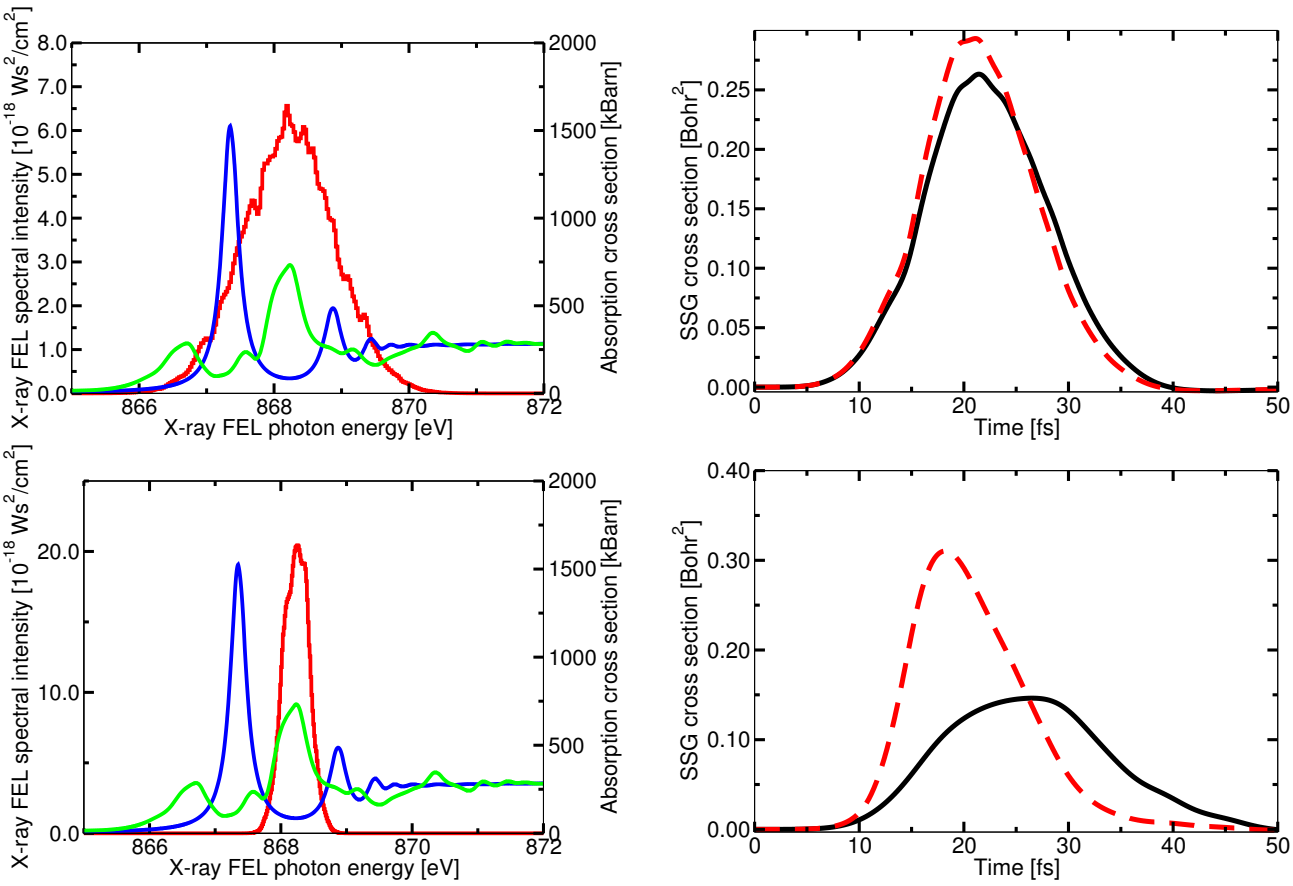

Figure 6.23.: The x-ray FEL bandwidth is 1.5 eV in the top panel and 0.4 eV in the bottom panel. The left-hand side displays the spectral intensity in red, the field-free absorption cross section in blue and the laser-dressed absorption cross section in green. The right-hand side displays the SSG for the field-free case in black and for the laser-dresses case in red.

6.6. Seeding with high-harmonic radiation

We pump the XRL with an x-ray FEL pulse with photons per shot $N_{\mathrm{ph}} = 2.5 \times 10^{12}$, focal radius 1 μm, FWHM duration 10 fs and a peak intensity of 10^{18} W/cm^2. In addition to the optical laser pulse, we use a pulse with photon energy equal to ω_{XRL}, FWHM duration of 13 fs and a peak intensity of 10^{13} W/cm^2, which is produced by high-harmonic generation, to seed the XRL. The seed pulse is shown by the dashed, blue line in Fig. (6.37a) along with the x-ray FEL pump pulse in black and the optical laser pulse in red. Fig. (6.37b) contains the XRL intensity (solid lines) and gain (dashed lines) as a function of the interaction length. The black lines show the field-free case without the seed pulse, the red lines show the laser-dressed case without the seed pulse and the blue lines show the laser-dressed case when the XRL is seeded with high-harmonic radiation. At $z = 0$ the blue line's value is 10^{13} W/cm^2, which is just the intensity of the seed pulse, which is subsequently amplified. It can be seen from Fig. (6.37b) that seeding leads to a much earlier saturation of the XRL, however, the peak XRL intensity is unaffected, as comparison of the red and blue lines reveals. Fig. (6.38) shows the temporal profile of the laser-dressed XRL

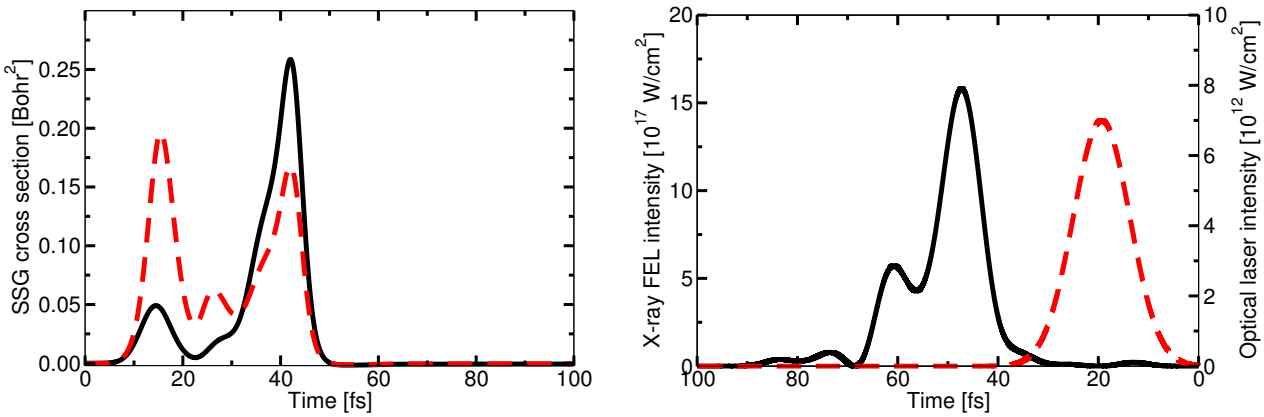

Figure 6.24.: (a) Single-shot calculation of the SSG cross section for the field-free case (black) and the case with laser-dressing (red). (b) X-ray FEL pump pulse with spectral width 0.4 eV (black) and optical laser pulse (red).

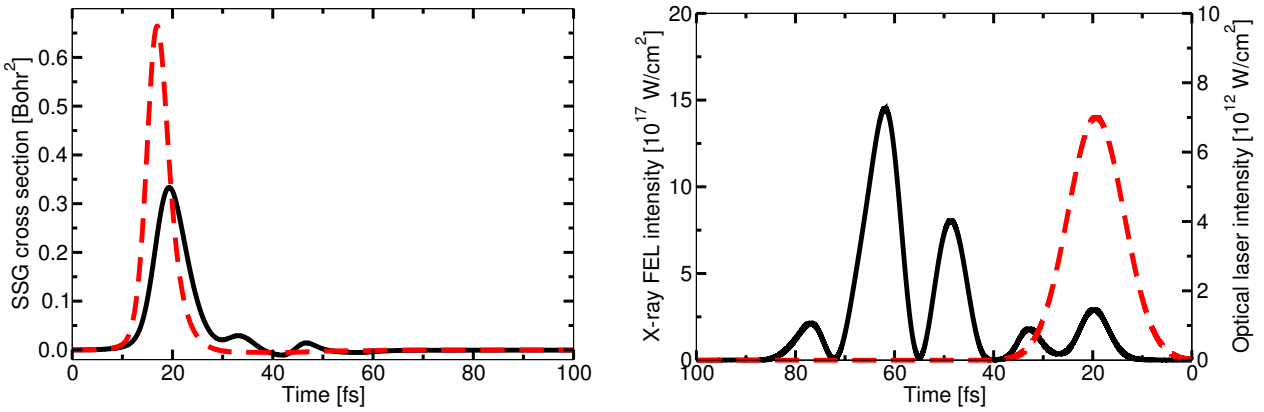

Figure 6.25.: (a) Single shot calculation of the SSG cross section for the field-free case (black) and the case with laser-dressing (red). (b) X-ray FEL pump pulse with spectral width 0.4 eV (black) and optical laser pulse (red).

pulses for the case without seeding (red) after an interaction length of 1.17 mm and for the case with seeding (blue) after an interaction length of 0.5 mm. Both pulses have a peak intensity of approximately 10^{16} W/cm^2.

6.7. Calculational details

We solve the set of coupled partial differential equations consisting of Eqs. (6.7), (6.11), (6.14) and (6.16). First we transform these equations into a set of ordinary differential equations that can be solved using the Runge-Kutta method [100].

We introduce the independent variables $\eta = z$ and $\tau = t - z/c$. With these variables

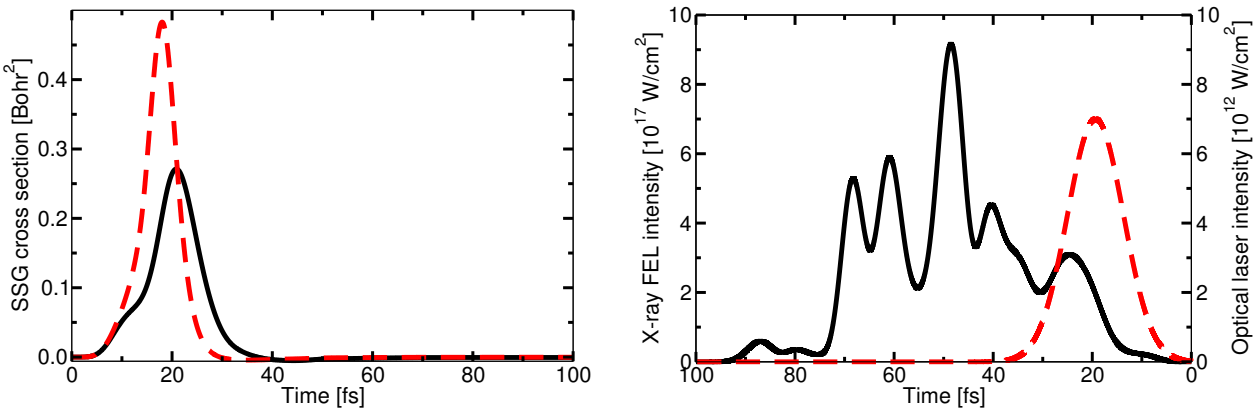

Figure 6.26.: (a) Single shot calculation of the SSG cross section for the field-free case (black) and the case with laser-dressing (red). (b) X-ray FEL pump pulse with spectral width 0.4 eV (black) and optical laser pulse (red).

we obtain the derivatives

$$\frac{\partial}{\partial t} = \frac{\partial}{\partial \tau}\frac{\partial \tau}{\partial t} = \frac{\partial}{\partial \tau}\,, \tag{6.22}$$

$$\frac{\partial}{\partial z} = \frac{\partial}{\partial \eta}\frac{\partial \eta}{\partial z} + \frac{\partial}{\partial \tau}\frac{\partial \tau}{\partial z} = \frac{\partial}{\partial \eta} - \frac{1}{c}\frac{\partial}{\partial \tau}\,, \tag{6.23}$$

$$\frac{\partial}{\partial z} + \frac{1}{c}\frac{\partial}{\partial t} = \frac{\partial}{\partial \eta}\,. \tag{6.24}$$

We express Eqs. (6.7), (6.11), (6.14) and (6.16) in terms of the new variables, which correspond to a reference frame traveling with the speed of light, and transform the differential equation for the XRL pulse in Eqs. (6.16) into a difference equation:

$$\begin{aligned} \Delta I^{+}_{\mathrm{XRL}}(\eta+\Delta\eta,\tau) &= \Delta\eta I^{+}_{\mathrm{XRL}}(\eta,\tau) c n_{\mathrm{A}}\{\sigma_{\mathrm{se}} N_{\mathrm{U}}(\eta,\tau) - \sigma_{\mathrm{abs}} N_{\mathrm{L}}(\eta,\tau)\} \\ &\quad + \Delta\eta \frac{\Omega(\eta)}{4\pi} A_{2\mathrm{p}\to 1\mathrm{s}} N_{\mathrm{U}}(\eta,\tau) c n_{\mathrm{A}} + I^{+}_{\mathrm{XRL}}(\eta,\tau) \end{aligned} \tag{6.25}$$

The propagation of the x-ray FEL pulse is also described by a difference equation. In the propagation calculations we have done in Sec. (6.2) the bandwidth of the pump pulse was always limited to 0.2 eV. It can be seen in Fig. (**??**) that if we assume this, the spectrum is much narrower than the resonance in the laser-dressed absorption cross section at the x-ray FEL central frequency ω_{XFEL}. As an approximation we have assumed that the x-ray FEL pump pulse is monochromatic and its propagation and absorption is given by

$$\begin{aligned} \Delta I_{\mathrm{P}}(\eta+\Delta\eta,\tau) &= \Delta I_{\mathrm{P}}(\eta,\tau) - \Delta\eta \Delta I_{\mathrm{P}}(\eta,\tau) c n_{\mathrm{A}} \\ &\quad \times \{\sigma^{\mathrm{Tot}}_{\mathrm{N}}(I_{\mathrm{L}},\omega_{XFEL}) N_{\mathrm{N}}(\eta,\tau) + \sigma^{\mathrm{Tot}}_{\mathrm{U}} N_{\mathrm{U}}(\eta,\tau) + \sigma^{\mathrm{Tot}}_{\mathrm{L}} N_{\mathrm{L}}(\eta,\tau)\}\,. \end{aligned} \tag{6.26}$$

The three summands appear in the bracket because the x-ray FEL pulse can be absorbed by atoms in the ground state, atoms in the upper state and atoms in the lower state of the

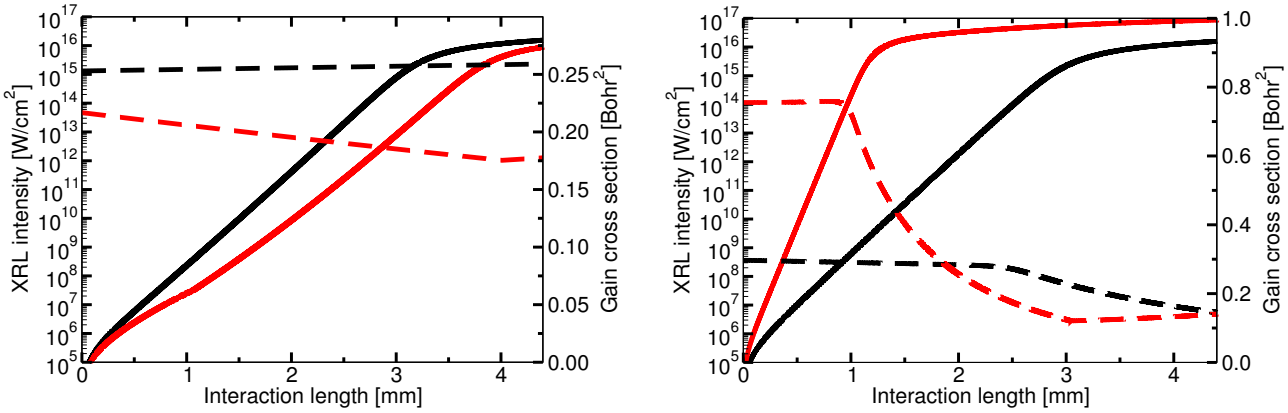

Figure 6.27.: (a) XRL intensity displayed with the solid lines and gain displayed with the dashed lines for the pump pulse from Fig. (6.24b) with black for the field-free case and with red for the case with laser-dressing. (b) XRL intensity displayed with the solid lines and gain displayed with the dashed lines for the pump pulse from Fig. (6.25b) with black for the field-free case and with red for the case with laser-dressing.

lasing transition. The atoms in the different states absorb the pump pulse with varying strength.

We use a fourth-order Runge-Kutta integrator [100] to solve Eqs. (6.7), (6.11), (6.14) over τ to obtain the temporal profile of the neutral state, upper level and lower level occupancy, respectively, at every step in η. $I_{\mathrm{P}}(\eta,\tau)$ and $I^{\pm}_{\mathrm{XRL}}(\eta+\Delta\eta,\tau)$ are then solved through first-order forward stepping in η [1].

The function $\sigma^{\mathrm{Tot}}_{\mathrm{N}}(I_{\mathrm{L}},\omega_{XFEL})$ is acquired by calculating the absorption cross section as a function of the photon energy at nine different laser-dressing intensities with the DREYD code v1.3.0 [89] and doing a two-dimensional interpolation.

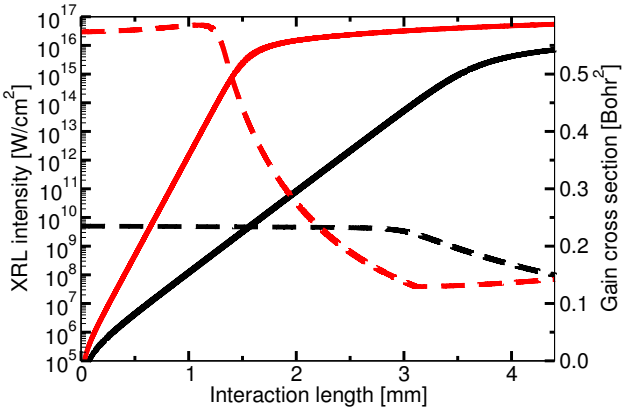

Figure 6.28.: (a) XRL intensity displayed with the solid lines and gain displayed with the dashed lines for the pump pulse from Fig. (6.26b) with black for the field-free case and with red for the case with laser-dressing.

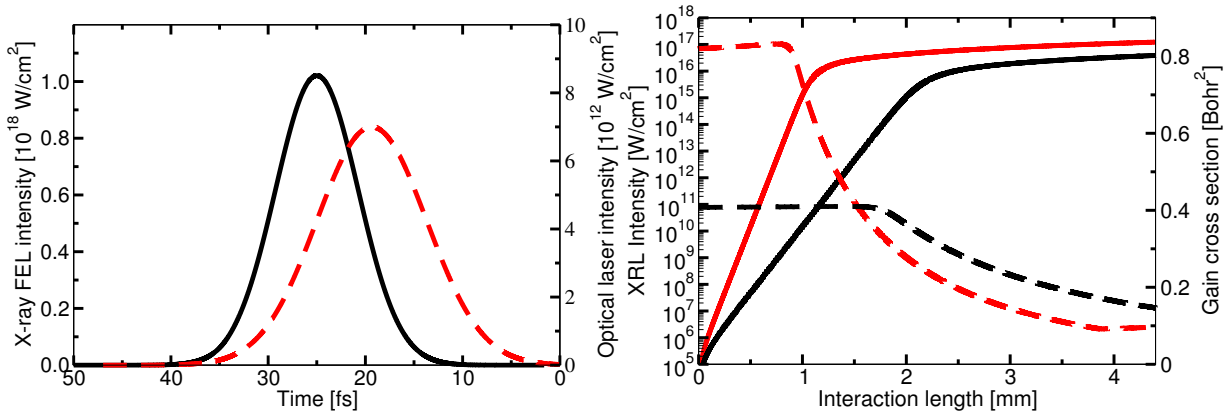

Figure 6.29.: a) Temporal profiles of the x-ray pump pulse (black line) and the optical laser pulse (red line). b) The solid lines show the XRL intensity, while the dashed lines show the gain cross section, both in dependence of the interaction length, for the field-free (black lines) and the laser-dressed case (red lines). The x-ray pump pulse and optical laser pulse from a) are used.

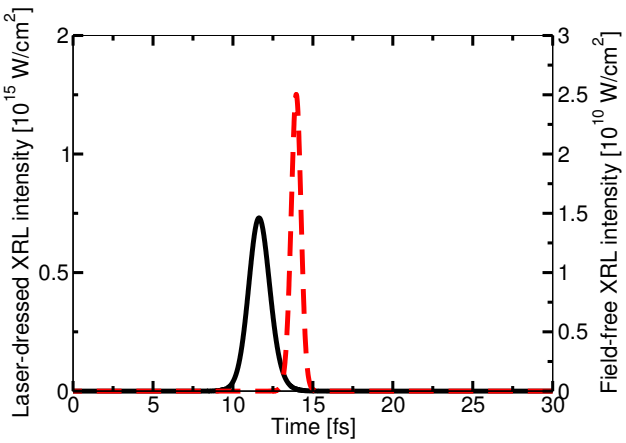

Figure 6.30.: The temporal profile of the XRL pulses for the field-free (black line) and the laser-dressed case are displayed before saturation of the laser-dressed XRL. The x-ray pump pulse and optical laser pulse from Fig. (6.29a) are used.

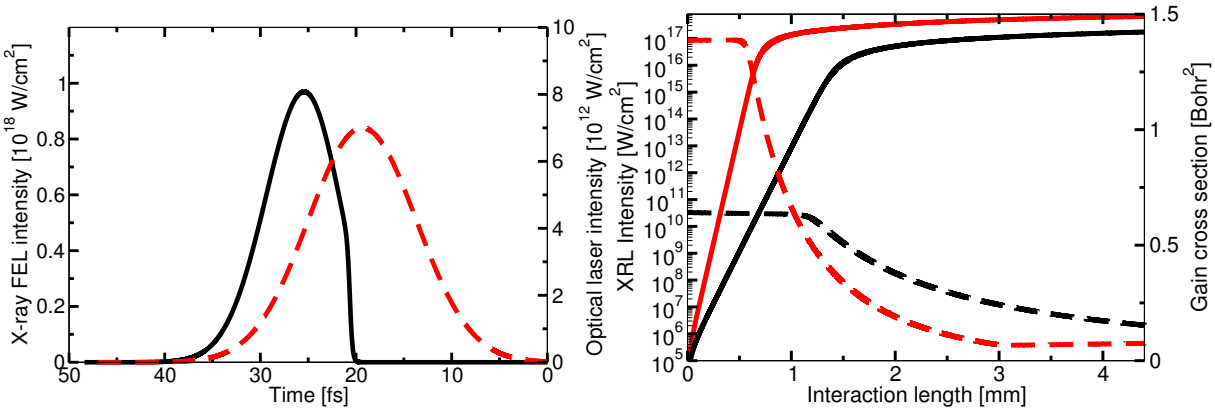

Figure 6.31.: Temporal profiles of the x-ray pump pulse (black line) and the optical laser pulse (red line). The x-ray pump pulse has been propagated through a 25 mm long neon gas cell before interacting with the lasing medium to reduce the pulse's rise time through absorption. b) The solid lines show the XRL intensity, while the dashed lines show the gain cross section, both in dependence of the interaction length, for the field-free (black lines) and the laser-dressed case (red lines). The x-ray pump pulse and optical laser pulse from a) are used. Compared to Fig. (6.29b) the XRL saturates earlier and the gain cross section is increased before saturation.

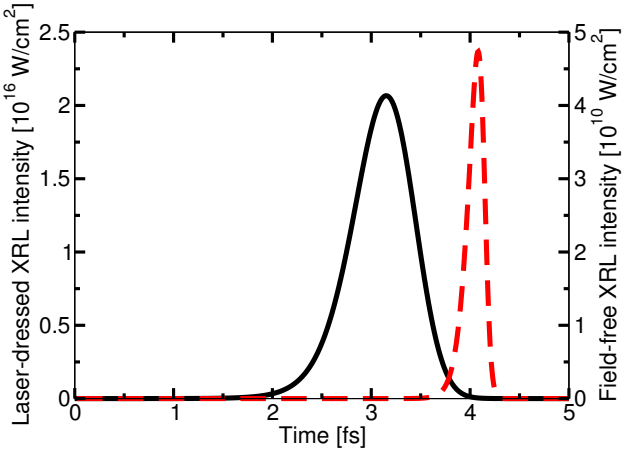

Figure 6.32.: The temporal profiles of the XRL pulses for the field-free (black line) and the laser-dressed case are displayed before saturation of the laser-dressed XRL. The x-ray pump pulse and optical laser pulse from Fig. (6.31a) are used. Compared to Fig. (6.30) the pulses are more intense and shorter.

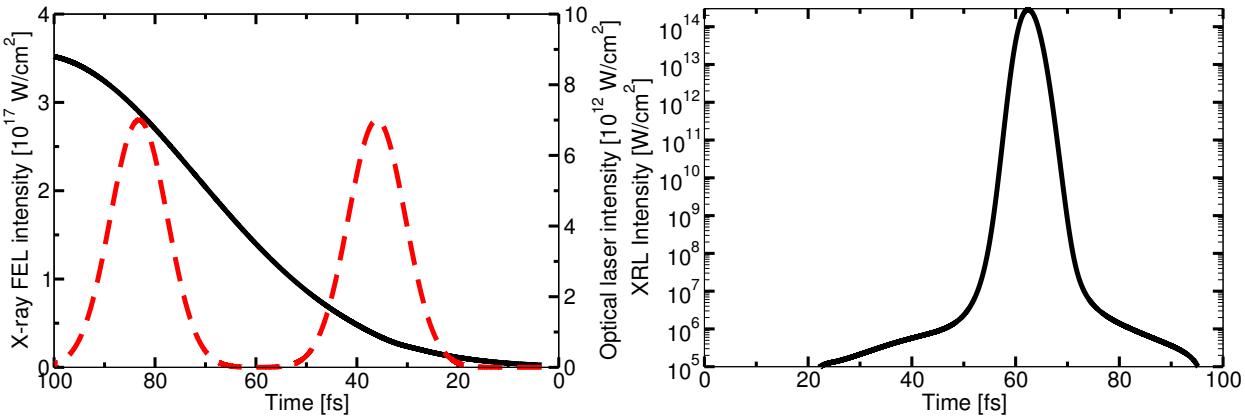

Figure 6.33.: Temporal profiles of the initial x-ray pump pulse with peak intensity of $3.5 \times 10^{17}\mathrm{W/cm^2}$ (black line) and the optical laser pulse with twin-peaks (red line). b) The XRL pulse after a propagation distance of 3 mm is shown for laser-dressing with the twin-peak optical laser pulse.

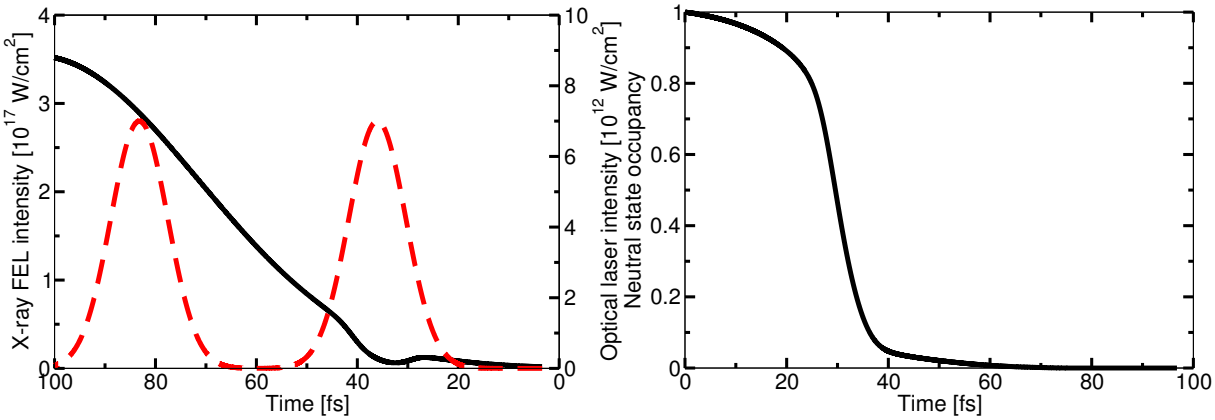

Figure 6.34.: Temporal profiles of the x-ray pump pulse with peak intensity of 3.5×10^{17}W/cm^2 (black line) and the optical laser pulse with twin-peaks (red line) are shown after a propagation distance of 3 mm. Based on the reshaping of the x-ray pump pulse it is evident that only the front portion of the pulse contributes to the excitation of the atoms. b) Temporal profile of the groundstate occupancy after 3 mm is displayed, confirming the conclusion from a) as all atoms are excited after 60 fs before the second optical laser peak arrives.

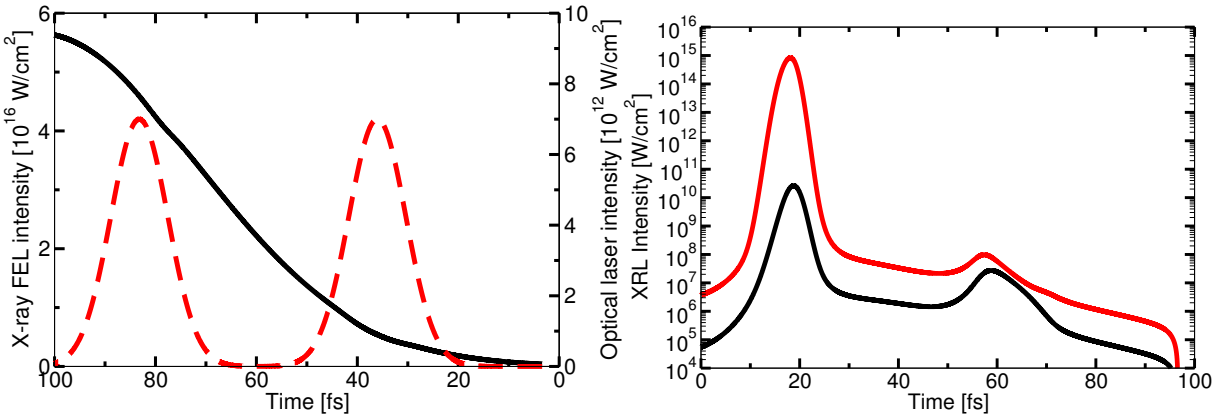

Figure 6.35.: Temporal profiles of the initial x-ray pump pulse with peak intensity of 5.6×10^{16} W/cm^2 (black line) and the optical laser pulse with twin-peaks (red line). b) The XRL pulse for laser-dressing with the twin-peak optical laser pulse from a) is displayed after a propagation distance of 0.5 mm (black line) and after a propagation distance of 4.4 mm (red line).

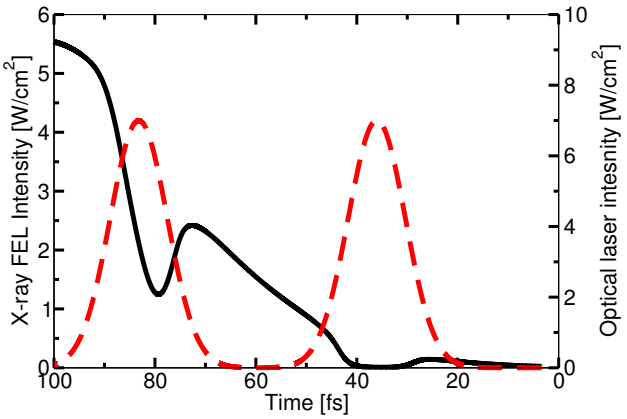

Figure 6.36.: Temporal profiles of the x-ray pump pulse with peak intensity of $5.6 \times 10^{16}\mathrm{W/cm^2}$ (black line) and the optical laser pulse with twin-peaks (red line) are shown after a propagation distance of 2.5 mm. Reshaping of the x-ray pump pulse due to absorption results in the loss of the initially chosen overlap with the optical laser pulse as the first 40 fs of the x-ray pulse are effectively gone.

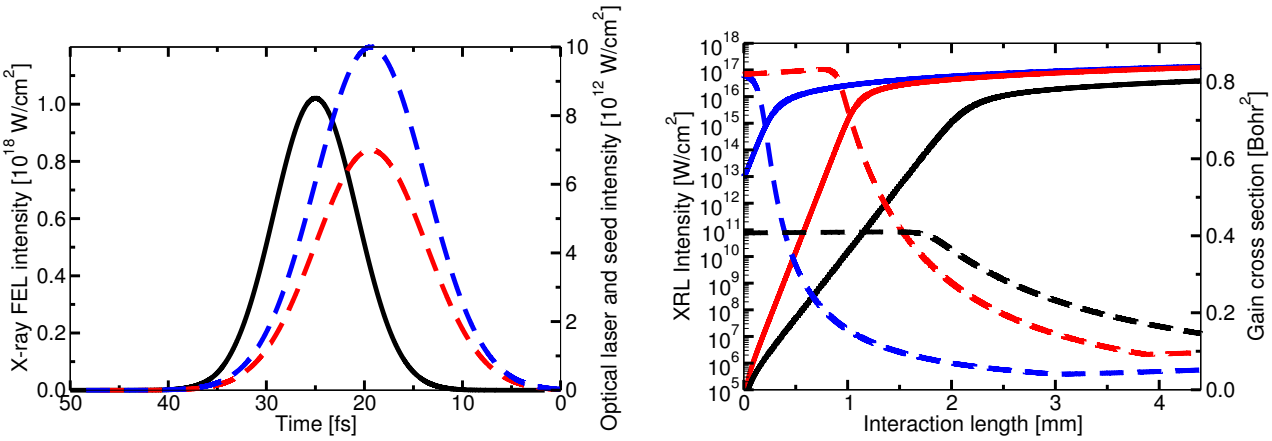

Figure 6.37.: (a) The x-ray pump pulse is shown in black, the optical laser pulse is shown in red and the seed pulse is shown in blue. (b) The solid lines show the peak XRL intensity as a function of the interaction length and the dashed lines show the gain as a function of the interaction length. The black lines show the field-free case without a the seed pulse. The red lines show the laser-dressed case without a seed pulse and the blue lines show the laser-dressed case with seeding.

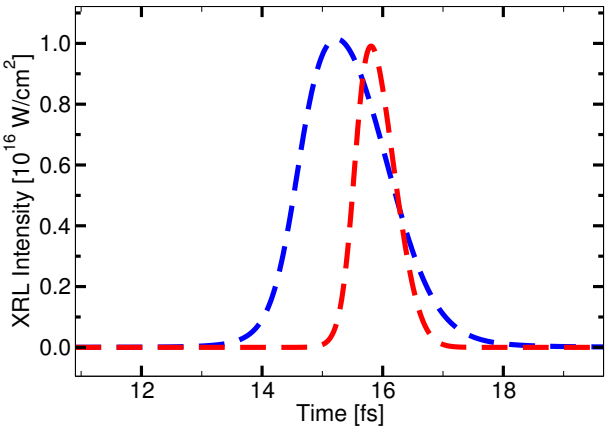

Figure 6.38.: Temporal profiles of the laser-dressed XRL pulse without seeding after an interaction length of 1.17 mm in red and of the laser-dressed XRL pulse with seeding after an interaction length of 0.5 mm in blue.

7. Conclusion

In this thesis we have investigated a method to control the output of an inner-shell neon XRL pumped by an x-ray FEL. In our scheme the x-ray FEL's central frequency is chosen to be below the K edge to avoid multiply core-ionized states that would open up other, competing lasing channels [37–39]. Furthermore, an optical laser collinearly propagating with the x-ray FEL pulse has been added to the setup. The optical laser dresses [42] the neon atoms and modifies the absorption cross section [43, 44], thereby also modulating the upper x-ray lasing state's pumping rate; the atoms are efficiently excited only in the presence of the optical laser, making it possible to control the x-ray lasing process. We have shown that the XRL's output intensity can be increased by as much as seven orders of magnitude through optical laser-dressing. Although the XRL's output still depends on the shape of the x-ray FEL pulse, we can control when the XRL produces a pulse by placing an absorber behind the neon gas cell. The intensity expected from the XRL for the field-free case is absorbed, while the output from the laser-dressed XRL is hardly reduced due to its several orders of magnitude higher intensity.

We have used a system of coupled rate equations [1, 75], incorporating the excitation process via x-ray aborption, spontaneous emission, stimulated emission and Auger decay, to describe the laser. We solved the rate equations with the Runga-Kutta method [100] acquiring the temporal profiles of the neutral state occupancy, the upper level occupancy, the lower level occupancy, the x-ray FEL pulse and the XRL pulse at every point in the medium. Analysis has shown that for optical control of lasing to be efficient, the bandwidth of the pumping radiation needs to be limited to approximately 0.4 eV in order to be able to exploit the strong variations of the absorption cross section in the vicinity of the x-ray FEL's central frequency. If the spectral intensity distribution is much broader than the resonances in the absorption cross section, laser-dressing does not facilitate a more rapid build-up of population inversion. Furthermore, the optical laser pulse's timing needs to be very precise with respect to the x-ray FEL pulse to increase absorption at the right time and to lead to higher gain in the medium.

With this scheme it is possible to produce coherent x-ray pulses at a photon energy of 850 eV (1.43 nm) with spectral width 0.25 eV. The output consists of a single peak of sub-femtosecond duration and intensities up to 10^{17} W/cm^2. It is possible to control the XRL's output with the optical laser pulse. The optical laser's intensity determines the modulation of the medium's gain via the absorption cross section and makes it possible to adjust the XRL's intensity. Additionally, the XRL pulse is synchronized with the optical laser pulse to within approximately 5 fs.

We have shown that it is possible to produce x-ray pulses with FWHM duration of as little as 0.2 fs. For this, it is crucial that the x-ray FEL pulse has a very short rise time and reaches intensities over 10^{18} W/cm^2 within 1–2 fs. Since a one-dimensional model is used to calculate the XRL's output intensity and no correlations between the neon atoms exist

orthogonally to the propagation axis, an optical laser pulse's transverse intensity profile can be imprinted onto the XRL pulse. We have found that it is not possible to produce twin XRL pulses consisting of two temporally consecutive intensity peaks. The reason for this is that low intensity pump pulses that excite the atoms slowly are required to produce temporally long patterns, however, these pump pulses are significantly reshaped whilst propagation; the overlap between the x-ray FEL pulse and the optical laser pulse initially set to produce two temporally adjacent peaks in the gain cross section is lost after a short propagation distance.

This XRL scheme can be used for the study of atomic or molecular dynamics [2]. Such a setup at an x-ray FEL facility would make it possible to do two-color pump-probe experiments [45] with sub-femtosecond x-ray pulses synchronized to an optical laser with femtosecond precision; one pulse excites an atom or molecule while the other pulse probes the sample as a function of the time delay between the pulse [2, 45]. With x-ray pulses of sub-femtosecond duration it is possible to observe the dynamics of ultra-fast-decaying inner-shell resonances [46].

Furthermore, the shortness of the pulses produced by our XRL scheme can be exploited in the single-shot imaging of macromolecules with coherent x-ray scattering [47–50], where radiation damage determines the resolution limit [49]. X-rays preferentially ionize core electrons [19] creating hollow atoms, that is ions where the K shell is not occupied. The atomic form factor of hollow atoms is only minutely modified compared the neutral atoms' [50]. With sub-femtosecond x-ray pulses, which are shorter than the double-core-hole lifetimes, the samples can be probed before relaxation effects occur. If the core holes are retained over the duration of the pulse, the sample becomes transparent for x-ray [101] because of the small x-ray absorption cross section of outer-shell electrons and electronic damage is reduced. Also, coulomb explosion of the sample due to ionization of its atoms can be neglected on a sub-femtosecond time scale [50]. All three of these effects result in more accurate x-ray scattering patters [50].

As a next step, investigating the coherence properties of the pulses produced by this scheme would be of interest. In order to do this, the rate equations for the XRL intensity need to be replaced by rate equations for the electric field envelope and supplemented by a rate equation for the electric field's phase to have complete knowledge of the electric field [75] propagating in the medium. Additionally, it may be of interest to study the feasibility of transferring this scheme to the hard x-ray region. The key for finding other atoms as candidates is how strongly the absorption cross section can be modulated with an optical laser, as that determines how well the XRL's output can be controlled. Most likely choices are the heavier noble gases Ar, Kr, Xe and Rn as these have similar atomic structures as Ne.

8. Acknowledgments

I would like to thank Prof. Dr. Christoph H. Keitel for giving me the opportunity to write my diploma thesis in a supportive and motivating environment at the Max-Planck-Institut für Kernphysik and for making my participation in the DPG-Frühjahrstagung possible. I am also grateful to Prof. Dr. Dirk Dubbers for evaluating my diploma thesis.

I would like to thank Dr. Christian Buth for providing me with an interesting project and guidance throughout this past year. This work would not have been possible without his ideas and support. Our discussions helped me connect the dots and develop a better all-around understanding of the physics underlying my research.

My thanks are also extended to Dr. Markus Kohler and Stefano Cavaletto for their help throughout the year and especially for the invaluable feedback they provided me with on my writing. Their comments helped me a great deal in elucidating my thoughts and in giving a clearer picture of my findings.

I would also like to thank my room mates Héctor Cortés, Anis Dadi and Dr. Hossein Ebadi for the pleasant working atmosphere in the office, as well as Sibel Babacan and Dominik Hertel for being courteous and patient whenever I needed help.

Furthermore, I am grateful to my friends for bearing with me through some stressful times, in particular Fernando Oster, with whom I was fortunate enough to share this experience.

Bibliography

[1] P. W. Milonni and J. H. Eberly, *Laser Physics*, John Wiley and Sons, Hoboken (New Jersey), 2010.

[2] W. Demtröder, *Laser Spectroscopy*, volume 1 and 2, Springer, Berlin, 4th edition, 2008.

[3] L. Essen and J. V. L. Parry, An Atomic Standard of Frequency and Time Interval: A Caesium Resonator, Nature **176**, 280 (August 1955).

[4] S. Chu, J. E. Bjorkholm, A. Ashkin, and A. Cable, Experimental Observation of Optically Trapped Atoms, Phys. Rev. Lett. **57**, 314 (July 1986).

[5] A. Einstein, Zur Quantentheorie der Strahlung, Phys. Z. **18**, 121 (1917).

[6] T. H. Maiman, Stimulated Optical Radiation in Ruby, Nature **187**, 494 (August 1960).

[7] T. H. Maiman, Optical and microwave-optical experiment in ruby, Phys. Rev. Lett. **4**, 564 (June 1960).

[8] J. P. Gordon, H. J. Zeiger, and C. H. Townes, The Maser-New Type of Microwave Amplifier, Frequency Standard, and Spectrometer, Phys. Rev. **99**, 1264 (August 1955).

[9] J. P. Gordon, H. J. Zeiger, and C. H. Townes, Molecular Microwave Oscillator and New Hyperfine Structure in the Microwave Spectrum of NH_3, Phys. Rev. **95**, 282 (July 1954).

[10] A. L. Schawlow and C. H. Townes, Infrared and Optical Masers, Phys. Rev. **112**, 1940 (December 1958).

[11] A. M. Prokhorov, Molecular amplifier and generator for submillimeter waves, Sov. Phys. JETP **34**, 1658 (June 1958).

[12] C. H. Townes, Production of coherent radiation by atoms and molecules, Nobel Lecture, December 11, 1964.

[13] A. M. Prokhorov, Quantum electronics, Nobel Lecture, December 11, 1964.

[14] A. L. Schawlow, Spectrsocopy in a new light, Nobel Lecture, December 8, 1981.

[15] R. C. Elton, *X-Ray Lasers*, Academic Press, 1st edition, 1990.

[16] S. Suckewer and P. Jaegle, X-Ray laser: past, present, and future, Laser Physics Letters **6**, 411 (March 2009).

[17] P. W. Milonni and J. H. Eberly, *Lasers*, Wiley, New York, 1988.

[18] H. C. Kapteyn, *Photoionization-Pumped Short-Wavelength Lasers*, PhD thesis, University of California, Berkley, 1989.

[19] J. Als-Nielsen and D. McMorrow, *Elements of Modern X-Ray Physics*, John Wiley and Sons, New York, 2000.

[20] D. L. Matthews *et al.*, Demonstration of a Soft X-Ray Amplifier, Phys. Rev. Lett. **54**, 110 (January 1985).

[21] J. M. J. Madey, Stimulated Emission of Bremsstrahlung in a Periodic Magnetic Field, J. Appl. Phys. **42**, 1906 (April 1971).

[22] E. Saldin, E. Schneidmiller, and M. V. Yurkov, *The Physics of Free Electron Lasers*, Advanced Texts in Physics, Springer, Berlin, 1st edition, 2000.

[23] J. Feldhaus, J. Arthur, and J. B. Hastings, X-ray free-electron lasers, Journal of Physics B: Atomic, Molecular and Optical Physics **38**, 799 (2005).

[24] http://hasylab.desy.de/facilities/flash.

[25] P. Emma *et al.*, First lasing and operation of an ångstrom-wavelength free-electron laser, Nature Photonics **4**, 641 (August 2010).

[26] http://lcls.slac.stanford.edu.

[27] D. Pile, X-rays: First light from SACLA, Nature Photonics **5**, 456 (July 2011).

[28] http://xfel.riken.jp/eng/.

[29] E. Saldin, E. Schneidmiller, and M. Yurkov, Statistical properties of radition from VUV and X-ray free electron laser, Optics Communications **148**, 383 (March 1998).

[30] E. Saldin, E. Schneidmiller, and M. Yurkov, Statistical and coherence properties of radiation from x-ray free-electron lasers, New J. Phys. **12** (March 2010).

[31] R. Bonifacio, C. Pellegrini, and L. M. Narducci, Collective instabilities and high-gain regime in a free electron laser, Optics Communications **50**, 373 (July 1984).

[32] M. A. Duguay and P. M. Rentzepis, Some approaches to vacuum UV and x-ray lasers, Applied Physics Letters **10**, 350 (June 1967).

[33] H. C. Kapteyn, Photoionization-pumped x-ray lasers using ultrashort-pulse excitation, Applied Optics **31**, 4931 (August 1992).

[34] T. S. Axelrod, Inner-shell photoionization-pumped x-ray lasers. Sulfur*, Phys. Rev. A **13**, 376 (October 1976).

[35] K. Lan, E. Fill, and J. Meyer-Ter-Vehn, Photopumping of XUV lasers by XFEL radiation, Laser and Particle Beams **22**, 261 (2004).

[36] J. Nilsen and H. A. Scott, Using the X-ray free-electron laser to drive a photo-pumped helium-like neon X-ray laser at 23nm, High Energy Density Physics **7**, 6 (2011).

[37] N. Rohringer and R. London, Atomic inner-shell x-ray laser pumped by an x-ray free-electron laser, Phys. Rev. A **80**, 013809 (July 2009).

[38] N. Rohringer and R. London, Erratum: Atomic inner-shell x-ray laser pumped by an x-ray free-electron laser, Phys. Rev. A **82**, 049902 (Octorber 2010).

[39] N. Rohringer, An atomic inner-shell laser pumped with an x-ray free-electron laser, J.Phys: Conference Series **194**, 012012 (2009).

[40] J. Zhao, Q. L. Dong, S. J. Wang, L. Zhang, and J. Zhang, X-ray lasers from Inner-shell transitions pumped by the Free-electron laser, Optics Express **16**, 3546 (March 2008).

[41] N. Rohringer *et al.*, in preparation.

[42] P. Meystre and M. Sargent, *Elements of Quantum Optics*, Springer, Berlin, 3rd edition, 1999.

[43] C. Buth, R. Santra, and L. Young, Electromagnetically Induced Transparancy for X Rays, Phys. Rev. Lett. **98**, 253001 (June 2007).

[44] C. Buth and R. Santra, Theory of x-ray absorption by laser-dressed atoms, Phys. Rev. A **75**, 033412 (March 2007).

[45] F. J. Wuilleumier and M. Meyer, Pump-probe experiments in atoms involving laser and synchrotron radiation: an overview, J. Phys. B: At. Mol. Opt. Phys. **39**, 425 (November 2006).

[46] M. Drescher *et al.*, Time-resolved atomic inner-shell spectroscopy, Nature **419**, 803 (October 2002).

[47] R. Neutze, R. Wouts, D. van der Spoel, E. Weckert, and J. Hajdu, Potential for biomolecular imaging with femtosecond X-ray pulses, Nature **406**, 752 (August 2000).

[48] H. N. Chapman *et al.*, Femtosecond diffractive imaging with a soft-X-ray free-electron laser, Nature Physics **2**, 839 (November 2006).

[49] M. R. Howells *et al.*, An assessment of the resolution limitation due to radiation-damage in X-ray diffraction microscopy, Journal of Electron Spectroscopy and Related Phenomena **170**, 4 (2009).

[50] S.-K. Son, L. Young, and R. Santra, Impact of hollow-atom formation on coherent x-ray scattering at high intensity, Phys. Rev. A **83**, 033402 (March 2011).

[51] W. C. Röntgen, Über eine neue Art von Strahlung, Aus den Sitzungsberichten der Würzburger Physik.-medic. Gesellschaft Würzburg , 137 (1985).

[52] W. Demtröder, *Experimentalphysik 3: Atome, Moleküle und Festkörper*, Springer, Berlin, 2009.

[53] N. B. Delone and V. P. Krainov, *Multiphoton processes in atoms*, Springer series on atoms and plasmas, Springer, Berlin, 2nd edition, 1994.

[54] J. D. Jackson, *Classical Electrodynamics*, John Wiley and Sons, Hoboken (New Jersey), 3rd edition, 1999.

[55] M. A. Kornberg *et al.*, Interaction of atomic systems with X-ray free-electron lasers, J. Synchrotron Rad. **9**, 298 (September 2002).

[56] L. R. Elias, W. M. Fairbank, J. J. Madey, H. A. Schwettman, and T. I. Smith, Observation of Stimulated Emission of Radiation by Relativistic Electrons in a Spatially Periodic Magnetic Field, Phys. Rev. Lett. **36**, 717 (March 1976).

[57] A. Thompson, D. Attwood, E. Gullikson, M. Howells, K.-J. Kim, J. Kirz, J. Kortright, I. Lindau, Y. Liu, P. Pianetta, A. Robinson, J. Scofield, J. Underwood, and G. Williams, X-ray Data Booklet, Lawrence Berkley National Laboratory, University of California, Berkley, CA 94720, October 2009.

[58] http://www.xfel.eu.

[59] http://www.psi.ch.

[60] E. Saldin, E. Schneidmiller, Y. V. Shvyd'ko, and M. V. Yurkov, X-ray FEL with a meV bandwidth, Nucl. Instrum. Methods Phys. Res., Sect. A **475**(1-3), 357 (December 2001).

[61] J. Feldhaus, E. Saldin, J. R. Schneider, E. Schneidmiller, and M. V. Yurkov, Possible application of X-ray optical elements for reducing the spectral bandwidth of an X-ray SASE FEL, Optics Communications **140**, 341 (March 1997).

[62] G. Doumy *et al.*, Nonlinear Atomic Response to Intense Ultrashort X Rays, Phys. Rev. Lett. **106**, 083002 (February 2011).

[63] N. Rohringer and R. Santra, Resonant Auger effect at high x-ray intensity, Phys. Rev. A **77**, 053404 (May 2008).

[64] N. Rohringer and R. Santra, X-ray nonlinear optical processes using self-amplified spontaneous emission free-electron laser, Phys. Rev. A **76**, 033416 (September 2007).

[65] L. Young *et al.*, Femtosecond electronic response of atoms to ultra-intense X-rays, Nature **466**, 56 (July 2010).

[66] L. Fang *et al.*, Double Core-Hole Production in $N2$: Beating the Auger Clock, Phys. Rev. Lett. **105**, 083005 (August 2010).

[67] H. N. Chapman *et al.*, Femtosecond X-ray protein nonocrystallography, Nature **470**, 73 (February 2011).

[68] M. M. Seibert, T. Ekeberg, F. R. N. C. Maia, M. Svenda, J. Andreasson, and O. Jönsson, Single mimivirus particles intercepted and imaged with an X-ray laser, Nature **470**, 78 (February 2011).

[69] J. J. Turner *et al.*, X-Ray Diffraction Microscopy of Magnetic Structures, Phys. Rev. Lett. **107**, 033904 (July 2011).

[70] T. Pfeifer, Y. Jiang, S. Düsterer, R. Moshammer, and J. Ullrich, Partial-coherence method to model experimental free-electron laser pulse statistics, Optics Letters **35**, 3441 (October 2010).

[71] Y. H. Jiang *et al.*, Temporal coherence effects in multiple ionization of N_2 via XUV pump-propb autocorrelation, Phys. Rev. A **82**, 041403(R) (October 2010).

[72] G. Vannucci and M. C. Teich, Computer simulation of superposed coherent and chaotic radiation, Appl. Opt. **19**, 548 (February 1980).

[73] J. C. Diels and W. Rudolph, *Ultrashort Laser Pulse Phenomena*, Academic Press, San Diego, 1st edition, 1996.

[74] F. Schwabl, *Quantenmechanik*, volume 1, Springer, Berlin, 7th edition, 2007.

[75] M. O. Scully and M. S. Zubairy, *Quantum Optics*, Cambridge University Press, Cambridge (UK), 2002.

[76] W. E. Lamb, Theory of an Optical Maser, Physical Review **134**, 1429 (June 1964).

[77] H. Haken and H. Sauermann, Nonlinear Interaction of Laser Modes, Zeitschrift fuer Physik **173**, 261 (1963).

[78] P. N. Butcher and D. Cotter, *The Elements of Nonlinear Optics*, Cambridge Studies in Modern Optics, Cambridge University Press, reprint edition, 1991.

[79] A. E. Siegman, *Lasers*, University Science Books, 1st edition, 1986.

[80] M. Fleischhauer, A. Imamoglu, and J. P. Marangos, Electromagnetically induced transparancy: Optics in coherent media, Reviews of Modern Physics **77**, 633 (April 2005).

[81] A. Imamoglu and S. E. Harris, Lasers without inversion: interference of dressed lifetime-broadened states, Optics Letters **14**, 1344 (December 1989).

[82] S. H. Autler and C. H. Townes, Stark Effect in Rapidly Varying Fields, Phys. Rev. **100**, 703 (October 1955).

[83] S. E. Harris, J. E. Field, and A. Imamoglu, Nonlinear Opical Processes Using Electromagnetically Induced Transparancy, Phys. Rev. Lett. **64**, 1107 (March 1990).

[84] K.-J. Boller, A. Imamoglu, and S. E. Harris, Observation of Electromagnetically Induced Transparancy, Phys. Rev. Lett. **66**, 2593 (May 1991).

[85] A. Imamoglu, Interference of radiatively broadened resonances, Phys. Rev. A **40**, 2835 (September 1989).

[86] S. E. Harris, Lasers without Inversion: Interference of Lifetime-Broadened Resonances, Phys. Rev. Lett. **62**, 1033 (February 1989).

[87] U. Fano, Effects of Configuration Interaction on Intensities and Phase Shifts, Phys. Rev. **124**, 1866 (December 1961).

[88] R. Madden and K. Codling, Two-Electron Excitation States in Helium, Astrophys. J. **141**, 364 (February 1965).

[89] C. Buth and R. Santra, FELLA-The Free Electron Laser Atomic Physics Program Package, Argonne National Laboratory.

[90] C. P. Bhalla, N. O. Folland, and M. A. Hein, Theoretical K-Shell Auger Rates, Transition Energies, and Flourescence Yields for Multiply Ionized Neon, Phys. Rev. A **8**, 649 (August 1973).

[91] T. E. Glover *et al.*, Controlling X-rays with light, Nature Physics **6**, 69 (January 2009).

[92] A. Kivimäki *et al.*, Auger decay at the $1s^{-1}np$ ($n = 3-5$) resonances of Ne, Journal of Electron Spectroscopy and Related Phenomena **114-116**, 49 (March 2001).

[93] Y. Shimizu *et al.*, Auger spectra of $1s^{-1}3p$ decay: High resolution angle-resolved measurements of Auger emission from the photo-excited $1s^{-1}3p$ state of Ne, Journal of Physics B: Atomic, Molecular and Optical Physics **33**, 685 (September 2000).

[94] Los alamos national laboratory atomic physics codes, http://aphysics2.lanl.gov/cgi-bin/ION/runlanl08d.pl.

[95] R. A. London, Development of coherent x-ray lasers, Phys. Fluids B **5**, 2707 (March 1993).

[96] M. Kato *et al.*, Absolute Photoionization Cross Section with an Ultra-high Energy Resolution for Ne in the Region of 1s Rydberg States, in *Synchroton Radiation Instrumentation: Ninth International Conference on Synchrotron Radiation Instrumentation*, edited by Jae-Young and S. Rah, volume 879 of *AIP Conf. Proc.*, page 1121, American Institute of Physics, 2007.

[97] R. A. McCorkle and J. M. Joyce, Threshold conditions for amplified spontaneous emission of x radiation, Phys. Rev. A **10**, 903 (September 1974).

[98] C. Matsubara, N. C. Dutta, T. Ishihara, and T. P. Das, Brueckner-Goldstone Many-Body Theory for Dynamic Polarizabilities: Application to Ne, Phys. Rev. A **1**, 561 (March 1970).

[99] C. Buth and R. Santra, X-ray refractive index of laser-dressed atoms, Phys. Rev. A **78**, 043409 (October 2008).

[100] H.-R. Schwarz and N. Köckler, *Numerische Mathematik*, Teubner, Wiesbaden, 5th edition, 2004.

[101] M. Hoener *et al.*, Ultraintense X-Ray Induced Ionization, Dissociation, and Frustrated Absorption in Molecular Nitrogen, Phys. Rev. Lett. **104**, 253002 (June 2010).